university of groningen / faculty of science and engineering / kapteyn astronomical institute

An Evolutionary Model for the Milky Way's Corona

Abstract

The study of the circumgalactic medium (CGM) around late-type galaxies is crucial due to its ties to several open problems in the field, like the missing baryon problem, and the question of how cool gas is accreted onto the galaxy to sustain the star formation over a long period of time. The CGM spans a large volume, and is therefore able to contain a large amount of gas that can, overtime, efficiently feed the galaxy. In this work, we focus in particular on the hot phase of CGM, also known as the corona, around the Milky Way and Milky Way-mass galaxies. We study the evolution of such a corona using a semi-analytical model assuming that it is in hydrostatic equilibrium, but evolves via radiative cooling and different forms of heating. We implement evolution by cooling using a classical cooling function and by a more modern code which also includes heating from the extragalactic ultraviolet background. Moreover, we implement mechanical heating from a central source, resembling the source that inflated the Fermi and eROSITA bubbles, by continuously injecting energy in inner few kpc of the system.

Our results show that in isolation, the centre of the corona cools rapidly within $\sim 10\,\mathrm{Myr}$, while the outer regions remain relatively unchanged, but flows inwards at constant mass accretion rates between 0.2 and $1\,\mathrm{M_\odot/yr}$, depending on the mass of our corona. By comparing the evolution of the density and temperature of the corona with a steady-state cooling flow model from the literature, we show a remarkable similarity between the two models. When we add heating from a central source, we estimate an upper and lower bound on the range of powers for which the corona is not cooling nor heating being around $10^{41} - 10^{42}\,\mathrm{erg\,s^{-1}}$, depending on the corona's mass and the chosen distribution over which energy is injected. Finally, we compare this range of powers with literature estimates of the Fermi and eROSITA power source, by averaging them over an entire duty cycle. We find values similar to the power thresholds from our evolutionary model. This could imply that the source that inflated the bubbles is able to stop the cooling of the inner corona, and start a self-regulating cycle that keeps the corona in equilibrium for a long time.

Astronomy Master's Thesis

Author: Sten Sipma

Primary supervisor: Prof. dr. Filippo Fraternali

October 2024

Contents

1 Introduction

The circumgalactic medium (CGM) is a large gaseous component in a galaxy's halo, which is closely tied to many processes pertaining to the evolution of galaxies. Studying the CGM is therefore crucial in understanding the role of supernova and black hole feedback, the regulation of the star formation rate and the distribution of matter in galaxies (Tumlinson et al., 2017). The CGM has been observed to consist of multiple phases ranging from the *cool/cold* CGM phase at $T < 10^5\,\mathrm{K}$, the *warm* phase of the CGM of $10^5 \leq T < 10^6\,\mathrm{K}$ and finally the *hot* CGM phase (or *corona* for late-type galaxies) above $T \gtrsim 10^6\,\mathrm{K}$. Out of these phases, the hot CGM is likely the most massive component in Milky Way-like galaxies, where the total mass seems to be at least of the same order as the stellar component of the galaxy (?Bregman et al., 2022; Locatelli et al., 2024; Zhang et al., 2024). The corona is primarily observed in X-ray emission and absorption, but since Milky Way-like coronae typically have a low surface brightness, observing it has been challenging, and therefore its properties are still not well known.

1.1 Two classical problems related to the CGM

The study of the CGM is primarily motivated by open problems in the field of formation and evolution of galaxies. Among others, these are the missing baryon problem (McGaugh et al., 2009; Dai et al., 2010) and the problem of sustaining the galaxy's star formation rate (SFR) over cosmic time (Fraternali & Tomassetti, 2012).

1.1.1 The missing baryon problem

The missing baryon problem comes from a discrepancy between the cosmological prediction for the number of baryons, and the total observed baryonic matter in galaxies. Standard ΛCDM cosmology predicts a baryonic fraction (ratio of baryonic to dark matter mass) of $f_\mathrm{b} \equiv M_\mathrm{b}/M_\mathrm{dm} \approx 18.7\,\%$ across the universe (Planck Collaboration et al., 2020). Assuming the baryonic fraction in the Milky Way is similar to the universal value, this would give around $f_b M_\mathrm{vir} = 2.3 \times 10^{11}\,\mathrm{M}_\odot$ of expected baryonic matter for Milky Way-mass (assuming the dark matter mass is approximately equal to the virial mass, $M_\mathrm{vir} = 1.3 \times 10^{12}\,\mathrm{M}_\odot$ Bland-Hawthorn & Gerhard, 2016) galaxies. However, when we tally up all the observed baryonic matter from stars and interstellar gas, we get a total mass of around $6 \times 10^{10}\,\mathrm{M}_\odot$ (Sparke & Gallagher III, 2007; Bland-Hawthorn & Gerhard, 2016), which is only $25\,\%$ of the total baryon budget. We are therefore missing more than half of the baryonic matter in Milky Way-mass galaxies, and the discrepancy is even higher for lower mass galaxies (McGaugh et al., 2009). In the estimate of the missing mass above we have not included the baryonic mass in the CGM, so including this could help to alleviate the problem.

Even though the CGM around Milky Way-mass galaxies is expected to extend to the virial radius (roughly $250\,\mathrm{kpc}$), most studies have reported detections up to only $r \sim 70\,\mathrm{kpc}$ (Dai et al., 2012; Bogdán et al., 2013; Anderson et al., 2016; Das et al., 2020). Recently, a signal up to r_vir from stacked coronae in eROSITA (Zhang et al., 2024) has been observed, but such a signal still has to be confirmed for the CGM around an individual galaxy. Assuming the CGM does extend up to the virial radius, this would span a volume up to $0.1\,\mathrm{Mpc}^3$ for the Milky Way (Bland-Hawthorn & Gerhard, 2016), so even a low density gas can still contribute a large amount of mass to the total baryon budget. Estimates of the contribution of the Milky Way hot CGM to the baryonic mass budget range from $10\,\%$ (?Faerman et al., 2020; Locatelli et al., 2024) to higher values around $30-50\,\%$ (Faerman et al., 2017; Bregman et al., 2022; Zhang et al., 2024), where the variance in the mass estimates primarily comes from the assumed metallicity, temperature and entropy profile of the CGM. This already helps to alleviate the missing baryon problem significantly, and some estimates even claim there is enough mass in the CGM to fully solve the issue (Nicastro et al., 2023; Grønnow et al., 2024).

1.1.2 Sustaining star formation in galaxies

In order to form stars, a gas cloud needs to cool to low enough temperatures such that it is dense enough for gravitational instabilities to grow and start the collapse of the cloud. At this point the gas is removed from the interstellar medium (ISM) and stays 'trapped' in the star, only being returned at the end of the star's lifetime for relatively massive stars. The amount of gas that is returned to the ISM depends on the initial mass function (IMF), since high mass stars ($M_\star > 8\,\mathrm{M}_\odot$) have lifetimes around $\sim 10\,\mathrm{Myr}$ they quickly return their gas via core collapse supernovae, but low mass stars ($M_\star < 1\,\mathrm{M}_\odot$) have lifetimes longer than the Hubble time, so the gas will stay trapped forever. For a typical IMF (Salpeter, 1955; Scalo, 1986; Kroupa, 2002; Chabrier, 2003), the mass in low mass stars dominates the total mass of stars that are formed, which implies only fractions around $30 - 40\,\%$ of the gas is returned to the ISM to contribute to the formation of new stars (Cimatti et al., 2019).

When a star forming galaxy does not accrete new gas from outside the ISM, eventually the reservoire of gas will run out and no more stars can be formed. The observed SFR in the Milky Way has been put around $1 - 3\,\mathrm{M}_\odot/\mathrm{yr}$ (Bland-Hawthorn & Gerhard, 2016), and has been shown to be relatively constant for a long ($\tau \geq 10\,\mathrm{Gyr}$) time (Twarog, 1980; Binney et al., 2000). It is possible to estimate the depletion time τ_dep, time it takes for the galaxy to run out of its current gas reservoire, by dividing the observed gas mass by the SFR, thus $\tau_\mathrm{dep} \sim M_\mathrm{g}/\dot{M}_\mathrm{SFR}$. For Milky Way-mass galaxies, this typically gives $\tau_\mathrm{dep} = 2 - 4\,\mathrm{Gyr}$ (Whitaker et al., 2012; Peeples et al., 2014; Tumlinson et al., 2017) which is significantly lower than the time over which the Milky Way has been forming stars. Chemical evolution models of the Milky Way additionally show that accretion of low metallicity gas is needed at low redshift, in order to reproduce the chemical distribution of stars in the disc (Schönrich & Binney, 2009; Kubryk et al., 2013; Schönrich & McMillan, 2017).

For galaxies to keep forming stars, accretion of new gas is therefore required. In the early universe, constant mergers and accretion from nearby satellites are predicted to be able to supply this fresh gas (Kereš & Hernquist, 2009), but the merger history of many star-forming galaxies, including the Milky Way, has been quiescent for a long time (Helmi, 2008; Cooper et al., 2010; Di Teodoro & Fraternali, 2014; Fragkoudi et al., 2020). Neighbouring galaxies therefore cannot be the only source of gas, which leaves us with the accretion from the intergalactic medium (IGM) or CGM (Fraternali & Tomassetti, 2012), and since both of these scenario's involve gas flowing through the CGM before accreting onto the galaxy, it is a crucial component in order to understand gas accretion.

1.2 Observing the hot CGM / corona

The hot CGM, which we will refer to as the corona, is predicted by theory and by cosmological simulations to be a large, diffuse body of shock-ionised gas at temperatures close to the virial temperature, extending out to the virial radius of the halo (White & Frenk, 1991; Fukugita & Peebles, 2006; Fielding et al., 2017). On large scales, the corona is believed to be in hydrostatic equilibrium (Faerman et al., 2017, 2020), but on a small scale, nonequilibrium local conditions are also considered to be important (Binney et al., 2009; Lochhaas et al., 2023). Due to its temperature (around 10^6 K for the Milky Way), the corona is mainly observed in X-rays.

1.2.1 Milky Way observations

The corona of the Milky Way has been observed using [OVII] and [OVIII] absorption in active galactic nuclei (AGN) sightlines (Gupta et al., 2012; Miller & Bregman, 2013) and from X-ray emission (?Li & Bregman, 2017; Ponti et al., 2023; Locatelli et al., 2024). Given an absorbing medium of density n and size L, the column density of absorption lines scales with nL, whereas the column density of emission scales with n^2L. Absorption can therefore probe larger distances, since it fades more slowly than emission. On the other hand, emission maps are typically able to capture a larger area, since they are not constrained by the presence of slightlines. To fully study the corona, it is therefore important to consider both emission and absorption (Gupta et al., 2012; Kaaret et al., 2020). Regardless, observation of the Milky Way are still biased to distances close to the galaxy ($\sim 10\,\mathrm{kpc}$) since these regions tend to dominate the total emission (Locatelli et al.,

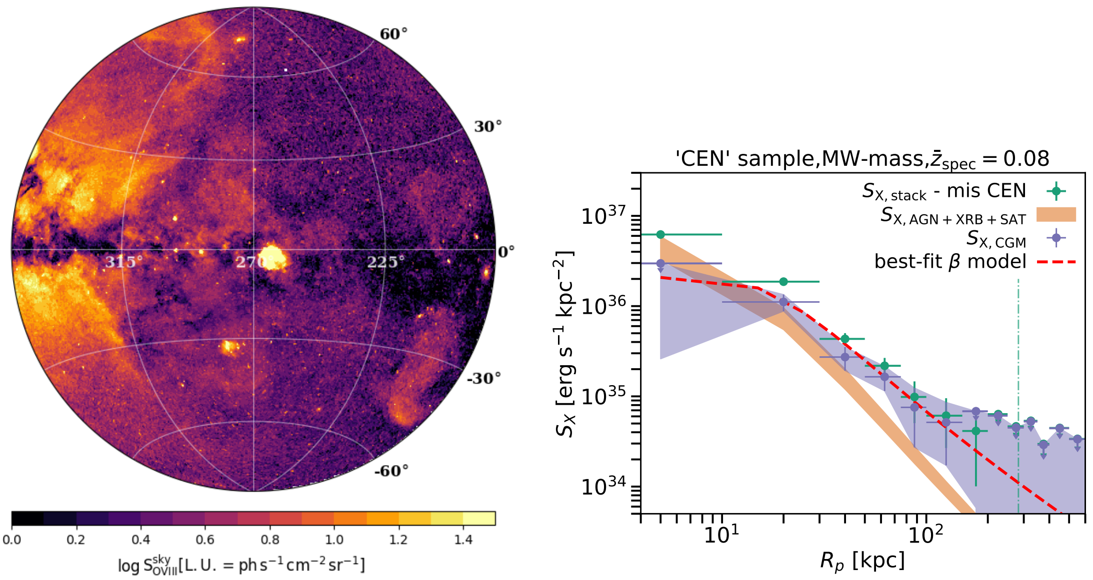

Figure 1: *Left:* Observed sky X-ray surface brightness of the eRASS1 [OVIII] emission from Locatelli et al. (2024). The image is a Zenith Equal Area projection in galactic coordinates centered at $l = 270$ and $b = 0\,\mathrm{deg}$. The data in the image are background subtracted, but foreground contamination from various sources is still clearly visible. Image taken from Locatelli et al. (2024). *Right:* X-ray surface brightness profiles of stacked Milky Way-mass galaxies in eRASS:4 from Zhang et al. (2024) showing a signal of the CGM out to the virial radius. The figure shows the stacked surface brightness after masking and correction of misclassifications ($S_{\rm X,stack}$, green points), a model for the unresolved AGN and X-ray binaries ($S_{\rm X,AGN+XRB+SAT}$, orange band), and the stacked CGM X-ray brightness ($S_{\rm X,stack}$ with AGN + XRB subtracted, purple band). The red-dashed line shows the best fit β-model for $S_{\rm X,CGM}$, and the green dash-dotted line the virial radius.

2024). Modeling of the emission and absorption lines, additionally requires the careful subtraction of multiple foreground sources (local hot bubble, galactic disc, solar wind charge exchange) in addition to an instrumental and cosmic X-ray background (Ponti et al., 2023). This has also made constraining the inner regions $r < 3\,\mathrm{kpc}$ of the corona challenging, since in this part of the sky contaimination from the galactic disk is most significant, and the emission from the Fermi and eROSITA bubbles also has to be taken into account (**?**).

In order to model the density of the corona, the temperature and metallicity of the gas often have to be assumed. Typically, the corona is assumed (motivated by spectral fitting, Henley & Shelton 2013; Ponti et al. 2023) to be isothermal with a temperature of $T \sim 2 \times 10^6\,\mathrm{K}$ (**?**Locatelli et al., 2024), but the metallicity still varies a lot from $Z = 0.1\,\mathrm{Z}_\odot$ (Locatelli et al., 2024) to $0.3\,\mathrm{Z}_\odot$ (**?**Li & Bregman, 2017) and up to even $0.5\,\mathrm{Z}_\odot$ (Faerman et al., 2017). In order to find a proper estimate of the coronal density, the metallicity is important since a low metallicity gas needs a higher density to produce the same emission compared to a higher metallicity gas. Recently, Ponti et al. (2023) have measured the metallicity of the corona to be considerably lower than the above assumptions, between $Z = 0.052 - 0.072\,\mathrm{Z}_\odot$, but with at most $Z \sim 0.1\,\mathrm{Z}_\odot$ still possible, considering the uncertainty in the extragalactic cosmic X-ray background. Such a metallicity is considerably lower than what has been used in many works (Miller & Bregman, 2013; **?**; Faerman et al., 2017; Li & Bregman, 2017) and therefore can have a significant impact on the inferred density and total mass of the Milky Way corona.

1.2.2 The corona around external galaxies

The corona around other nearby galaxies has mostly been observed in individual galaxies by directed pointings of *XMM-Newton* (Dai et al., 2012; Bogdán et al., 2013; Li et al., 2016; Anderson et al., 2016; Das et al., 2020), but these observations fail to detect emission of the corona beyond $70\,\mathrm{kpc}$. More recent observations from the eROSITA all-sky surveys (eRASS:4) (Zhang et al., 2024) have used stacking of multiple galaxies within $M_\star = 10^{10} - 10^{12}\,\mathrm{M}_\odot$ to successfully measure the emission from the corona beyond $100\,\mathrm{kpc}$ up to the virial radius, confirming the theoretical predictions about its extent. Moreover, assuming $Z = 0.1\,\mathrm{Z}_\odot$ and $T = 0.5\,T_\mathrm{vir}$, where T_vir is the virial temperature, for Milky Way-mass galaxies, the total mass of these coronae would be enough to account for all the missing baryons. However, a higher metallicity and/or temperature, would imply a significantly lower mass within the virial radius. To obtain a mass that is comparable to the mass predicted by the cosmological baryon fraction, the corona would then have to extend beyond the virial radius.

As an alternative to observing the X-ray emission of the gas, the thermal Sunyaev-Zeldovich Effect (SZE) (Sunyaev & Zeldovich, 1970) can also be used to measure the gas in the galactic corona. When radiation from the Cosmic Microwave Background (CMB) passes through a hot plasma, photons will scatter off the free electrons and this will produce a distortion in the spectrum. Since the CMB is an almost perfect black-body at $T_\mathrm{CMB} = 2.726\,\mathrm{K}$ over the entire sky, these distortions can be measured and converted to a total gas mass of the plasma (Birkinshaw, 1999; Cimatti et al., 2019). Due to the strength of the signal, this technique has mainly be used to study galaxy-clusters (for example, Vanderlinde et al., 2010) and massive early type galaxies (Greco et al., 2015), but is now observable for lower masses. Bregman et al. (2022) measured the SZE of the corona around 12 spatially resolved $L^\star$ galaxies. Stacking 11 of the lowest brightness galaxies gives a signal up to at least $250\,\mathrm{kpc}$ and the estimated average mass of the stacked coronae turns out to be $30\,\%$ of the missing baryons. Das et al. (2023) used the SZE to measure the coronal mass for galaxies between $M_\star = 10^{10.6 - 11.3}\mathrm{M}_\odot$ and concluded that the corona of galaxies with $M_\star = 10^{10.9 - 11.2}\mathrm{M}_\odot$ could be massive enough to reach the cosmological baryon fraction.

1.3 Gas accretion

We have seen that star forming galaxies require accretion of fresh new gas from the CGM to be able to continue forming stars (Fraternali & Tomassetti, 2012). Gas accretion is typically described as either *hot*-mode or *cold*-mode, depending on whether the halo is massive enough to shock heat the gas or not (Dekel & Birnboim, 2006; Dekel et al., 2009; Kereš et al., 2009). The mass threshold, is given by the shock-heating mass M_sh, which varies slightly with redshift and is around $M_\mathrm{sh} \approx (5 - 7) \times 10^{11}\,\mathrm{M}_\odot$ (Cimatti et al., 2019). If a galaxy is accreting in cold-mode ($M < M_\mathrm{sh}$), gas entering the halo from the IGM is not shock heated, allowing the cool $T \sim 10^4\,\mathrm{K}$ gas to reach the inner galaxy. This type of gas accretion can take place in the form of filaments. Gas in hot-mode accretion ($M > M_\mathrm{sh}$), instead, will be shock heated when it enters the halo and consequently will fill the halo with a diffuse atmosphere of gas around the virial temperature. This corona can still feed the galaxy if it is able to cool, for example via fountain accretion (Fraternali, 2017) or the formation of cooling flows (Stern et al., 2019; Hafen et al., 2022).

Since haloes grow over time via hierarichal merging, and the shock heating mass M_sh stays relatively constant over time, most haloes at high redshifts are expected to be accreting gas through cold-mode accretion. However, once they grew massive enough, accretion transitioned to hot-mode, so this mode is mostly important in the later stages of galaxy evolution. For the Milky Way halo, this transition from cold- to hot-mode accretion takes place somewhere after $z \approx 2$ (van de Voort et al., 2011) and but before $z \approx 1.5$ (Grønnow et al., 2024), which implies most of the stars in the Milky Way should have formed from the cooling of the corona, and not from cold-mode accretion.

1.3.1 Hot-mode accretion

When the halo of a galaxy is massive enough for the IGM gas to virialize as it is accreted, a large diffuse atmosphere, or hot CGM, forms around the galaxy. Dekel & Birnboim (2006) used this to help show why the star formation in massive haloes quenches. However, hot-mode accretion cannot correspond to the end of accretion of star-forming gas as in Milky Way-mass haloes star formation continues at a relatively constant rate, even after the formation of the hot corona. In

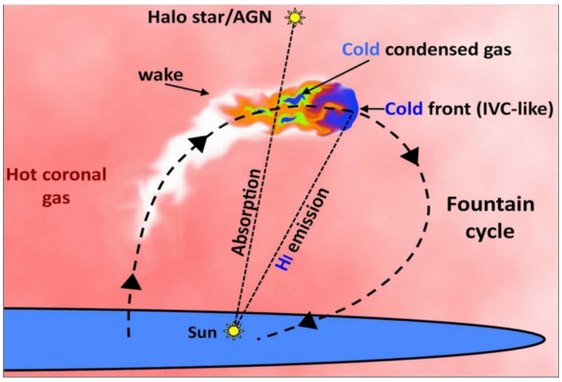

Figure 2: Schematic picture of the fountain accretion model, where a cold cloud is ejected from the disc by supernova feedback and travels through the hot coronal gas on a semi-ballistic trajectory. In the wake of the could, turbulent mixing between the cold and hot gas will trigger cooling of the hot gas. This cooled coronal gas will then fall back onto the disc together with the cloud gas, and be available to feed the star formation. Image taken from Fraternali et al. (2013).

the regime of hot-mode accretion, we therefore need a pathway for the gas to accrete from the hot CGM onto the galaxy, where it can feed star formation.

For massive cluster-scale haloes, there has long been the idea of gas from the hot CGM losing energy by radiative cooling and consequently compressing, forming a steady cooling flow towards the centre of the cluster (Fabian et al., 1984; Kaiser & Binney, 2003). Such a cooling flow would produce accretion rates of the order $10 - 100\,\mathrm{M_\odot/yr}$ and a central spike in emission in massive galaxies, both which are not observed. Radiative cooling of the gas must still take place, however, in order to stop the formation of a cooling flow, there needs to be a heating source that counterbalances the cooling, which is most likely a central AGN (McNamara & Nulsen, 2007). The sitiuation can be different in galaxy-size haloes, where cooling flow models have been recently revisited by Stern et al. (2019); Hafen et al. (2022). They build analytical solutions for a corona with steady-state cooling flows (see Section 2.5) that are able to reproduce the observed density distribution of the Milky Way (Li & Bregman, 2017) using a mass accretion rate equal to the Milky Way's observed SFR.

In an alternative scenario, thermal instabilities in the corona could form cool clouds through precipitation, and once formed they are pressure supported in the ambient corona. These clouds then lose orbital energy by ram pressure drag and eventually accrete onto the galaxy (Sormani & Sobacchi, 2019; Voit, 2021). However, several studies have shown that the formation of thermal instabilities are suppressed, disfavouring this accretion scenario (Binney et al., 2009; Joung et al., 2012).

Instead of a cooling mechanism that requires spontaneous thermal instabilities, the instabilities can also be induced by pertubations generated by the cool clouds ejected from the ISM, for instance by supernova-powered superbubbles (Fraternali, 2017). Such clouds will typically be ejected from the disc at high velocities and pass through the corona on a semi-ballistic trajectory. When this cool cloud then comes in contact with the hot corona, it will cool parts of the hot gas via turbulent mixing. The cooler coronal gas will then condense onto the wake of the cloud, which will return to the galaxy with this additional mass (Marinacci et al., 2010; Fraternali et al., 2013). These galactic 'fountains' can therefore be a medium for the galaxy to accrete gas effectively. A sketch of the fountain accretion model can be seen in Figure 2, originally from Fraternali et al. (2013).

1.4 Fermi and eROSITA bubbles

The Fermi and eROSITA bubbles (we will refer to them as the Milky Way bubbles) are large scale (height $\sim 10\,\mathrm{kpc}$), highly energetic structures, that are located above and below the Milky Way

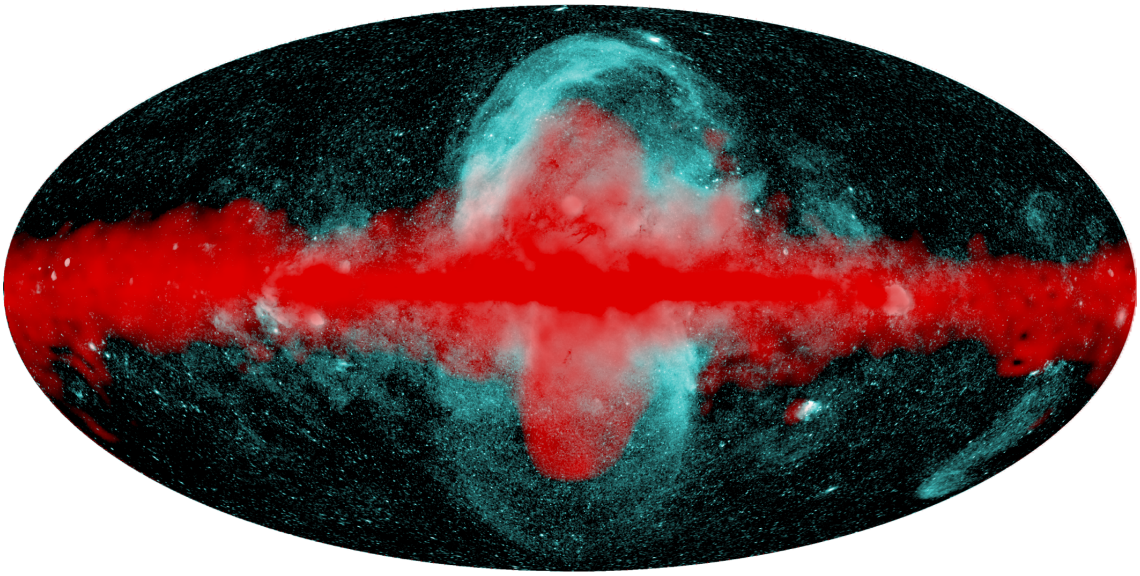

Figure 3: A composite, all-sky image of the Fermi and eROSITA bubbles. The cyan shows the extended X-ray emission from eROSITA (Predehl et al., 2020), which completely encloses the GeV emission from the Fermi bubbles shown in red (Selig et al., 2015). Image taken from Predehl et al. (2020).

disc. The bubbles have been discovered relatively recently in all sky gamma-ray (*Fermi*-LAT, Su et al., 2010) and X-ray (eROSITA, Predehl et al., 2020) surveys. Partial features of these bubbles were observed earlier, like the North Polar Spur in the X-ray ROSAT survey (Snowden et al., 1997), which turned out to align with the edge of the eROSITA bubbles. This feature was already interpreted early on by some Sofue (2000); Bland-Hawthorn & Cohen (2003) as the edge of a superwind bubble. The Fermi bubbles also coincide with the microwave haze (WMAP Finkbeiner, 2004), and both also emit a very hard spectrum, making their connection very likely (Yang et al., 2018). A composite image of the emission of the Fermi (Selig et al., 2015) and eROSITA (Predehl et al., 2020) bubbles can be seen in Figure 3. Here, we can clearly see the spatial correlation between the two structures, where the Fermi bubbles (red) are completely encompassed by the eROSITA bubbles (cyan).

The X-ray emmissivity of the eROSITA bubbles is mostly due to the thermal emission of the gas in the bubble and its shell. Most of the emission peaks in the $0.6 - 1.0\,\mathrm{keV}$ energy band of eROSITA which, taking into account the telescope response, corresponds to emission of a hot hot $k_\mathrm{B}T = 0.3\,\mathrm{keV}$ gas (Predehl et al., 2020). The Fermi bubbles are visible in gamma-rays, but here the exact emission mechanism is not yet certain. It is expected that the gamma-rays are produced by cosmic ray (CR) interactions, which can be *hadronic*, where the gamma-rays will be produced by collisions between protons and the hot gas via the decay of neutral poins, or *leptonic* where electrons generate gamma rays via inverse-Compton scattering of the interstellar radiation field. These models also depend on the mechanism that accelerates the CRs, which again is intimately tied to the formation mechanism of the bubbles (Yang et al., 2018).

Although several theories for the formation of the Milky Way bubbles exist, their exact origin is still unkown. Due to their position above and below the Milky Way galactic centre (GC), an energetic outburst from this region is a likely contender. This typically leaves two main candidates for the source of the bubbles, nuclear star formation (NSF) (Crocker et al., 2015) or past AGN activity from the central supermassive black hole, called Sgr A* (Zhang & Guo, 2020; Yang et al., 2022). Miller & Bregman (2016) and Predehl et al. (2020) both model the power of a continuously injecting central source, assuming the bubbles are a massive galactic outflow. They estimate the mechanical power of the source to be of the order of a few $10^{42}\,\mathrm{erg\,s^{-1}}$, together with an age of these bubbles of a few Myr to a few tens of Myr. Yang et al. (2022) instead show, using a hydrodynamical simulation, that a very short jet activity of time-scales of $0.1\,\mathrm{Myr}$ with a power of the order $10^{44}\,\mathrm{erg\,s^{-1}}$ is able to create the Milky Way bubbles as well.

Even though the corona of the Milky Way is orders of magnitudes larger than the bubbles, they still share an intimate connection. For instance, estimates of the formation of the Milky Way bubbles depend on the density of the ambient medium, where a higher inner density would result in a brighter X-ray signature near the galactic disc (Zhang & Guo, 2020). Moreover, the evolution of the corona is influenced by galactic feedback. For instance, powerful feedback, for example from an AGN, is able to heat gas in the corona, which would in turn decrease gas accretion and star formation (Fielding et al., 2020; Voit et al., 2024). Conversely, more gentle supernova feedback could act to stimulate gas accretion through the fountain accretion model (Fraternali, 2017). The Milky Way bubbles are a good example of galactic feedback in the Milky Way, and can therefore be useful to study the corona, and vice-versa.

1.5 Overview of the thesis

In this thesis, we study the evolution of a Milky Way-like corona using a semi-analytic evolutionary model. In Chapter 2, we explain the model, the various heating/cooling prescriptions, initial conditions for the evolution and numerical details of the model. At the end of the section, we also introduce a different analytic model of cooling flows in Milky Way-mass haloes which we compare our results to. Our results are presented in Chapter 3, separated in the evolution with only classical collisional ionisation equilibrium (CIE) cooling, cooling computed from non equilibrium codes with heating from the extragalactic ultraviolet background (UVB) and finally with heating from a central source. Here we also compare the results to the analytic model of cooling flows, and put our results in a physical context. In our discussion (Chapter 4), we compare the powers of possible sources of the Milky Way bubbles with our results, discuss assumption and some numerical details, and test another analytic model for cooling flows with rotation. Finally we summarize our findings and present our conclusions in Chapter 5.

2 Methods

In this chapter, we present the model that we use to evolve the corona of the Milky Way. In Section 2.1 we describe the physics of the model, show how we integrate the properties of the corona at a given timestep and derive how the entropy evolves as a consequence of heating or cooling. Then, we describe the various cooling and heating prescriptions that we employ in Section 2.2. The numerical details of the integration and evolution, and our initial conditionsfor the Milky Way's corona are in Sections 2.3 and 2.4 respectively. Finally, Section 2.5 describes an analytic model from the literature that describes a corona with steady-state cooling flows (Stern et al., 2019), which we use to compare our results with.

2.1 Physical model

The model that we will use in this thesis was introduced by Kaiser & Binney (2003) to investigate the evolution of the hot intracluster gas in the Hydra cluster. They assume that the gas around the Hydra cluster to be hydrostatic equilibrium, but evolves by the formation of a cooling flow through radiative cooling. Starting from an initial condition, as observed in X-ray by David et al. (2001), they evolve the gas with their model until a high ($n_{\mathrm{e}} > 0.3\,\mathrm{cm}^{-3}$) density in the centre is reached and the cooling becomes too high to proceed with the integration. At this time, $284\,\mathrm{Myr}$ after the start of the evolution, they assume a cooling catastrophy occurs occurs in the centre, and as a consequence the central AGN erupts and reheats the gas in the system. From this, they conclude that the next AGN outburst should occur in roughly the same time.

We apply the same model to the Milky Way corona but instead of considering only radiative cooling, we study how it evolves under various cooling and heating processes. Binney et al. (2009) have applied this model to a Milky Way-like corona as well, but only to study the formation of thermal instabilities. In this section, we focus on setting up and deriving the equations that describe the corona's pressure and mass, given a relation between the mass and entropy, and how such a corona evolves over time. We solve these equations numerically, a procedure that we describe in Section 2.3.

2.1.1 Static corona

For this model, we assume the corona to be a spherically symmetric, non-rotating body of gas, approximately in hydrostatic equilibrium. The potential of this system is assumed to be dominated by the potential of the dark matter halo $\Phi(r) \approx \Phi_{\mathrm{DM}}(r)$, which we assume stays constant over time. Hydrostatic equilibrium for the corona then reads

$$\frac{\mathrm{d}P(r)}{\mathrm{d}r} = -\rho(r)\frac{\mathrm{d}\Phi_{\mathrm{DM}}(r)}{\mathrm{d}r}, \tag{1}$$

where $P(r)$ and $\rho(r)$ are the pressure and density of the gas at radius r. Moreover, given the spherical symmetry, the variation of the gas mass within radius r, $M(r)$, is given as

$$\frac{\mathrm{d}M(r)}{\mathrm{d}r} = 4\pi\rho(r)r^2. \tag{2}$$

To solve the above equations, we need to know the density of the corona, which is actually one of the quantities that we aim to compute. To get around this we introduce another quantity, the entropy-index of the gas σ, which is defined as

$$\sigma \equiv \frac{P}{\rho^{\gamma}}, \tag{3}$$

where the adiabatic index $\gamma = C_{\mathrm{P}}/C_{\mathrm{V}}$, is the ratio of the specific heats under constant pressure (C_{P}) and constant volume (C_{V}). For a monatomic gas of point particles there are no internal degrees of freedom, so the adiabatic index is equal to $\gamma = 5/3$. The entropy-index relates to the specific entropy (entropy per unit mass) as

$$\mathcal{S} = C_{\mathrm{V}} \ln \sigma + \text{constant}. \tag{4}$$

Substituting Equation 3 back into Equations 1 and 2, one obtains (dropping the explicit dependence on r)

$$\frac{\mathrm{d}P}{\mathrm{d}r} = -\left(\frac{P}{\sigma}\right)^{1/\gamma} \frac{\mathrm{d}\Phi_{\mathrm{DM}}}{\mathrm{d}r}, \tag{5}$$

$$\frac{\mathrm{d}M}{\mathrm{d}r} = 4\pi \left(\frac{P}{\sigma}\right)^{1/\gamma} r^2, \tag{6}$$

which we can solve numerically as two coupled differential equations, given a relation between entropy-index and mass $\sigma(M)$, and boundary conditions for pressure and mass. The boundary condition for $M(r = 0) = 0$ is trivial, but we do not know $P(r = 0)$ beforehand, since this will depend on the density and temperature at $r = 0$, which in turn can vary over time. We therefore assume the corona is in pressure equilibrium with the external IGM, and no gas flows in or out of the system. The corona will then have a total mass M_{tot} at some outer radius R_{out}

$$M(R_{\mathrm{out}}) \equiv M_{\mathrm{tot}}, \tag{7}$$

where M_{tot} stays constant over time, and R_{out} is allowed to decrease (or increase) when the corona contracts (or expands). The pressure at R_{out}, then, has to be equal to the pressure of the external medium (P_∞), giving

$$P(R_{\mathrm{out}}) \equiv P_\infty, \tag{8}$$

which will remain constant over time. This then gives us an outer boundary condition for the pressure, making the problem of solving Equations 5 and 6 a two-point boundary value problem. We solve this by applying a shooting method (see Section 2.3.2), where we iteratively guess $P(r = 0)$ until the condition in Equation 8 is satisfied.

2.1.2 Time evolution

The corona obtained in the previous section will be in equilibrium, and stay that way forever if the entropy-mass relation does not change. Typically, there are processes that are able to add or remove entropy from the system, for instance through radiative cooling, or injection of energy by feedback from supernovae or AGN. We treat the evolution of the corona as a series of different equilibrium stages, or time-steps, where the evolution between the stages is based on the change in the entropy-mass relation, which we derive in this section. We note that it is most useful to focus on the change in entropy, as opposed to change in energy, since entropy is directly related to radiative heating and cooling, where energy also depends on work done by external factors. For example, when the system is cooling the system might lose some energy, but can regain part of it due to work done by the surrounding IGM when the system contracts.

The relation between specific entropy and heating and cooling processes is given by the heat equation (Clarke & Carswell, 2007)

$$\rho T \frac{\mathrm{d}\mathcal{S}}{\mathrm{d}t} = -\mathbb{L}(T, n_{\mathrm{H}}, Z, r, \ldots), \tag{9}$$

where we neglect all non-radiative terms, and define $\mathbb{L}$[1] as some heating / cooling function of energy per unit time per unit volume which can depend on various properties of the gas, like temperature, density and metallicity. We take the time derivative of the specific entropy: (Equation 4)

$$\dot{\mathcal{S}} = C_{\mathrm{V}} \frac{\dot{\sigma}}{\sigma}, \tag{10}$$

---

[1] This is similar to the quantity $\dot{Q}$ used for any change in heat in the system, but this typically also includes other processes like thermal conduction. So, to avoid confusion, we use $\mathbb{L}$ to denote the radiative energy exchange processes and volume. Using this definition, $\mathbb{L}$ is equal to $\rho\mathcal{L}$ as defined in Clarke & Carswell (2007).

and put this back into the heat equation (Equation 9) to obtain

$$\rho T C_{\rm V}\frac{\dot{\sigma}}{\sigma} = (\mu m_{\rm p} C_{\rm V}) n T\frac{\dot{\sigma}}{\sigma} = -\mathbb{L}, \tag{11}$$

where we used $\rho = \mu m_{\rm p} n$, with μ being the mean molecular weight, $m_{\rm p}$ the proton mass and n the number density of all particles in the gas. We can isolate $\dot{\sigma}$ and use $C_{\rm V}\mu m_{\rm p} = k_{\rm B}/(\gamma - 1)$ (see Appendix A.1), where $k_{\rm B}$ is the Boltzmann constant, which then gives us

$$\dot{\sigma} = -\sigma\frac{\gamma - 1}{k_{\rm B}}\frac{\mathbb{L}}{nT}. \tag{12}$$

To numerically find how entropy evolves, we use the Euler Method for solving differential equations (Press et al., 2007), which uses forward-difference to approximate the time derivative of the entropy-index

$$\dot{\sigma}(t) \approx \frac{\sigma(t + \delta t) - \sigma(t)}{\delta t}, \tag{13}$$

and then isolates $\sigma(t + \delta t)$

$$\sigma(t + \delta t) \approx \sigma(t) + \dot{\sigma}(t)\delta t, \tag{14}$$

to give the entropy at the next time step $\sigma(t + \delta t)$, as a function of the entropy at current time t, the analytic derivative $\dot{\sigma}$ and the step-size δt. Finally, we then use Equation 12 to find how the entropy changes as a function of cooling/heating as evaluated using the physical properties of the corona at time t:

$$\sigma(t + \delta t) \approx \sigma(t) - \sigma(t)\frac{\gamma - 1}{k_{\rm B}}\frac{\mathbb{L}}{nT}\delta t, \tag{15}$$

where $\sigma(t)$ and $\sigma(t + \delta t)$ are both functions of M, and all the other quantities are evaluated at the radius r that contain the mass M at time t.

With the new entropy-mass relation known at time $t + \delta t$, we can solve Equations 5 and 6 to find $P(r)$, $M(r)$ at $t+\delta t$, which we then use to find $\sigma(t+2\delta t)$ and so on. Repeating these two steps allows us to compute how the corona evolves over time. We note that Equation 15 is more general than Equation 10 from Kaiser & Binney (2003), which only considers radiative cooling. Of course, the evolution will mostly be determined by our choice of $\mathbb{L}$, which we discuss in Section 2.2.

It is instructive to rewrite the equations above in terms of a characteristic time-scale in which the energy of the system changes significantly (t_ϵ) due to radiative cooling or heating. For a nearly static fluid, where the velocity of the gas is much smaller than the sound speed, $v \ll c_{\rm s}$, the total energy of the system is approximately equal to its internal energy

$$\epsilon \approx U = \frac{k_{\rm B} n T}{\gamma - 1}, \tag{16}$$

where ϵ and U are the total and internal energy per unit volume. We assume the internal energy changes only through radiative cooling or heating, so

$$\dot{\epsilon} \approx -\mathbb{L}. \tag{17}$$

We then define t_ϵ to be the timescale in which the energy changes significantly, as the ratio of the total energy and its derivative

$$t_\epsilon \equiv \frac{\epsilon}{|\dot{\epsilon}|} \approx \frac{k_{\rm B} n T}{(\gamma - 1)|\mathbb{L}|}, \tag{18}$$

where we take the absolute value of $\dot{\epsilon}$, since $\mathbb{L}$ can be positive when the system is cooling down, or negative when the system is heating up. When we substitute the characteristic time-scale in Equation 12, we get

$$t_\epsilon = \frac{\sigma}{|\dot{\sigma}|}, \tag{19}$$

which shows that we can also interpret t_ϵ as the time-scale in which the entropy (index) changes significantly. Finally, Equation 15 with the characteristic time-scale substituted then reads

$$\sigma(t + \delta t) \approx \sigma(t)\left(1 - \mathrm{sgn}(\mathbb{L})\frac{\delta t}{t_\epsilon}\right). \tag{20}$$

where we multiply by the sign of $\mathbb{L}$ to account for the absolute value of $\mathbb{L}$ in Equation 18.

This form of the equation clearly shows us that change in entropy of the system is highest, whenever the characteristic time-scale is small. Moreover, when cooling is dominant ($\mathbb{L} > 0$), the entropy in the system will decrease, while heating ($\mathbb{L} < 0$) will make the entropy increase. We also see that whenever the system is cooling, Equation 20 shows us that in order for the entropy to stay positive, the step-size should be limited to $\delta t < t_\epsilon$. However, since we are using an Euler integration scheme, we have to keep the time-size low to reduce accumulation of large errors, so in practice we always keep $\delta t < t_\epsilon/10$ (see Section 2.3.3).

2.2 Cooling and heating processes

The evolution of the hot coronal gas will mostly be determined by the processes that remove entropy from or inject entropy into the gas. In our model, $\mathbb{L}$ describes this as the rate per unit volume ($\mathrm{erg\,s^{-1}\,cm^{-3}}$) that is heated ($\mathbb{L} < 0$) or cooled ($\mathbb{L} > 0$). In this Section, we describe three prescriptions for cooling and/or heating that we use to evolve the corona. These are the scenario of only cooling from a classical cooling function, cooling with heating from the extragalactic UVB, and cooling with heating from a central source.

Typically, the most important factor which determines how much a gas cools radiatively, depends on temperature and metallicity. The temperature mainly determines the state of hydrogen atoms in the system, ionised or neutral (ionised for $T \gtrsim 10^4\,\mathrm{K}$) and for an ionised gas, which processes will be important in ionisation/recombination and (de-)exitation of atoms in the gas. For the corona of the Milky Way, with a temperature around $T \sim 10^6\,\mathrm{K}$ being significantly above the threshold for ionisation of H and He, we consider the system to be fully ionised. The metallicity of the gas is mainly important at temperatures around $T \sim 10^5 - 10^6\,\mathrm{K}$, since here the majority of the cooling comes from metal ions (C, O, Fe, Si, N and Ne). Therefore, a gas that has a higher fraction of metals, will therefore also cool more efficiently (Maciel, 2013; Cimatti et al., 2019).

For this thesis, we assume the gas to be always fully ionised, which implies that the atomic number density n_t (neutral atoms and ions) will be equal to the number of ions n_i

$$n_\mathrm{t} \approx n_\mathrm{i}. \tag{21}$$

The total number of particles, is then

$$n \approx n_\mathrm{i} + n_\mathrm{e} \tag{22}$$

where n_e is the number density of electrons, where we assume the ratio between the ions and electrons to be $n_\mathrm{e} \approx 1.2 n_\mathrm{i}$ due to the contribution of Helium. For the mean molecular weight, we take a value of $\mu = 0.62$. These assumptions will only be valid for temperatures above $T \geq 10^5\,\mathrm{K}$, and we would need different values for lower temperatures. In practice, however, the temperature in the evolution will remain above $10^5\,\mathrm{K}$ (see discussion in Section 4.2.4), so we do not need to consider calculations for a medium which is not fully ionised.

2.2.1 Radiative cooling in collisional ionisation equilibrium (CIE)

The density of the gas, assuming it is optically thin such that radiation can escape the system, will mainly determine the rate of collisional ionisation and collisional excitation. If the density of the gas is high enough for these collisions to dominate ionisation, we can approximate the gas to be in collisional ionisation equilibrium (CIE), which assumes that there is a perfect balance between collisional ionisation and recombination rates. In addition, CIE assumes there is no heating from the photoionisation. Classically, the CIE cooling functions from Sutherland & Dopita (1993) (hereafter SD1993) have been used, so we will use them as our most basic prescription for cooling (see Section 2.2.1). Using such a cooling prescription is also most analogous to the original application of the model, by Kaiser & Binney (2003) on the evolution of the Hydra cluster.

Assuming CIE, the rate of radiative cooling can be written as

$$\mathbb{L} = n_\mathrm{e} n_\mathrm{t} \Lambda_\mathrm{CIE}(T, Z) \tag{23}$$

where n_e and n_t are the electron and atom density of the gas, and $\Lambda_\mathrm{CIE}(T, Z)$ is the CIE cooling function (in $\mathrm{erg\,s^{-1}\,cm^{3}}$) from SD1993 that only depends on temperature and metallicity of the

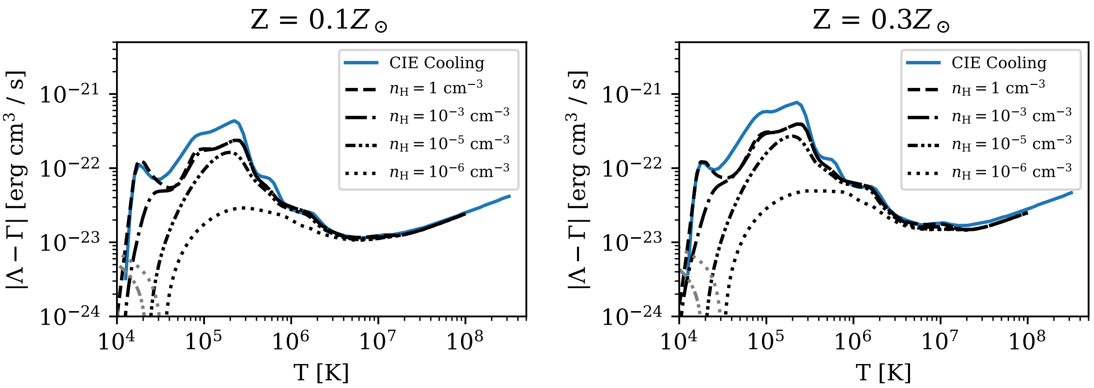

Figure 4: Net cooling functions (cooling Λ minus heating Γ) from SD1993 (blue line, $\Gamma = 0$) and `CLOUDY` (Ferland et al., 2013) with photoionization from extragalactic UVB from Haardt & Madau (2012) for hydrogen densities in the range $n_{\rm H} = 1 - 10^{-6}\,{\rm cm}^{-3}$ (black lines). The black and blue lines indicate that cooling is dominant, and the gray lines denotes that heating is dominant. The figure on the left shows the net cooling functions for $Z = 0.1Z_\odot$ and the figure on the right for $Z = 0.3Z_\odot$.

gas. The blue line in Figure 4 shows how $\Lambda_{\rm CIE}(T, Z)$ varies as a function of temperature, for two metallicities. In this case, there is no heating in the system, so the sytem can cool indefinitely to temperatures below $T \lesssim 10^4$ K, where the gas no longer will be ionised and CIE no longer holds. We therefore put an artificial temperature floor in the cooling function

$$\Lambda_{\rm CIE}(T, Z) = 0, \qquad \text{for } T \leq 10^{4.2}\,{\rm K}, \tag{24}$$

to halt the cooling.

For a system that is only cooling ($\mathbb{L} > 0$), the characteristic time-scale in which energy changes significantly, becomes equal to what is commonly defined as the cooling time $t_{\rm cool}$ (Cimatti et al., 2019)

$$t_\epsilon = t_{\rm cool}, \qquad \text{for } \mathbb{L} > 0. \tag{25}$$

In this case, Equation 18 then becomes

$$t_\epsilon = t_{\rm cool} \approx \frac{2.2 k_{\rm B} T}{(\gamma - 1) n_{\rm e} \Lambda_{\rm CIE}(T, Z)}, \tag{26}$$

where we have used Equations 23 together with $n_{\rm t} \approx n_{\rm i}$, $n \approx n_{\rm e} + n_{\rm i}$ and $n_{\rm e} \approx 1.2 n_{\rm i}$ to rewrite the characteristic time-scale in terms of $n_{\rm e}$ and $\Lambda_{\rm CIE}$.

2.2.2 Cooling with heating from photoionisation

Since the Milky Way corona can have a density as low as $n_{\rm e} \sim 10^{-5}\,{\rm cm}^{-3}$ at large radii (**?**), assuming CIE will no longer be valid. Our second cooling prescription therefore uses `CLOUDY` (Ferland et al., 2013) to calculate a rate of cooling which is also valid at these lower densities. `CLOUDY` is a full plasma simulation code, that is able to calculate the cooling or heating rates in non-equilibrium gasses. It is therefore able to calculate rates for densities where CIE is no longer valid. Moreover, it is possible to consider heating from photoionisation as well, where we choose to add photoionisation from the local extragalactic ultraviolet background (UVB) at $z = 0$ (Haardt & Madau, 2012). This source of photoionisation should be present throughout the Milky Way corona, and could reduce the net cooling rate of the gas.

The cooling/heating rate are given by tables from `CLOUDY`, which are identical to those used by Afruni et al. (2023), they directly give

$$\mathbb{L} = \mathbb{L}_{\texttt{CLOUDY}}(T, Z, n_{\rm H}), \tag{27}$$

where n_H is the number density of hydrogen atoms (neutral and ionised). Obtaining the hydrogen number density from the density ρ is not immediately obvious, since this depends on the metallicity of the gas. However, for a given metallicity Z, the proportionality between n_H and ρ is fixed for all T:

$$n_\mathrm{H} = a(Z)\rho, \tag{28}$$

where $a(Z)$ is this proportionality constant depending on metallicity. We compute $a(Z)$ directly from the tables. These tables are then interpolated using a a Piecewise Cubic Hermite Interpolating Polynomial (PCHIP) (Fritsch & Butland, 1984), because linear interpolation was not accurate enough and quadratic or higher order methods occasionally produced incorrect values due to dramatic oscillations between control points in the interpolating polynomial.

The rates from `CLOUDY` with UVB for varying densities can be seen in Figure 4 as black or grey lines depending on whether cooling or heating dominates. We see that around $T = 10^5$ the CIE cooling function SD1993 is significantly higher, compared to the highest density in `CLOUDY` ($n_\mathrm{H} = 1\,\mathrm{cm}^{-3}$) which should also approach CIE. Moreover, for densities ($n_\mathrm{H} = 10^{-5}$ – $10^{-6}\,\mathrm{cm}^{-3}$), we see that cooling is significantly lower compared to higher densities. For these low densities, heating also becomes dominant at and below the temperature $T \lesssim 3 \times 10^5\,\mathrm{K}$.

As opposed to the case of SD1993, there is now a heating factor from the UVB which is most significant at low temperatures (10^3 – $10^4\,\mathrm{K}$ depending on metallicity). We therefore no longer need a temperature floor to halt the cooling at these low temperatures.

2.2.3 Heating from a central source

So far the cooling and heating processes we have considered are all based on physical quantities of the gas temperature, density and metallicity and are independent on the position within the corona. However, the corona is most likely influenced by feedback from the galaxy in the centre of the system only, which would make the heating/cooling prescription dependent on radius r. Our main motivation for adding such a central source is the presence of the Milky Way bubbles (Su et al., 2010; Predehl et al., 2020) which likely have been created by some energetic source in the galactic centre (GC) of the Milky Way. The implementation of this central heating source, follows an approach motivated by AGN feedback models from simulations (Springel et al., 2005; Weinberger et al., 2017). In these models, given some power of an AGN $\dot{E}_\mathrm{tot}$ (typically calculated based on the accretion rate of the AGN), they inject this energy, weighted by a kernel, into the gas as thermal energy. Such a kernel $\dot{E}(r)$ is dependent on position and can have any shape, as long as its total power integrated over the entire volume equals $\dot{E}_\mathrm{tot}$

$$\dot{E}_\mathrm{tot} = \iiint \dot{E}(r)dV\,. \tag{29}$$

We note here that if the power $\dot{E}_\mathrm{tot}$ is energy per unit time, then the kernel $\dot{E}(r)$ will be energy per unit time per unit volume. For this work, we use a spherically symmetric Gaussian kernel, centered at $r = 0$, which, following the above condition for normalisation, is then given as

$$\dot{E}(r) = \frac{\dot{E}_\mathrm{tot}}{(2\pi\lambda^2)^{3/2}} \exp\left[-\frac{r^2}{2\lambda^2}\right], \tag{30}$$

where λ is the standard deviation, which defines the length scale of the kernel. More precisely, λ defines the radius where 68 % of the total energy is given to the gas inside this radius.

Finally, we include this central heating based on position of the gas into our model by adjusting $\mathbb{L}$ based on `CLOUDY` with the UVB. The cooling/heating rate of a gas with a given temperature, density and metallicity at radius r from the centre is then simply the rate calculated by `CLOUDY`, based on properties of the gas, plus the energy injected at position r by the central source:

$$\mathbb{L} = \mathbb{L}_\mathtt{CLOUDY}(T, n_\mathrm{H}, Z) + \dot{E}(r) \tag{31}$$

where the central power $\dot{E}_\mathrm{tot}$, and scale λ are constants set depending on the model run.

We note that so far, the heating and cooling have been via radiation only. The thermal energy injected from the central source, however, is best interpreted as mechanical energy, since it does not influence the calculation of the cooling/heating rates by `CLOUDY`. Radiative feedback from the central source may be important as well (for instance from Sgr A* Bland-Hawthorn et al., 2019), but is not considered here (see Section 4.4).

2.2.4 Convection

The various energy exchange processes described above have no constraints that would keep the corona safe from instabilities. A region that decreases in entropy with outgoing radius, $\frac{\partial S}{\partial r} < 0$, will be convectively unstable (Balbus, 1995; Clarke & Carswell, 2007). In our initial condition (see Section 2.4) a negative entropy gradient exists around $r = 1\,\mathrm{kpc}$, and evolving the corona results in this negative gradient increasing even further. Moreover, the prescription that includes heating from a central source will only increase the entropy in the centre, which will result in a large convectively unstable region if the power of the source is high enough.

We therefore implement a simple form of convection similar to what is done in Binney et al. (2009), that we can apply to our initial condition to remove the unstable region, and apply at each time-step to avoid unstable regions from forming. The method works iteratively and follows

1. find a region that is convectively unstable,
2. calculate the mass-weighted average entropy-index in this region $\bar{\sigma}$,
3. set the entropy-index of the entire region to this average value,
4. repeat if convectively stable regions still exist.

The mass-weigthed average entropy-index for the convectively unstable region is given by (see Appendix A.2)

$$\ln \bar{\sigma} = \frac{\sum_i \ln[\sigma(r_i)] T(r_i) m(r_i)}{\sum_i T(r_i) m(r_i)} \tag{32}$$

where $m(r_i)$ is the gas mass in a shell at radius r_i, $T(r_i)$ the temperature at r_i, and $\sigma(r_i)$ is the entropy-index at r_i before the convective method is applied. The sum over i indicates that we sum over all radii r_i in the region with decreasing entropy-index. We note that we have to sum (and not take the integral), since we apply this method to our corona which we integrate numerically. The values of entropy, temperature and mass as a function of radius are therefore discrete and the size of these 'cells' is determined by the radial step-size of the integrator of the corona (see Section 2.3.1). We consider the shell at r_i to extend from r_{i-1} to r_i, so the mass in the shell is then given by the difference in total mass $m(r_i) = M(r_i) - M(r_{i-1})$, starting at $m(0) = 0$.

Since we remove convectively unstable regions at each time-step, the time-scale on which the convection takes place should ideally be of the same order. We discuss the implications of this in Section 4.2.3.

2.3 Numerical details

In Section 2.1 we have outlined a model that can describe the evolution of a spherical corona in consecutive phases of hydrostatic equilibrium. The evolution of this model proceeds through two main steps that are performed numerically

1. Given some entropy-mass relation at time t $\sigma_t(M)$, and time independent boundary conditions for $M(r = 0) = 0$ and $P(R_{\mathrm{out}}) = P_\infty$, intregrate Equations 5 and 6 to find the pressure $P_t(r)$ and mass $M_t(r)$ profiles of the corona at time t.
2. Given the properties of the corona at time t, $P_t(r), M_t(r), \sigma_t(M)$, update the entropy-mass relation for the next time-step $\sigma_{t+\delta t}(M)$, using Equation 15.

In this Section we will explain the details of the numerical integration of a corona (Section 2.3.1) given some $P(r = 0), M(r = 0)$ and $\sigma(M)$. We then show in Section 2.3.2 how we repeat this integration with different $P(r = 0)$ until we satisfy the outer boundary condition $P(R_{\mathrm{out}}) = P_\infty$. Sections 2.3.3 and 2.3.4 describe the details of the update in entropy and the stopping conditions for the evolution. Finally, Section 2.3.5 explains how we compute the mass accretion rate and velocity of the gas, given a fully evolved corona. Figure 5 shows a schematic overview of how we evolve the corona.

2.3.1 Integration of the static corona

Equations 5 and 6 are two coupled first order ordinary differential equation (ODE). We solve these equations numerically with a Runge-Kutta method (Press et al., 2007), given initial conditions for $P(0), M(0)$ and entropy-mass relation $\sigma(M)$. We make solving the ODEs's explicit, by casing Equations 5 and 6 into normal form (Landau et al., 2015):

$$\frac{\mathrm{d}\mathbf{y}}{\mathrm{d}r} = \mathbf{f}(r, \mathbf{y}), \quad \mathbf{y} = [P, M]^T, \quad \mathbf{f}(r, \mathbf{y}) = [f_0(r, \mathbf{y}), f_1(r, \mathbf{y})]^T, \tag{33}$$

$$\frac{\mathrm{d}P}{\mathrm{d}r} = f_0(r, \mathbf{y}) = g(r)\left(\frac{P}{\sigma(M)}\right)^{1/\gamma}, \tag{34}$$

$$\frac{\mathrm{d}M}{\mathrm{d}r} = f_1(r, \mathbf{y}) = 4\pi r^2\left(\frac{P}{\sigma(M)}\right)^{1/\gamma}, \tag{35}$$

where the acceleration due to the gravitational potential $g(r)$ is defined as $g(r) \equiv -\mathrm{d}\Phi(r)/\mathrm{d}r$ and is assumed to be a known analytic function. Since we solve the equations numerically, the resulting pressure and mass profiles are discrete and only known at specific radii determined by the step-size of the integrator. This also means that $\sigma(M)$ is discrete, so we use linear interpolation[2] to evaluate σ for any M between 0 and M_{tot}.

The integrator we use to get $P(r), M(r)$ is an eighth order ($\mathcal{O}(h^8)$, where h is the step-size) Dormand-Prince (Dormand & Prince, 1980) embedded method (`Dopr853`[3]) outlined by Press et al. (2007) in Section 17.2.4, based on the implementation of Hairer et al. (1993). This method uses a PI (proportional- and integral feedback) stepsize controller, to determine the step-size in r at each step of the integrator. This assures that the method has a good balance between precision, by not taking steps that are too large, and computational cost, by not taking steps that are too small. Moreover, at each step the integrator is able to provide *dense* output, meaning it is able to evaluate $P(r), M(r)$ for $r_{i-1} \leq r \leq r_i$, where r_{i-1} and r_i are the radius at the previous and current step of the integrator, up to seventh order.

The integrator proceeds with steps in r, starting from $r = 0$, and stops at $r = R_{\mathrm{out}}$. We, however, do not know R_{out} a priori since it is defined to be the radius where the total mass is equal to M_{tot} (Equation 7). To find R_{out}, we integrate until the mass at the current step $M(r_i)$ exceeds M_{tot}. At this point, we know that M_{tot} is between mass of the previous and current step, which is equivalent to R_{out} being between the radius of the previous and current step

$$M(r_{i-1}) \leq (M_{\mathrm{tot}} \equiv M(R_{\mathrm{out}})) < M(r_i) \quad \Longleftrightarrow \quad r_{i-1} \leq R_{\mathrm{out}} < r_i. \tag{36}$$

We then find R_{out} using a root finding method on the *dense* output of the integrator between r_{i-1} and r_i. The root finding method is a *Secant* method from Press et al. (2007), since the dense output is a cubic polynomial and is therefore guarenteed to be smooth around the root. We modify the implementation of the Secant method slightly to stop the root finding method whenever $M(r) - M_{\mathrm{tot}} < M_{\mathrm{tot}}/10^6$.

Finally, the result of the integration is that we know the pressure $P(r)$ and mass $M(r)$ profiles for discrete r between 0 and R_{out} :

$$\texttt{integrate}[P(0), M(0), \sigma(M)] \quad \rightarrow \quad P(r), M(r) \ \text{ for } r \in [0, r_2, r_3, \ldots, r_{N-1}, R_{\mathrm{out}}]. \tag{37}$$

2.3.2 Boundary condition for pressure

The integrator from the previous section is able to solve Equations 5 and 6 numerically given pressure and mass at $r = 0$. However, as we have described in Section 2.1.1, our boundary

---

[2] We tried higher order (quadratic and quintic) interpolation as well, but due to excessive oscillations between control points these schemes gave incorrect values.

[3] C++ implementation available at the webnote: Numerical Recipes Software 2007, "Routine Implementing an Eighth-order Runge-Kutta Method," *Numerical Recipes Webnote No. 20* https://numerical.recipes/webnotes/nr3web20.pdf

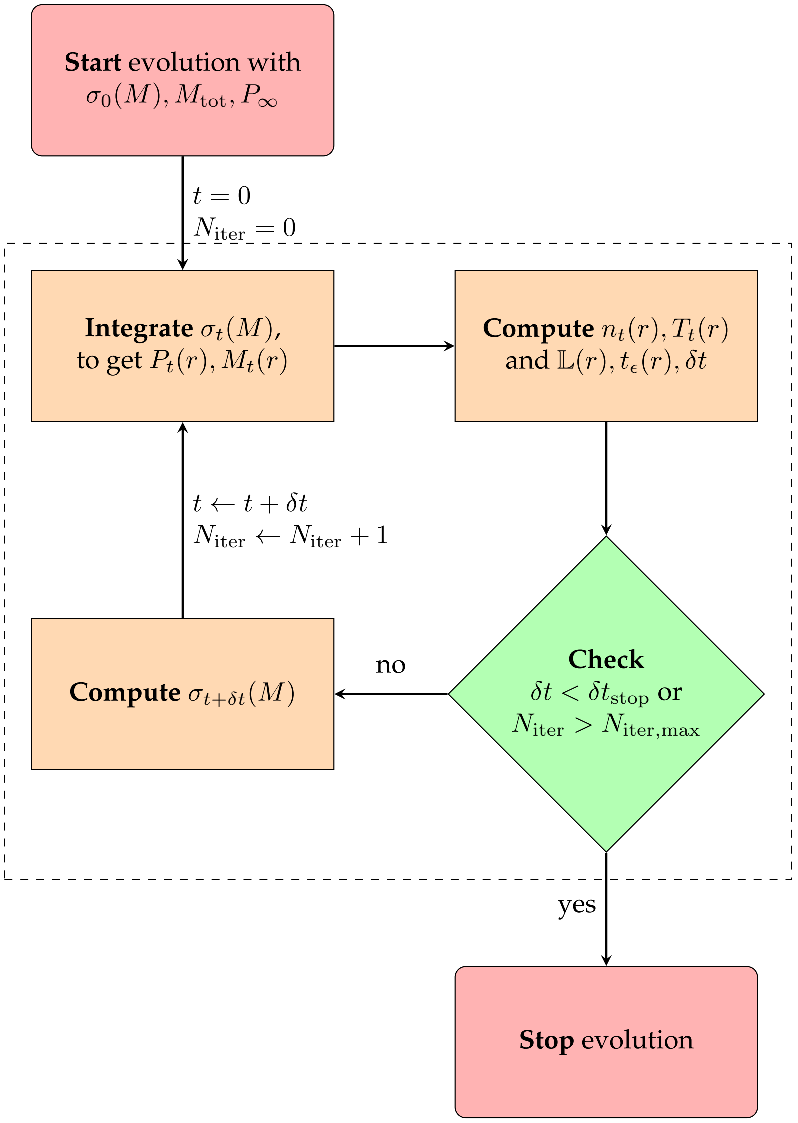

Figure 5: Schematic of the different steps involved in the evolution, starting from initial conditions (Section 2.4). The core loop of the evolution, inside the dashed box, consists of integrating the corona (Sections 2.3.1 and 2.3.2), computing quantities for the time-step (Section 2.3.3), checking stopping conditions (Section 2.3.4) and updating entropy (Section 2.3.3). If the method for convection is used (Section 2.2.4), it is applied after the corona is integrated.

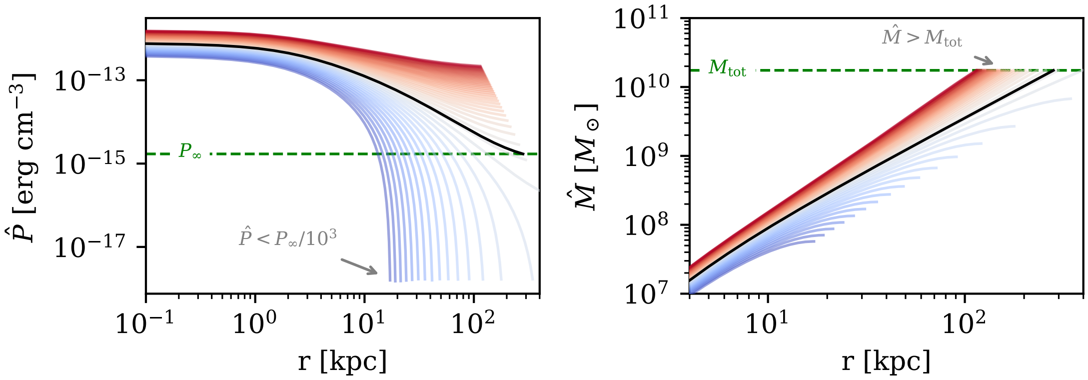

Figure 6: Example of the shooting method in action, where we see pressure (left) and mass (right) for varying trials of $\hat{P}_0$. The profiles are indicated by blue ($\hat{P}_0$ too low) or by red ($\hat{P}_0$ too high), compared to the corona that satisfies the boundary condition in black. The target values for the outer boundary condition (P_∞ and $M_{\rm tot}$) are shown as green dashed horizontal lines. The regimes where the profiles hit one of the two stopping conditions $\hat{P}(r)$ too low or $\hat{M}(r)$ greater than $M_{\rm tot}$, are indicated by grey arrows. This example is created using the `mb2016` initial condition (see Section 2.4).

condition for the pressure in our corona (Equation 8) is given at the outer radius $R_{\rm out}$. Instead of a standard initial value problem, which we can directly solve by applying our method outlined in the previous section, we have a *two-point boundary value problem*, which requires some additional steps to fully solve. The most straightforward method of solving such a two point boundary value problem, is by using a *shooting method* (Press et al., 2007), which iteratively guesses values for the pressure at $r = 0$, until the outer boundary condition is satisfied.

More precisely, given a trial value for the central pressure $\hat{P}(0)$ (we use the hat to indicate a trial corona), we integrate the corona to obtain the full pressure and mass profiles

$$\texttt{integrate}\Big[\hat{P}(0), M(0), \sigma(M)\Big] \quad \rightarrow \quad \hat{P}(r), \hat{M}(r) \;\; \text{for } r \in [0, \hat{r}_2, \hat{r}_3, \ldots, \hat{r}_{N-1}, \hat{R}_{\rm out}]. \tag{38}$$

When the trial corona gives an outer pressure value $\hat{P}(\hat{R}_{\rm out})$ that is close enough to the boundary condition

$$\Big|\hat{P}(\hat{R}_{\rm out}) - P_\infty\Big| < \frac{P_\infty}{10^6}, \tag{39}$$

we accept the trial corona as the real corona. Otherwise, we refine our guess for $\hat{P}(0)$ and repeat the process. This process is actually also a root finding problem, and we use *bisection* (Press et al., 2007) to find $P(0)$ that satisfies Equation 39. Again, we also modify the original *bisection* algorithm to stop whenever $\hat{P}(\hat{R}_{\rm out})$ and P_∞ are close.

Figure 6 shows the shooting method in action, where we see the trial pressure (left) and mass (right) profiles for varying starting values $\hat{P}_0$. The corona that satisfies the boundary conditions (green dashed lines) is indicated by the black line. The trial coronae that have $\hat{P}(0)$ too high are indicated by red. We see that they reach the stopping condition on $\hat{M} > M_{\rm tot}$, but the $\hat{P}(\hat{R}_{\rm out})$ is too high, so they are not accepted. The pressure of trial coronae that have $\hat{P}(0) < P(0)$, indicated by blue, decreases too rapidly to reach $M_{\rm tot}$. Since pressure can only decrease with radius, we stop the integrator early whenever

$$\hat{P}(r_i) < \frac{P_\infty}{10^3} \tag{40}$$

since we know that it will never satisfy the boundary condition. Stopping the integration early saves a lot of computational time, but makes the landscape for the root finding problem unreliable at $\hat{P}(0) \ll P(0)$. We can see this in Figure 7, which shows the result of the integration $\hat{P}(\hat{R}_{\rm out})$ as

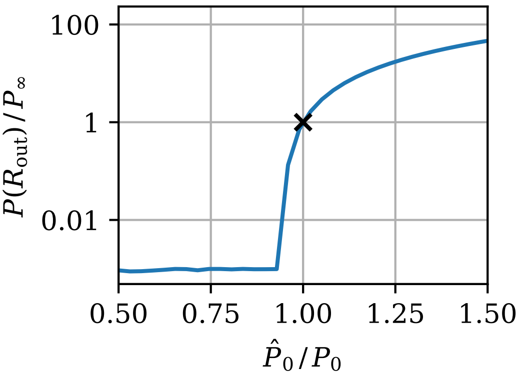

Figure 7: Example of the curve that is optimized when we integrate the corona. The horizontal axis shows the trial $\hat{P}_0$ normalized to 1 being the true value of P_0, and the vertical axis shows the resulting $P(R_{\rm out})$ at the end of the integration, also normalized to the target value P_∞. The target for the optimization is indicated by a black cross. The flat section in the bottom left side of the plot shows the effect of early stopping when pressure is too low. The full pressure and mass curves that created this graph can be seen in Figure 6.

a function of the trial value $\hat{P}(0)$. Both axes are normalized to the reference values (P_∞ and $P(0)$), such that the value that we are looking for is at (1, 1). The flat region of the curve on the left side indicates the early stopping of the integrator.

2.3.3 Updating the entropy-mass relation

The previous two Sections describe how at a time t, given some $\sigma_t(M)$, the corona is integrated to obtain pressure $P_t(r)$ and mass $M_t(r)$ for r between 0 and $R_{\rm out}$. We now describe how we compute the change in entropy of the corona, given some prescription for heating/cooling (Section 2.2).

The change in entropy, from $\sigma_t(M)$ to $\sigma_{t+\delta t}(M)$, is given by Equation 15. For this, we need to compute total number density $n(r)$, and temperature $T(r)$ from the pressure $P(r)$, mass $M(r)$ and entropy $\sigma_t(M)$. First, we can compute the density ρ directly form the definition of entropy-index (Equation 3), and use this to compute $n = \rho/\mu m_{\rm p}$, where we assume the mean molecular weight to be $\mu = 0.62$. Using the ideal gas law we can calculate the temperature of the coronal gas as

$$T = \frac{P}{nk_{\rm B}}. \tag{41}$$

Since we want density and temperature as a function of radius, but entropy-index is given as a function of mass, we compute the entropy as a function of r by evaluating it at the mass at that radius $\sigma_t(r) = \sigma_t(M(r))$. Finally, we compute $\mathbb{L}$, using the temperature and density, according to any of the presciptions presented in Section 2.2.

Updating the entropy using Equation 15 requires us to make a choice for the step-size δt. From the update rule in terms of the time-scale of energy/entropy change t_ϵ (Equation 20) we see that whenever the corona is cooling ($\mathbb{L} > 0$) and $t_\epsilon < \delta t$, the update rule will cause the entropy-index to be negative, which is unphysical. Moreover, the update rule is an Euler method, which requires a small step-size to reduce the accumulation of large errors. So also in the case of heating ($\mathbb{L} < 0$), we want to keep the step-size small if the change in energy is large. Therefore, if t_ϵ is large, we choose a constant value for the step-size δt_0 between 0.1 – $1\,\mathrm{Myr}$. But when the timescale is of the same order as this value, we reduce the step-size to be a factor 10 smaller than t_ϵ. Together this gives

$$\delta t = \min\left(\delta t_0,\ \frac{\min\limits_r t_\epsilon(r)}{10}\right), \tag{42}$$

where we take the minimal value of $t_\epsilon(r)$, because the timescale can vary with radius.

With $\sigma_{t+\delta t}(M)$ known, we then integrate the corona again to obtain $P_{t+\delta t}(r)$ and $M_{t+\delta t}(r)$. In the cases where we include convection in our model (Section 2.2.4), we compute $\sigma_{t+\delta t,\mathrm{conv}}(M)$ based on the corona at $t + \delta t$, and then integrate to obtain $P_{t+\delta t,\mathrm{conv}}(r)$ and $M_{t+\delta t,\mathrm{conv}}(r)$ for the corona where convectively unstable regions have been removed.

2.3.4 Stopping conditions for the evolution

The cyclic process of integrating the corona and updating the entropy can in principle continue forever using an arbitrarily small δt, so we put two stopping conditions on the evolution. First we put a limit on the total number of iterations $N_{\mathrm{iter,max}}$, where we stop if the evolution reached

$$N_{\mathrm{iter,max}} = 4000 \tag{43}$$

iterations. For an initial step-size of $\delta t_0 = 0.1\,\mathrm{Myr}$, this will mean the corona will evolve for a maximum of $400\,\mathrm{Myr}$.

In practice, however, we typically see that the time-scale of energy change t_ϵ becomes low before this limit is reached. In a situation where the corona primarily cools, it will result in a decreasing t_ϵ, and consequently will cool even more (for instance, see Section 3.1). This will cause δt to decrease rapidly (Equation 42), and the corona will no longer evolve in time. To reduce wasteful computation when δt becomes too low long before the iteration limit is reached, we stop the evolution whenever the step-size is below the lower limit δt_{stop}, which we set at

$$\delta t_{\mathrm{stop}} = 0.01\,\mathrm{Myr}. \tag{44}$$

We discuss how these stopping conditions impact our results in Section 4.2.4.

2.3.5 Derived quantities

By evolving the corona, we can compute some additional observable quantities such as the mass accretion $\dot{M}$ and the radial velocity v_r. We calculate these quantities after we have completed the evolution of our model, so they have no impact on the evolution itself.

The straightforward method of computing the mass accretion is to use the forward difference approximation (Press et al., 2007):

$$\dot{M}(t) \approx \frac{M(t+\delta t) - M(t)}{\delta t} \tag{45}$$

where $M(t)$ and $M(t + \delta t)$ are the masses at subsequent evolutionary steps, separated by δt. However, this method does not work well when the timestep δt is very small, resulting in the denominator blowing up. We therefore take another approach, taking into account multiple steps of the evolution to estimate the mass accretion: To compute the mass accretion at radius r at time t, $\dot{M}_t(r)$, we take all masses at r between t and $t + \Delta t$:

$$M_t(r),\ M_{t+\delta t}(r),\ M_{t+2\delta t}(r),\ \ldots,\ M_{t+\Delta t}(r), \tag{46}$$

where Δt is larger than the timestep between evolutions δt. We then assume that the increase in mass within this interval t to $t + \Delta t$ is linear, so we can fit a linear model through these points. The slope of this line, will then give our value for $\dot{M}_t(r)$. We can then repeat this fit for multiple radii to get $\dot{M}_t(r)$ across the entire corona.

Using the mass accretion, we can also compute the radial velocity of the gas in the corona. For this, we assume that the mass in the system is conserved, meaning a change in mass at radius r, must be caused by gas flowing from or to adjacent shells. The continuity equation, then gives us v_r:

$$\dot{M} + 4\pi\rho r^2 v_r = 0 \qquad \Longrightarrow \qquad v_r = -\frac{\dot{M}}{4\pi\rho r^2}, \tag{47}$$

where $\dot{M}$ and ρ are the mass accretion and density at radius r. Note that when mass flows towards the galaxy, $\dot{M}$ will be positive and consequently the radial velocity will be negative. The radial velocity therefore measures how fast the gas is moving away from the galaxy.

2.4 Application to the Milky Way

Our aim is to study the evolution of a Milky Way-like corona, so therefore our initial conditions will be based on Milky Way observations. For our system we need to specify the dark matter halo, and density of the gas in the corona. Our model focuses on a corona without the presence of a galactic disc, so we do not consider this component in our initial condition.

2.4.1 Dark matter halo

We assume that the Milky Way potential is completely dominated by the potential of the dark matter halo, which we take to be a Navarro-Frenk-White (NFW) potential (Navarro et al., 1997). The density distribution of such a potential is then given by (Cimatti et al., 2019)

$$\rho(r) = \frac{4\rho_\mathrm{s}}{(r/r_\mathrm{s})(1+r/r_\mathrm{s})^2}, \tag{48}$$

where r_s is the scale radius and ρ_s the density at the scale radius. The potential at radius r is then

$$\Phi(r) = -16\pi G\rho_\mathrm{s} r_\mathrm{s}^2 \frac{\ln(1+r/r_\mathrm{s})}{r/r_\mathrm{s}}, \tag{49}$$

where G is the gravitational constant. To solve the equation for hydrostatic equilibrium (Equation 5), we require the derivative of the potential, which is given by

$$\frac{\mathrm{d}\Phi}{\mathrm{d}r} = -16\pi G\rho_\mathrm{s} r_\mathrm{s} \left[\frac{\frac{r/r_\mathrm{s}}{(1+r/r_\mathrm{s})} - \ln(1+r/r_\mathrm{s})}{(r/r_\mathrm{s})^2}\right]. \tag{50}$$

Evaluating this derivative directly for $r/r_\mathrm{s} \to 0$ will cause the denominator to blow up and is therefore numerically unstable. We therefore take the Taylor approximation of Equation 50 (see Appendix A.3) and use this to evaluate the gradient for $r/r_\mathrm{s} < 0.005$.

We expressed the NFW density and potential using the scale radius r_s and density, but these can be written in terms of the virial mass M_vir, virial radius r_vir and concentration $c \equiv r_\mathrm{vir}/r_\mathrm{s}$. The scale density is then given by

$$\rho_\mathrm{s} = \frac{M_\mathrm{vir}}{16\pi r_\mathrm{s}^3[\ln(1+c_\mathrm{vir}) - c_\mathrm{vir}/(1+c_\mathrm{vir})]}. \tag{51}$$

For the Milky Way halo, we use the parameters as given by Bland-Hawthorn & Gerhard (2016)

$$M_\mathrm{vir} = 1.3\times 10^{12}\,\mathrm{M}_\odot, \quad r_\mathrm{vir} = 282\,\mathrm{kpc}, \quad c_\mathrm{vir} = 10 \tag{52}$$

where the virial mass also has been measured with Gaia to be around this value (Posti & Helmi, 2019). The corresponding scale radius and density can be seen in Table 1.

2.4.2 Density of the coronal gas

Gas in the corona is at a high temperature around the virial temperature of the halo, and is therefore observed in X-ray. For external galaxies and clusters, the X-ray surface brightness of gas in the halo is typically modeled using a β-model (Forman et al., 1985; O'Sullivan et al., 2003; Li et al., 2016; Zhang et al., 2024)

$$I_\mathrm{X}(R) \propto \left[1+\left(\frac{R}{r_c}\right)^2\right]^{-3\beta+1/2} \tag{53}$$

where R is the projected distance to the centre of the system, r_c is the core radius and β determines how steeply the model falls of at large R. Assuming that the emitting body of gas is spherically symmetric, the density is then given by

$$n(r) = n_0\left[1+\left(\frac{r}{r_\mathrm{c}}\right)^2\right]^{-3\beta/2}, \tag{54}$$

Table 1: Parameters for our two initial conditions of the Milky Way. The first three parameters are for the gas density described by the β model (Equation 54), and are motivated by Miller & Bregman (2016). The remaining parameters $r_\mathrm{s}, \rho_\mathrm{s}$ describe the NFW potential in which the corona is embedded. The entries with double quotes (″), indicate that the value of the parameter is identical to the other initial condition. The rescaled model contains roughly 3 times the mass compared to the `mb2016` model.

	β	r_c kpc	$n_{0,e}$ $10^{-2}\mathrm{cm}^{-3}$	$M_\mathrm{cor}(r_\mathrm{vir})$ $10^{10}\mathrm{M}_\odot$	Z $Z_\odot$	r_s kpc	ρ_s $10^{-26}\,\mathrm{g\,cm}^{-3}$
`mb2016`	0.49	2.12	0.447	1.74	0.3	28.2	5.2
`mb2016-rescaled`	″	″	1.490	5.80	0.1	″	″

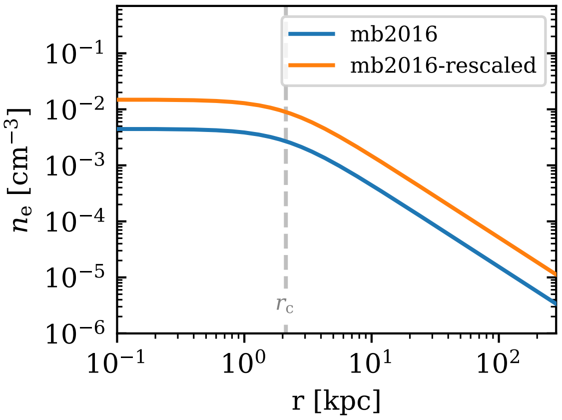

Figure 8: β-model (Equation 54) electron density profiles for the Milky Way corona, as observed by Miller & Bregman (2016) (`mb2016`, blue) and a rescaled variant (`mb2016-rescaled`, orange). The core radius r_c of the β-model is indicated by a vertical dashed line.

where n_0 is the density at the centre of the system. This β-model has a flat core with density n_0 up to r_c, and at larger radii decreases as a power law $n \propto r^{-3\beta}$.

Although observations of the Milky Way corona do not allow us to infer the radial profile from the X-ray surface, the gas density of the corona is still assumed to follow a β-model (Equation 54). Parameters for this model are then constrained with observations of [OVII] and [OVIII] absorption (Miller & Bregman, 2013), or emission (?Miller & Bregman, 2016; Locatelli et al., 2024). The core radius for Milky Way-like coronae, typically have $r_\mathrm{c} < 3\,\mathrm{kpc}$ (Miller & Bregman, 2013; Li & Bregman, 2017), which is much smaller than the extent of the Milky Way disc. This means that the region $r < r_\mathrm{c}$ can only be observed towards the GC, but this area is heavily obscured by the galactic disc and other sources like the Milky Way bubbles. Without the constraints for this region, the parameters n_0 and r_c are degenerate and can therefore not be fitted simultaneously. Alternatively, in the limit $r/r_c \gg 1$ Equation 54 can be approximated as

$$n(r \gg r_c) \approx n_0 r_\mathrm{c}^{3\beta} r^{-3\beta} \tag{55}$$

where the normalisation $n_0 r_\mathrm{c}^{3\beta}$ can then be constrained as a single parameter, removing the degeneracy (?Locatelli et al., 2024). Unfortunately, our model starts the integration of the corona from $r = 0$, so we cannot use this approximation.

Our first initial condition (we will refer to it as the `mb2016` corona) is given by Miller & Bregman (2016), where they simultaneously fit a multi component model to fit both the corona alongside the Fermi bubbles. For this they use emission lines from XMM-Newton and Suzaku, together with a normalization for the corona of $n_{0,\mathrm{e}} r_\mathrm{c}^{3\beta}$ obtained by **?**. For the corona, they then fix this normalization ($n_{0,\mathrm{e}} r_\mathrm{c}^{3\beta} = 0.0135\,\mathrm{cm}^{-3}\,\mathrm{kpc}^{3\beta}$) and only fit r_c and β, obtaining $\beta = 0.49 \pm 0.01$ and $r_\mathrm{c} = 2.12 \pm 0.22\,\mathrm{kpc}$. The central electron number density $n_{0,e}$ is then computed from the normalization, resulting in $n_0 = 4.47 \times 10^{-3}\,\mathrm{cm}^{-3}$.

Integrating this density profile gives a mass of $M_\mathrm{cor} \approx 1.74 \times 10^{10}\,\mathrm{M}_\odot$ at $r = r_\mathrm{vir}$ which is around $10\,\%$ of the *missing* baryons.[4] This is relatively low compared to significantly higher fractions obtained from stacking X-ray emission (Zhang et al., 2024) and stacking of the SZE (Bregman et al., 2022) around Milky Way-like galaxies. Additionally, Miller & Bregman (2016) assume a metallicity of $Z = 0.3 Z_\odot$, which is relatively high compared to more recent observations (Ponti et al., 2023), which are closer to $Z = 0.1 Z_\odot$, or even lower. A lower metallicity results in a lower oxygen abundance, so in order to explain the same X-ray brightness we would need a higher density. Unfortunately these more recent estimates (Locatelli et al., 2024) do not constrain the inner parameters (note that this does not affect the total mass much), so we cannot use them as an initial condition. To still investigate the evolution of such a lower metallicity and higher mass CGM, we use the same structural parameters (β, r_c) as the Miller & Bregman (2016) profile, but rescale the density such that the total mass at r_vir is around $30\,\%$ of the missing baryons. We refer to this second initial condition as the `mb2016-rescaled` corona. The parameters of these two initial conditions can be found in Table 1, and their electron density profiles can be seen in Figure 8.

2.4.3 Boundary conditions and entropy-mass relation

To integrate the corona, we want to find our boundary condition P_∞ for both the density profiles described in the previous section. To find this value, we assume the temperature of the gas at $R_\mathrm{out} = r_\mathrm{vir}$ to be equal to $T = 10^{6.3}\,\mathrm{K}$ (?Ponti et al., 2023; Locatelli et al., 2024). For a discussion of this assumption see Section 4.2.1. The resulting outer boundary condition on the pressure is then $P_\infty \equiv P(R_\mathrm{out}) = n(R_\mathrm{out}) k_\mathrm{B} T(R_\mathrm{out}) = 1.7 \times 10^{-14}\,\mathrm{erg\,cm}^{-3}$ for the `mb2016` corona, and $P_\infty = 5.7 \times 10^{-14}\,\mathrm{erg\,cm}^{-3}$ for `mb2016-rescaled`.

To compute the entropy-mass relation $\sigma(M)$ we first find $\sigma(r)$ and $M(r)$ for the initial conditions. We obtain the mass by numerically integrating Equation 2, directly since the density is known (Equation 54). We compute $\sigma(r)$ using Equation 3, for which we first need to find $P(r)$. Integrating Equation 1 from 0 to r gives

$$\int_{P(0)}^{P(r)} \mathrm{d}P = P(r) - P(0) = -\int_0^r \rho(r') \frac{\mathrm{d}\Phi}{\mathrm{d}r'} \mathrm{d}r' \equiv -I(r), \tag{56}$$

where, $P(0)$ is the pressure at $r = 0$ and for convenience, we define $I(r)$ to be the integral on the RHS up to some radius r. We can find $P(0)$ by evaluating the above equation at $r = R_\mathrm{out}$

$$P(0) = P_\infty - I(R_\mathrm{out}) \tag{57}$$

since $P(R_\mathrm{out}) = P_\infty$, and we can numerically integrate $I(r)$ for any r. Then, we use Equation 56 again to find $P(r) = P(0) - I(r)$. Finally, we combine the pressure and density to compute $\sigma(r)$.

The resulting pressure, mass and entropy profiles for both initial conditions can be seen in Figure 9. The pressure profile, as expected starts around a constant value $P(0)$ and decreases until P_∞. In the initial condition for σ, we see a small negative gradient around $1\,\mathrm{kpc}$, which we remove if our method of convection is enabled. The initial electron density can be seen in Figure 8, and the temperature can be seen in our results, Figure 13.

2.5 Solutions for cooling flows in the corona

We can compare the resulting profiles from our integration with self similar, steady-state solutions of cooling flows in galaxy-scale haloes by Stern2019. These solutions describe a possible scenario of how shocked gas from hot mode accretion reaches the galaxy via cooling flows. First, gas from

---

[4] We define the missing baryons as $M_\mathrm{b} - M_\mathrm{disc}$, where the expected baryonic mass M_b is obtained by multiplying the cosmic baryon fraction (ratio of baryonic to dark matter density) $f_\mathrm{b} = \Omega_b/\Omega_c \approx 0.187$ (Planck Collaboration et al., 2020), by the virial mass of the halo $M_\mathrm{b} = f_\mathrm{b} M_\mathrm{vir}$, and the total observed baryonic mass in the disc $M_\mathrm{disc} \approx M_\star + M_\mathrm{gas,disc}$, where we use $M_\star = 5 \times 10^{10}\,\mathrm{M}_\odot$ (Bland-Hawthorn & Gerhard, 2016) and $M_\mathrm{gas,disc} \approx 8 \times 10^9\,\mathrm{M}_\odot$ (Sparke & Gallagher III, 2007).

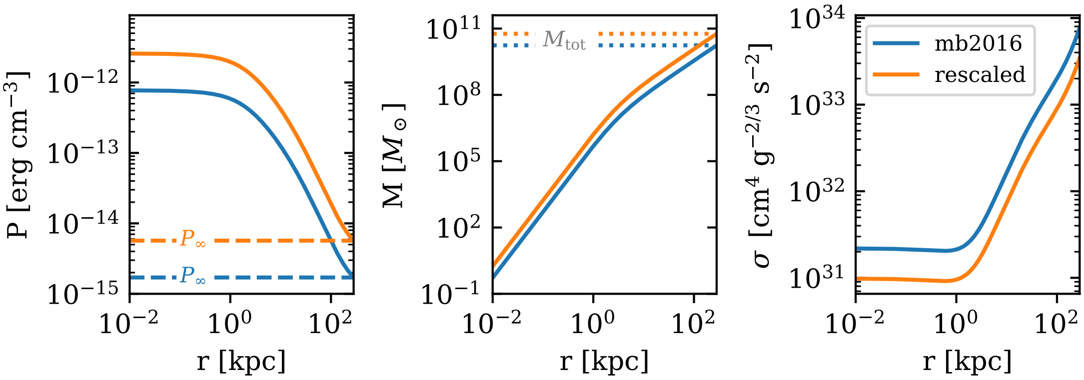

Figure 9: Integrated pressure (left), mass (middle) and entropy-index (right) profiles for our two initial conditions `mb2016` (blue) and `mb2016-rescaled` (orange). The obtained boundary conditions P_∞ and M_{tot} are indicated by dashed and dotted horizontal lines in their respective plots.

the IGM is accreted and shocked to the virial temperature by the halo at some outer radius R_{shock}. Subsequently, the gas cools radiatively and subsonically ($\mathcal{M} \ll 0$, where the mach number $\mathcal{M}$ is the ratio of the radial velocity over the adiabatic sound speed $\mathcal{M} \equiv |v_r|/c_{\mathrm{s}}$) flows through the halo towards the central galaxy. Finally, when the flow reaches the galaxy, at roughly the stellar half-mass radius $R_{1/2}$, angular momentum from the disc becomes important and the system will no longer be spherically symmetric. Close to the disc, feedback from the galaxy can also reheat the gas and influence the cooling flow. The solutions by Stern2019 describe this cooling flow in the halo, and are only valid for the region within the shock radius ($r < R_{\mathrm{shock}}$), and far away from the galaxy ($r > R_{1/2}$).

Stern2019 assume a spherically symmetric ideal fluid and no magnetic field, viscosity nor thermal conduction. Moreover, they assume the flow to be in steady-state and subsonic. The circular speed of the system v_{c} is related to the gravitational potential Φ of the system by $\Phi = -\int (v_{\mathrm{c}}^2/r)\mathrm{d}r$. They assume the potential to be dominated by the potential of the dark matter halo, and assume the circular speed can be written as a power law

$$v_{\mathrm{c}}(r) = v_{\mathrm{c}}(R_{\mathrm{vir}})\left(\frac{r}{R_{\mathrm{vir}}}\right)^m, \tag{58}$$

with m a constant, and R_{vir} the virial radius of the dark matter halo. For this power law, $m = 0$ describes an isothermal potential and $m = -0.5$ the potential of a point mass. Then, they assume all the logarithmic derivatives of the density, temperature and radial velocity with respect to r:

$$\frac{\mathrm{d}\ln\rho}{\mathrm{d}\ln r}, \quad \frac{\mathrm{d}\ln T}{\mathrm{d}\ln r}, \quad \frac{\mathrm{d}\ln v_r}{\mathrm{d}\ln r}, \tag{59}$$

to be constant, resulting in solutions which are self-similar, i.e. power laws in r. Finally, they assume the cooling rate of the gas Λ to be constant, making the final expressions easier to work with, at the cost of only minor inaccuracies. The self-similar steady-state solutions for the cooling flows then give $\rho(r), T(r), v_r(r)$ in terms of mass accretion $\dot{M}$, halo mass M_{vir}, cooling rate Λ and m (Equation 58), and they depend on radius as

$$\rho \propto r^{m-3/2}, \quad v_r \propto r^{-m-1/2}, \quad T \propto r^{2m}, \tag{60}$$

where quantities other than r only influence the proportionality constants. For the full solutions see Appendix A.5 and additionally for details of the derivation, comparison with numerical integration, simulations and application to other more massive haloes see Stern2019.

To compare the cooling flow solutions with our coronae, we choose values for M_{vir}, Λ and m to match our initial conditions. We take the virial mass to be the same as the Milky Way dark matter halo ($M_{\mathrm{vir}} = 1.3 \times 10^{12}\,\mathrm{M}_\odot$, see Equation 52). The cooling rate depends on the metallicity of the corona, which we assume to be either $0.3Z_\odot$ or $0.1Z_\odot$. For a metallicty of $0.3Z_\odot$, we adopt the same value as assumed by Stern2019 of $\Lambda = 0.6 \times 10^{-22}\,\mathrm{erg\,cm^3\,s^{-1}}$, roughly corresponding to the value of the cooling function at the flat part around $T = 8 \times 10^5$ K (see Figure 4). We similarly choose the value for $0.1Z_\odot$ to be $\Lambda = 0.25 \times 10^{-22}\,\mathrm{erg\,cm^3\,s^{-1}}$. We can find m by requiring that the slopes of the density of the cooling flow solutions $\rho \propto r^{m-3/2}$, equals the slope of the beta model in the large r limit $\rho(r) \propto r^{-3\beta}$ (Equation 55). Setting these equal, and solving for m gives us

$$m = 3/2 - 3\beta \tag{61}$$

which, with our initial conditions for the Milky Way ($\beta \approx 1/2$, Table 1) results in $m = 0$. We note that this value is different from the value of $m = -0.1$, which Stern2019 determines based on the circular velocity resulting from the combination of a central galaxy, a $10^{12}\,\mathrm{M_\odot}$ NFW halo and an outer component by Diemer & Kravtsov (2014). Since the difference in choice of m is small, it does not influence our results significantly. We leave the mass accretion $\dot{M}$ free in order to the compare accretion rates in the cooling flow solutions with our evolutionary model.

The full self-similar solutions for $m = 0$ are then given as (see Appendix A.5):

$$\rho(r) = 2.4 \times 10^{-5} \left(\frac{M_\mathrm{vir}}{10^{12}\,\mathrm{M_\odot}}\right)^{0.36} \left(\frac{\dot{M}}{\mathrm{M_\odot/yr}}\right)^{\frac{1}{2}} \left(\frac{\Lambda}{10^{-22}\,\mathrm{erg\,cm^3\,s^{-1}}}\right)^{-\frac{1}{2}} \left(\frac{r}{100\,\mathrm{kpc}}\right)^{-\frac{3}{2}} m_\mathrm{p}\,\mathrm{cm^{-3}} \tag{62}$$

$$|v_r(r)| = 12.9 \left(\frac{M_\mathrm{vir}}{10^{12}\,\mathrm{M_\odot}}\right)^{-0.36} \left(\frac{\dot{M}}{\mathrm{M_\odot/yr}}\right)^{\frac{1}{2}} \left(\frac{\Lambda}{10^{-22}\,\mathrm{erg\,cm^3\,s^{-1}}}\right)^{\frac{1}{2}} \left(\frac{r}{100\,\mathrm{kpc}}\right)^{-\frac{1}{2}} \mathrm{km\,s^{-1}} \tag{63}$$

$$T = 8 \times 10^5 \left(\frac{M_\mathrm{vir}}{10^{12}\,\mathrm{M_\odot}}\right)^{\frac{2}{3}} \mathrm{K} \tag{64}$$

3 Results

In this chapter we present the results of running the evolutionary model with both the `mb2016` and the `mb2016-rescaled` initial conditions for the Milky Way. Both initial conditions are density profiles described by beta models based on observations of the Milky Way corona from ?Miller & Bregman (2016). The `mb2016` profile is equal to the values of Miller & Bregman (2016) and has a metallicity of $Z = 0.3\,\mathrm{Z}_{\odot}$. The `mb2016-rescaled` initial condition has the same shape, but is rescaled to have three times the mass and a metallicity of $Z = 0.1 Z_{\odot}$, to be more in line with recent observations by eROSITA of the Milky Way corona (Ponti et al., 2023) and the corona of Milky Way-like galaxies (Zhang et al., 2024) (see Section 2.4 and Table 1).

Using both initial conditions, we also vary the cooling and heating processes as described in Section 2.2. We start by showing the results from the pure cooling case using the classical SD1993 cooling function (Section 3.1). This case is most analogous to the original application of the evolutionary model to the corona of the Hydra cluster by Kaiser & Binney (2003). We then continue with comparing the classical cooling case, with a more modern cooling function by `CLOUDY` (Ferland et al., 2013), where we also add photoionization from the extragalactic UVB by Haardt & Madau (2012) (Section 3.2). Finally, we add a powerful heating source in the centre of the system resembling the Fermi/eROSITA Bubbles (Miller & Bregman, 2016; Predehl et al., 2020). We then vary the power of this central source to investigate how the corona evolves under different heating sources (Section 3.3).

3.1 Classical cooling

In this section, we apply the evolutionary model from Kaiser & Binney (2003) to the corona of the Milky Way as observed by ?Miller & Bregman (2016) (`mb2016`) and a variant rescaled in mass (`mb2016-rescaled`) to represent more recent observations of the Milky Way and Milky Way like galaxies (Ponti et al., 2023; Zhang et al., 2024). In analogy with what is done in Kaiser & Binney (2003), we use a classical CIE cooling function from SD1993 (Section 2.2.1). The resulting evolutions of the two initial conditions can be seen in Figure 10. In this Figure we see the electron density n_{e} (first row), temperature T (second row) and entropy index σ (third row) profiles displayed at time intervals[5] of $0.5\,\mathrm{Myr}$ (blue to red). The left column displays these profiles for `mb2016`, and the right column for `mb2016-rescaled`.

For both initial conditions, we see that only the inner regions of the corona (less than a few kpc) evolve significantly, whereas the rest of the corona stays relatively constant. In the inner regions, as a result of cooling, the entropy index decreases (Equation 15), along with an increase in density and a decrease in temperature. For the SD1993 cooling function, $\mathbb{L} \propto n_{\mathrm{e}}^2$ (Equation 23), and also $\mathbb{L}$ increases rapidly from temperatures of 10^6 K to 10^5 K (see Figure 4), which means cooling experiences a runaway effect and will result in a cooling catastrophy. Since a higher cooling rate results in a lower cooling time (Equation 26), we have to lower the step-size of the evolution in order to avoid the entropy from becoming negative (see Equations 20 and 42). Because of the runaway effect, the step-size will only decrease further and essentially the corona will not evolve anymore with this model. We therefore stop the evolution when the step-size gets too low (see Section 2.3.4, and discussion in Section 4.2.4). For the `mb2016` case, the evolution stops at $\sim 10\,\mathrm{Myr}$, whereas the `mb2016-rescaled` corona stops at $\sim 5\,\mathrm{Myr}$. Both are significantly shorter than the expected age of the Milky Way corona of several Gyr (Cimatti et al., 2019). We emphasise, however, that all the above occurs essentially within a few kpc of the corona, which in reality is dominated by stellar components of the Milky Way. Our assumption of a spherical non-rotating system will no longer be valid in this location due to the presence of the Milky Way disc. Moreover, feedback from the galaxy will have an effect on the properties of the gas as well. We can therefore not draw any clear conclusions about the physical implications of the rapid cooling in the inner regions of our Milky Way corona.

---

[5] These time intervals are not to be confused with the step-size of the evolution δt.

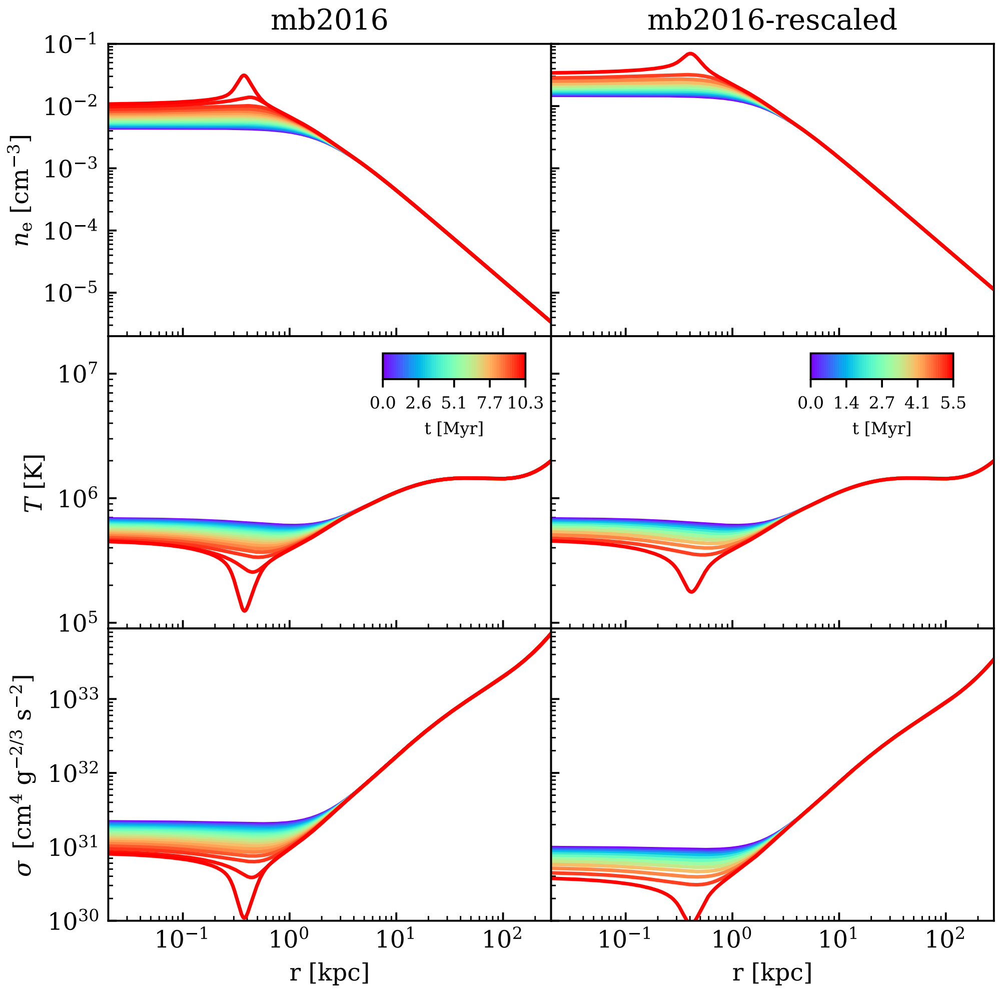

Figure 10: Full evolutions of the electron density, temperature and entropy-index of the `mb2016` (left column) and `mb2016-rescaled` (right column) initial conditions. Evolution uses the classical CIE cooling function from SD1993, described in Section 2.2.1. The colour of the line indicates the timestep of the evolution.

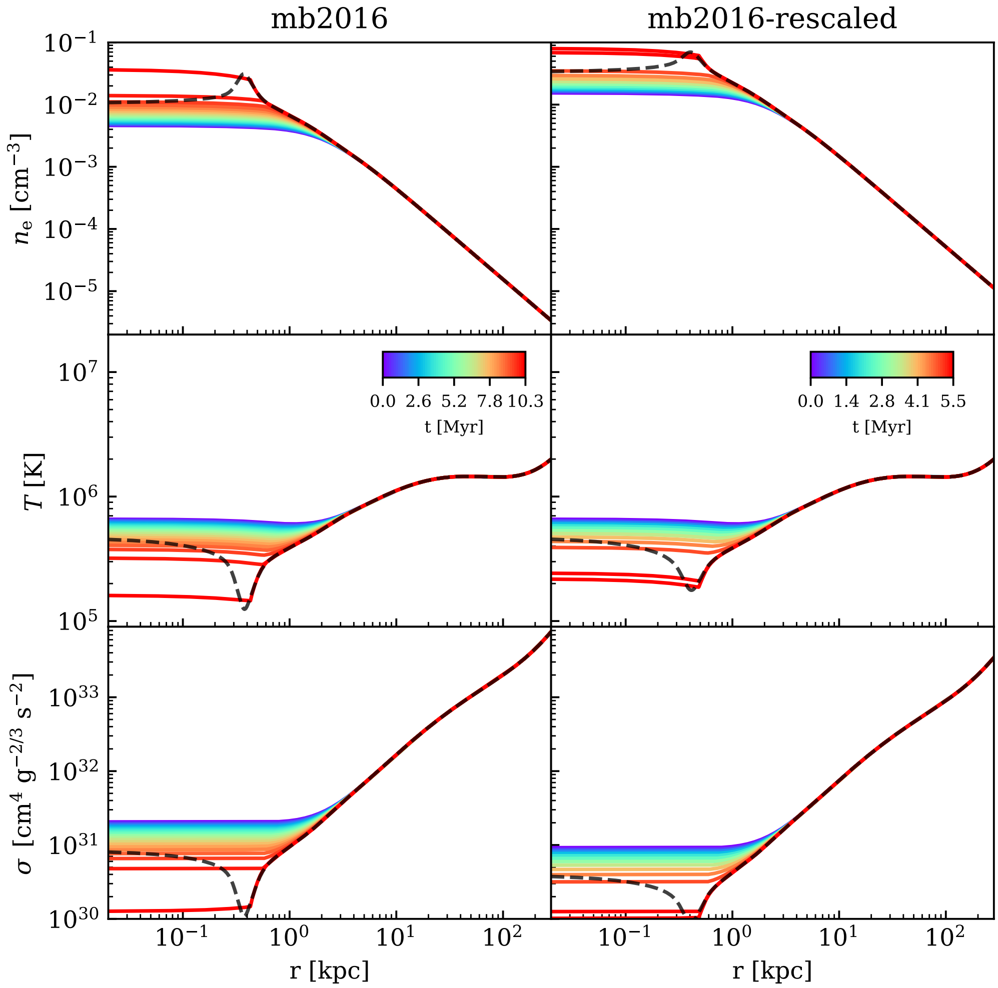

Figure 11: Same as Figure 10, but now the evolution also uses the method for convection (Section 2.2.4). The black dashed line is included as a reference to indicates final timestep of the method without convection (full Figure 10).

When Kaiser & Binney (2003) applied this model to the Hydra cluster, they observed a similar cooling catastrophy occuring in the centre of the cluster after $284\,\mathrm{Myr}$ of evolution. At that point, they also stop the evolution and assume the central AGN erupts and restores the density and temperature to the initially observed conditions. Drawing similar conclusions for the Milky Way would then suggest the black hole in the centre of the Milky Way would erupt within 5 to $10\,\mathrm{Myr}$. However, this ignores the presence of the Milky Way disc completely which most likely has significant impact on the inner regions of the corona. Probably, the gas in this region will either be accreted by the disc to feed star formation, or be reheated by feedback from the galaxy. In Section 3.3, we explore the second scenario of galaxy feedback, by adding a heating source in the centre of the system.

3.1.1 Inclusion of convection

In Figure 10, we see that the cooling occurs most rapidly just below $1\,\mathrm{kpc}$, around the location where the temperature is lowest in the initial conditions. This means, however that a negative entropy gradient forms and that the region is convectively unstable. Since the cooling is most rapid in this region, we can see if the rapid formation of a cooling catastrophy is partly caused by this convectively unstable zone. We therefore run the evolutionary models again with the same parameters, only now with our convection method enabled. Essentially, this method makes sure that at each timestep regions with negative entropy gradients are replaced by their mass-weighted average entropy over the same region, removing the negative gradient (see Section 2.2.4). The resulting density, temperature and entropy index for both initial conditions with convection enabled, can be seen in Figure 11, with the dashed black line representing the final profiles from the model without convection.

In this Figure, we can see that due to the convection method the entropy index is now completely flat in the inner regions of the corona, which means that the convectively unstable regions have been successfully removed. Compared to the final state of the model without convection (black dashed line), we see that the dip in entropy (but also bump in density and dip in temperature) is redistributed to the inner regions, resulting in a lower inner entropy index (and higher density, lower temperature) at $r = 0\,\mathrm{kpc}$. Beyond the region where convection is active, we see that the evolution of the model with convection is identical to the evolution of the model without convection. Also the evolution times remain identical, around the values of $\sim 10\,\mathrm{Myr}$ and $\sim 5\,\mathrm{Myr}$ for `mb2016` and `mb2016-rescaled` respectively.

The rapid cooling in the centre is therefore not a consequence of the negative entropy gradients, since the evolution times of the coronae are unaffected. However, because the convective method is able to remove the negative entropy gradients, whilst still evolving the outer parts of the corona identically to the method without convection, we will use it for the rest of our results.

3.1.2 Mass accretion

An important role of the corona in the context of galaxy evolution is its ability to feed the galaxy with gas to sustain the star formation. We therefore compute the mass accretion (see Section 2.3.5) across the entire evolution of the corona, which can be seen in Figure 12. Here we see the mass accretion profile for `mb2016` in the left, and the accretion profile for `mb2016-rescaled` in the right panel and the colour of the lines indicates the evolutionary time (from blue to red). For both coronae, across the entire evolution, we see that the mass accretion is very small in the centre, and increases with radius until it peaks and flattens out between 1 and $10\,\mathrm{kpc}$. From that point on, it stays roughly constant until it drops off a little bit at $r > 200\,\mathrm{kpc}$. Over time, the mass accretion increases mostly in the centre and stays relatively constant beyond $10\,\mathrm{kpc}$. In Figure 11 we saw that the density increased by almost an order of magnitude in the centre of the corona, whereas in the region beyond $10\,\mathrm{kpc}$ remained almost constant. It may therefore seem surprising to see that mass accretion is higher at $r > 10\,\mathrm{kpc}$, however this is explained by the fact that volume scales with radius as r^3 and therefore even a small change in density at high r, will have a large impact on the mass at such radii.

The increase in mass accretion as a function of radius below $\sim 1\,\mathrm{kpc}$ can also be explained by the r^3 scaling of volume. In the region below $1\,\mathrm{kpc}$, the density is approximately constant with radius due to the nature of the beta-model. As this region cools, the density increases at roughly the same rate in this region and as a consequence stays constant over r. Therefore, the mass profile scales with the volume and consequently the mass accretion profile also increases with r^3.

The peak in mass accretion between 1 and $10\,\mathrm{kpc}$ coincides with the region around the core radius of the beta-model, where the density as a function of radius starts to decrease. But also this region marks the transition from the centre where density increases due to rapid cooling, to the outer part of the corona, where the density stays constant over time. We see that at the start of the evolution (blue lines in Figure 12) no peak has developed yet, however, since density increases only in the centre of this region, $\dot{M}$ will increase faster around $1\,\mathrm{kpc}$ compared to $10\,\mathrm{kpc}$ which results in the formation of the peak in $\dot{M}(r)$.

At large radii, where the mass accretion is roughly constant, the difference between the two coronae is quite large. The corona of `mb2016`, shows a mass accretion of $\dot{M} \simeq 0.2\,\mathrm{M}_{\odot}/\mathrm{yr}$, whereas the accretion in `mb2016-rescaled` is much higher at $\dot{M} \simeq 1\,\mathrm{M}_{\odot}/\mathrm{yr}$. This difference can mostly be explained by the fact that the density in `mb2016-rescaled` is higher than in `mb2016`, therefore there is more cooling and consequently the mass accretion is higher. The lower metallicity of $Z = 0.1Z_{\odot}$, compared to $Z = 0.3Z_{\odot}$ for `mb2016`, should have the opposite effect and reduce the cooling in `mb2016-rescaled`. However, as we can see from the higher mass accretion and from

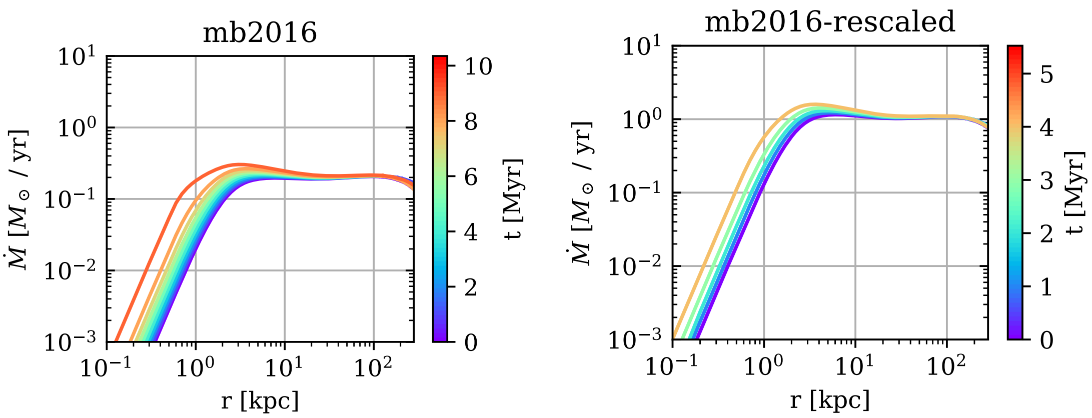

Figure 12: Evolution of the mass accretion profiles for the `mb2016` (left) and `mb2016-rescaled` (right) coronae, with classical cooling from SD1993 and convection enabled. The mass accretion rates are calculated based on average differences between the mass profiles $M(r)$ at different timesteps (see Section 2.3.5).

the shorter evolutionary time of the system, the increased density clearly has a stronger impact than the decreased metallicity.

? calculate the integrated mass accretion rate based on their observed density and estimated cooling time (t_{cool}) as

$$\dot{M}(r) = \int_0^r \frac{\rho(r')}{t_{\mathrm{cool}}(r')} 4\pi r'^2 dr\,'. \tag{65}$$

For a metallicity of $Z = 0.3Z_\odot$, they estimate the integrated mass accretion rate to be between 0.1 and $0.2\,\mathrm{M}_\odot/\mathrm{yr}$, at an outer radius where the cooling time equals the Hubble time (around $40\,\mathrm{kpc}$). The profile that matches the observed density from **?** is `mb2016`, so we can only compare the accretion rate of this profile. With a value of $\dot{M} \simeq 0.2\,\mathrm{M}_\odot/\mathrm{yr}$ at a radius of $40\,\mathrm{kpc}$, our mass accretion rate seems to match well.

The current SFR in the Milky Way is estimated to be around $1 - 3\,\mathrm{M}_\odot/\mathrm{yr}$ (Bland-Hawthorn & Gerhard, 2016). If we interpret our values for mass accretion to be equal to the amount of fresh gas that is fed to the galaxy in order to form new stars, we can see that with only radiative cooling the `mb2016-rescaled` corona is able to be a major contributor to sustain the star formation in the Milky Way. In practice, the amount of gas accretion needed to sustain the formation of stars in disc galaxies, is lower than the SFR (Fraternali & Tomassetti, 2012), so the accretion from `mb2016-rescaled` would then be sufficient. The gas accretion from the `mb2016` corona is much lower than the SFR, so if this corona is more representative for the Milky Way corona, additional sources of gas accretion are needed in order to fully sustain the formation of stars over a longer period of time. We note that our estimates here are in the absence of heating.

3.1.3 Comparison with steady-state cooling flow model

In the previous sections we have found that beyond a radius of a few kpc the profiles of density, temperature and entropy-index, stay relatively unchanged for the few $5 - 10\,\mathrm{Myr}$ that our model runs. Moreover, the mass accretion in these regions is relatively constant at $\dot{M} \simeq 0.2\mathrm{M}_\odot/\mathrm{yr}$ and $\dot{M} \simeq 1\mathrm{M}_\odot/\mathrm{yr}$ for `mb2016` and `mb2016-rescaled` respectively. We can compare the density, temperature and entropy-index profiles with the analytic model for steady-state cooling flows in Milky Way-like haloes by Stern2019 (see Section 2.5). In Figure 13, we can see the density, temperature and entropy index for both initial conditions (identical layout to Figures 10 and 11). Overplotted as dashed gray lines are the steady-state cooling flow models by Stern2019 for mass accretion rates of $\dot{M} = 0.1, 1.0$ and $10.0\,\mathrm{M}_\odot/\mathrm{yr}$ (see Equations 62 and 64). The slope of the lines in the cooling flow model is set to $m = 0$, to best match the density in our initial condition. The normalization of the cooling flow model is set by assuming $M_{\mathrm{vir}} = 1.3 \times 10^{12}\,\mathrm{M}_\odot$ and constant

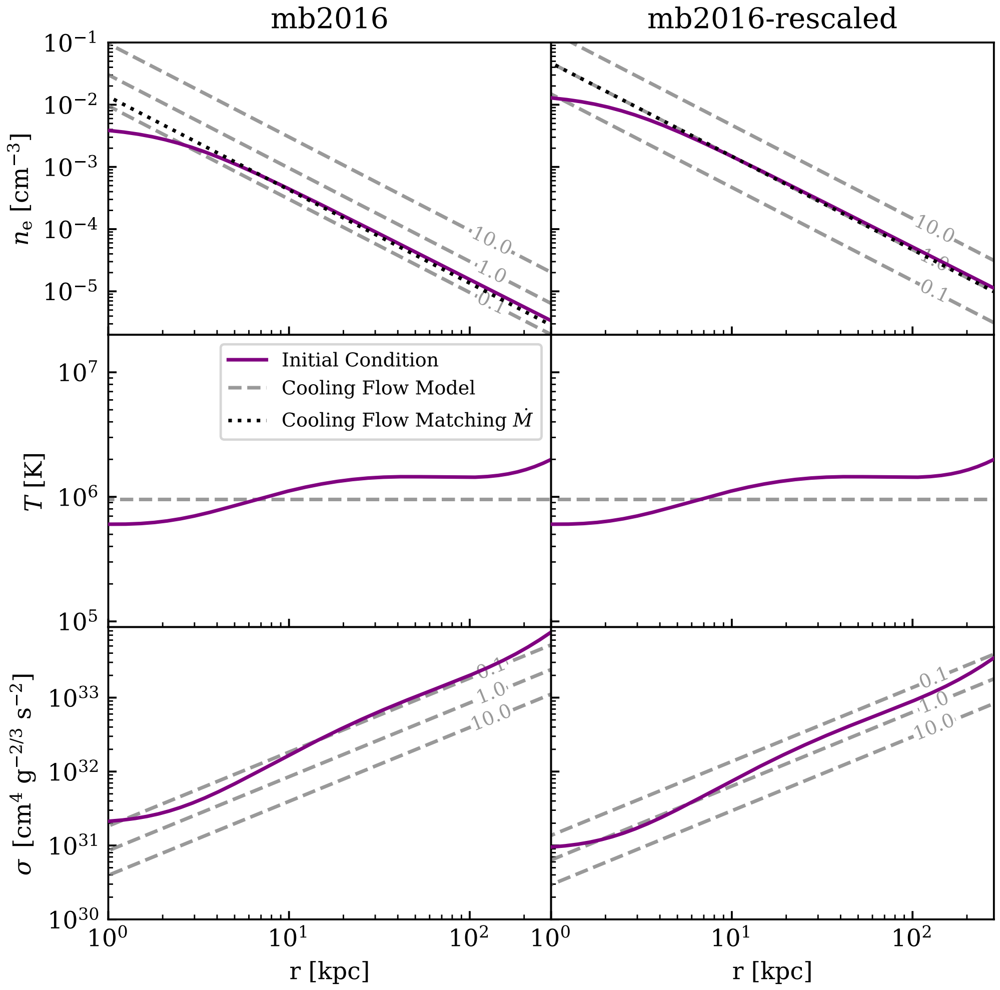

Figure 13: Comparison of our initial conditions in electron density, temperature and entropy-index for the `mb2016` (left column) and `mb2016-rescaled` (right column) corona as purple lines, with the same quantities predicted by the analytic steady-state solutions for cooling flows in a $m = 0$ Milky Way-like halo from Stern2019 (see Section 2.5) as gray and black lines. The grey gray dashed lines show the cooling flow solutions for mass accretion rates of $\dot{M} = 0.1, 1.0$ and $10.0\,\mathrm{M}_{\odot}/\mathrm{yr}$ (indicated in the figure). The black dotted line shows the cooling flow model with $\dot{M}$ based on the evolution of the corresponding corona (`mb2016`: $\dot{M} = 0.2\,\mathrm{M}_{\odot}/\mathrm{yr}$ and `mb2016-rescaled`: $\dot{M} = 1\,\mathrm{M}_{\odot}/\mathrm{yr}$).

cooling rates of $\Lambda = 0.6$ and $0.25 \times 10^{-22}\,\mathrm{erg\,cm^3\,s^{-1}}$ for the `mb2016` and `mb2016-rescaled` initial conditions, respectively. Finally, we also add black dotted curves for the cooling flow model having mass accretion rates equal to those found for our model in Section 3.1.2.

When we compare the density from the initial conditions, with the densities of the cooling flow model, we see that indeed the slopes of both models at large radii ($r > 10\,\mathrm{kpc}$) are identical. Of course, this is no coincidence as we have set $m = 0$ in the cooling flow model to match the density slopes. With the slopes identical, we can then compare the normalizations of the two models, which tells us something about the mass accretion since this is the only parameter that we vary in the cooling flow model. We see that for both `mb2016` and `mb2016-rescaled`, the density profiles match the cooling flow models with mass accretion rates of respectively $\dot{M} = 0.2$ and $1\,\mathrm{M_\odot/yr}$ (black dotted lines) remarkably well. The only difference is that the densities in the initial conditions are slightly higher than the matching cooling flow models, however a small difference can be expected, considering the mass accretion rates of our evolutionary model vary slightly over the entire evolition and the values that have been used to produce the matching cooling flow model have been estimated by eye.

We now look at the other quantities, starting from the temperature (middle row). Since $m = 0$ corresponds to an isothermal potential (Equation 58), the temperature profile of the cooling flow model does not depend on radius. For our initial conditions, the temperature clearly increases from $6 \times 10^5\,\mathrm{K}$ at $1\,\mathrm{kpc}$ to $2 \times 10^6\,\mathrm{K}$ at R_out, where this latter value is by construction. This change, however, is less than an order of magnitude and especially compared to other quantities like the density and entropy-index, the temperature is still relatively constant, and the temperature of the cooling flow model lies between our extreme values. Finally, in the bottom row of Figure 13, we compare the entropy-index from our model with the entropy-index from the cooling flow model. We see that again the slope and magnitude of the two models are very close. We estimate that the profile for `mb2016` is closest to the cooling flow model with $\dot{M} \approx 0.1\,\mathrm{M_\odot/yr}$ and `mb2016-rescaled` is between $\dot{M} \approx 0.1$ – $1.0\,\mathrm{M_\odot/yr}$. Both these values for the mass accretion are therefore lower than what we expect from our comparison of the density between the two models. This difference, however, is fully explained by the deviation in the temperature by using the definitions of σ and the cooling flow model solutions. Entropy index is defined as $\sigma \equiv P\rho^{-\gamma}$ and with the ideal gas law $P \propto \rho T$, we have $\sigma \propto T\rho^{-(\gamma-1)}$, meaning when T increases, σ increase proportionally as well. Moreover, in the cooling flow model, temperature does not depend on mass accretion (Equation 64), and density depends on $\dot{M}$ as $\rho \propto \sqrt{\dot{M}}$, together this gives $\sigma \propto \dot{M}^{-(\gamma+1)/2}$. Hence, a temperature which is higher compared to the cooling flow model, will also give a higher σ, and consequently a cooling flow model with a lower $\dot{M}$ will match this σ better.

In addition to the density and temperature, the cooling flow model also gives a solution for the radial velocity of the gas, as a function of radius $v_r(r)$ (Equation 63), where it is assumed that the gas flows towards the centre and therefore, by definition, $v_r(r) < 0$. The radial velocity for our evolutionary model can be computed via the continuity equation, using the mass accretion from our previous results (see Section 2.3.5, Equation 47). In Figure 14, we can see the resulting radial velocity profiles, where `mb2016` corona is displayed on the left, and `mb2016-rescaled` on the right. Similar to Figure 13, the radial velocities of the cooling flow model have been overplotted as gray dashed lines for mass accretion rates of $\dot{M} = 0.1, 1.0$ and $10.0\,\mathrm{M_\odot/yr}$. At small radii the radial velocity is between $1 - 10\,\mathrm{km\,s^{-1}}$ and increases with radius until it peaks around $1 - 2\,\mathrm{kpc}$ to a value of $20 - 100\,\mathrm{km\,s^{-1}}$. This increase and peak is similar to what we see in the mass accretion profile (Section 3.1.2), and is also a result of the constant density in this region. Beyond the peak, the velocity falls off again with a slope similar to the cooling flow model. In this region, the mass accretion rate was more or less constant, so the decrease here is caused by the $v_r(r) \propto \rho^{-1}r^{-2} \propto r^{-1/2}$ dependence at large r (Equations 47 and 55). Also similarly to the mass accretion, over time the radial velocity mainly accelerates in the centre of the corona and stays more or less constant beyond a few kpc. When we compare the radial velocity profiles with those of the cooling flow model, we again see that the `mb2016` and `mb2016-rescaled` coronae match the cooling flow models with $\dot{M} \simeq 0.2$ and $1\,\mathrm{M_\odot/yr}$, respectively. The radial velocity profile of our evolutionary model is computed using $\dot{M}(r)$ and $\rho(r)$, both which matched the cooling flow model well. It is therefore reassuring to see that the radial velocity also is a good match.

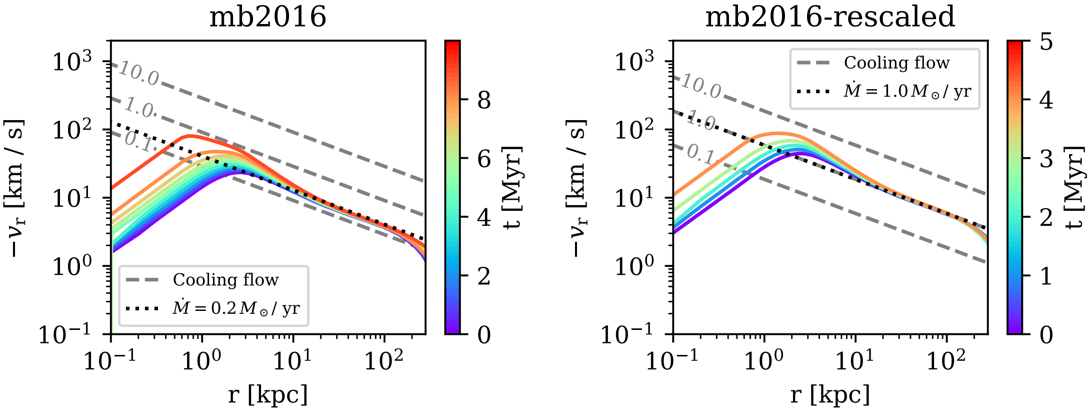

Figure 14: Evolution of the radial velocity profiles for the `mb2016` (left) and `mb2016-rescaled` (right) coronae, calculated from the mass accretion rate profile (see Section 2.3.5). Overplotted are the cooling flow models from Stern et al. (2019) as gray and black lines (similar to Figure 13).

We would like to emphasise again, that when we take the mass accretion rate as computed by our evolutionary model (Section 3.1.2) and use this value to compute the density distribution for the steady-state cooling flow model, this distribution is almost identical to our initial condition (beyond $10\,\mathrm{kpc}$). Such a similarity is not necessarily expected, because the assumptions used by the two models are very different. Our evolutionary model assumes that the corona is isolated with no in- or outflows from the IGM. Moreover, we assume that this corona is in hydrostatic equilibrium and evolve the corona numerically by radiative cooling using a CIE cooling function (SD1993). The mass accretion rate is then computed a posteriori from the evolution of the mass profile. The cooling flow model, instead, assumes a continuous steady-state cooling flow exists in the corona, and that this flow is continuously being fed by gas accretion from the IGM. The relation between the gas profiles (density, temperature, radial velocity) and properties of the halo (virial mass, mass accretion) is calculated analytically, assuming a constant cooling rate. The fact that these different assumptions produce similar results, implies that these assumptions might enforce each other. For instance, the steady-state cooling flow seems to produce a corona which is somewhat in hydrostatic equilibrium. And conversely, a corona in hydrostatic equilibrium with radiative cooling produces a constant cooling flow.

Finally, we note that our model is not in steady-state, and the comparison between our model and the cooling flow model is only valid for a short time ($5 - 10\,\mathrm{Myr}$). In Section 4.2.6 we evolve the corona for a longer ($t > 300\,\mathrm{Myr}$) time, and see that in this case the mass accretion rates in the outer region stay constant over this period as well. Therefore, the two models are likely still similar over such time-scales as well.

3.2 CLOUDY with extragalactic UVB

In the previous section, we have seen that our evolutionary model with only radiative cooling calculated with a classical cooling function from SD1993 produced coronae that cool in the centre within $10\,\mathrm{Myr}$. However, our main interest is in the outer regions of the corona, where non-spherical geometry and effects of the Milky Way disc do not affect our model, and it should be closer to reality. This part of the corona in the Milky Way is expected to be stable for a much longer time than $10\,\mathrm{Myr}$ (Cimatti et al., 2019), so we want our evolution to take longer as well. Our first step is to adjust the cooling prescription from the classical CIE cooling function (Section 2.2.1), to the usage of `CLOUDY` (Ferland et al., 2013) in order to be more in line with other recent determinations. In addition, we also add heating by photoionising radiation from the extragalactic UVB at $z = 0$ (Haardt & Madau, 2012). We note that only considering heating from the UVB is very much a lower limit to the more realistic case of the Milky Way, where additional heating is also likely to

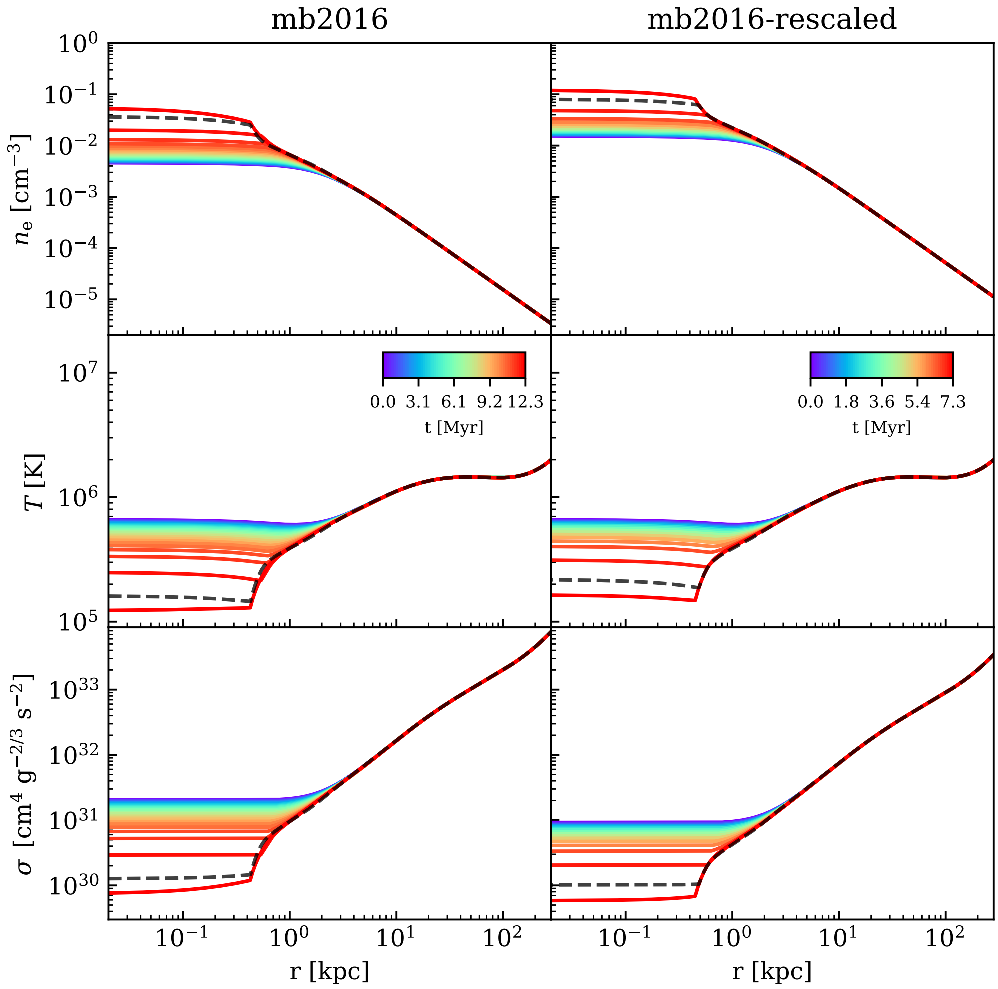

Figure 15: Same as Figure 10, but with cooling and heating from `CLOUDY` with photoionization from the extragalactic UVB, and with convection enabled. The black dashed line shows the final timestep of the evolution with classical cooling (see Figure 11).

occur via black hole and stellar feedback. For more details see Section 2.2.2.

We evolve the two initial conditions (`mb2016` and `mb2016-rescaled`) using the prescription outlined above and with our convection method enabled to avoid the formation of negative entropy gradients. The resulting evolutions of density, temperature and entropy index can be seen in Figure 15, where the layout is similar to Figures from the previous section. The final timestep of the evolution with classical cooling (Figure 11) is displayed as a black dashed line to compare with the results obtained with the `CLOUDY` prescription. In the Figure, we can see that the evolution with `CLOUDY` proceeds much like the evolution with classical cooling, where the inner regions of the corona, with highest initial density, cool rapidly and consequently dominate the evolution of the entire system. Also in this case, the outer regions of the corona seem to remain virtually constant. The difference compared to the evolutions with the classical cooling is that the evolution time is slightly longer, and the final density is slightly higher. Both can be explained by looking at the difference in the cooling function.

The evolution time of the system, roughly $12\,\mathrm{Myr}$ for `mb2016` and $7\,\mathrm{Myr}$ for `mb2016-rescaled`, are slighly longer than the respective 10 and $5\,\mathrm{Myr}$ with the classical cooling. This longer evolution time for both systems can be explained by the difference in the radiative energy loss $\Lambda - \Gamma$ between SD1993 and `CLOUDY` for temperatures $2 \times 10^4\,\mathrm{K} \leq T \leq 7 \times 10^5\,\mathrm{K}$ (black dotted and dashed lines, compared to blue line in Figure 4). In this domain, the radiative energy loss from `CLOUDY` is significantly lower than the CIE cooling function, and as a result of this lower cooling, the corona needs to evolve for longer to reach the same density as the classical cooling case. Even though the `CLOUDY` prescription includes heating from the extragalactic background, whereas the classical cooling case does not include any heating at all, the difference between the two prescriptions is mainly caused by the different calculation of the cooling rate Λ, and not the additional heating Γ, which turns out to have almost no impact in this evolution (see Section 4.2.5).

The final difference between the evolution with `CLOUDY` compared to the classical cooling, is the density in the final timestep of the evolution. The density of the `CLOUDY` evolutions is slightly higher than the final density from the classical cooling case, but this difference can also be explained by the different cooling rates. The cooling time depends on density and cooling rate roughly as $t_{\mathrm{cool}} \propto 1/(n\Lambda)$ (Equation 26). Since we use this cooling time as an upper limit to the timestep in the evolution ($\delta t \leq t_{\mathrm{cool}}/10$, Equation 42), and the evolution stops whenever a lower limit on the timestep is reached δt_{stop}, we can express this lower limit as a function of density and cooling rate. We do this by assuming that when the limiting timestep is reached, it is set by the upper limit defined by the cooling time

$$\delta t_{\mathrm{stop}} = t_{\mathrm{cool}}/10 \qquad \Longrightarrow \qquad \delta t_{\mathrm{stop}} \propto \frac{1}{n\Lambda}. \tag{66}$$

Since we have seen that the cooling rate Λ is lower for `CLOUDY`, a higher density is needed to reach the same δt_{stop}. Again, heating is not very relevant in this regime, because the density is high $\sim 0.1\,\mathrm{cm}^{-3}$. Since we set δt_{stop} to an arbitrary value, this difference in density at the final timestep is purely a numerical effect.

Whilst there are slight differences in the inner parts of the corona, the region beyond a few kpc from the centre seems to be unaffected by our change of the entropy update prescription, but we will look at the slight differences in mass accretion in the next Subsection. Unfortunately, our aim of extending the evolutionary time of the system by using `CLOUDY` only resulted in an evolution of a few extra Myr. We therefore conclude that heating from the extragalactic UVB is not sufficient to stop the corona from rapidly cooling in the centre. In the next Section (3.3), we will explore additional heating sources with the similar aim to extend the evolution of the system. Even though the prescription using `CLOUDY` did not have significant differences with the classical cooling case, it should be more realistic, so therefore we will use it when exploring other heating sources.

3.2.1 Mass accretion

Our results from the evolution of the corona using a classical cooling prescription, showed that for radii beyond $10\,\mathrm{kpc}$, the mass accretion of the `mb2016` and `mb2016-rescaled` coronae were

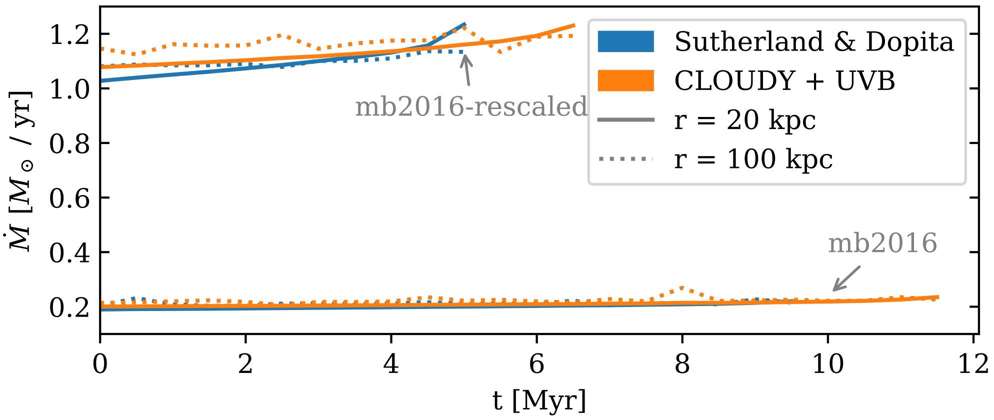

Figure 16: Comparison of mass accretion rates as a function of time from the classical cooling from SD1993 (blue) and `CLOUDY` with photoionisation (orange), taken at radii of 20 and 100 kpc (full and dotted lines). The mass accretion rates for the `mb2016` and `mb2016-rescaled` are shown in the same Figure, and indicated by arrows.

approximately constant with radius and time, with respective values of 0.2 and $1\,\mathrm{M_\odot/yr}$. For the evolution with `CLOUDY`, we can also compute the mass accretion profile (Section 2.3.5) and investigate how they compare to our previous results. As we have seen in Figure 15, the evolution in the outer region in density is essentially identical to the classical cooling case, and it turns out that the mass accretion profile calculated from the evolution with `CLOUDY`, is also virtually identical to Figure 12, so we do not show them here. Figure 16 shows instead the mass accretion at $r = 20\,\mathrm{kpc}$ (full lines) and $r = 100\,\mathrm{kpc}$ (dotted lines), for both the `CLOUDY` (orange lines) and classical cooling (blue lines) evolution. The values for `mb2016` and `mb2016-rescaled` have both been included in the same figure, and are indicated by arrows. Since the mass accretion profiles from the `CLOUDY` and classical cooling evolution are very similar to each other, the values of $\dot{M}$ at these two radii are very close to each other as well. In the Figure, we see that for both cooling/heating prescriptions, at both radii $\dot{M}$ increases slightly over time, where this effect is most pronouced for `mb2016-rescaled`, increasing from $\dot{M} \sim 1.1\,\mathrm{M_\odot/yr}$ to $1.2\,\mathrm{M_\odot/yr}$. At both radii, we also see that the mass accretion from the `CLOUDY` evolution is slightly higher than the classical cooling case, which is surprising since in the previous section we have seen that the radiative energy loss in `CLOUDY` in general was lower than in SD1993. The temperature at these radii, however, is roughly $10^6\,\mathrm{K}$ which is higher compared to the temperature in the inner regions of the corona. In Figure 4, we can see that at this temperature, for the density of the corona at these radii ($n_e \sim 10^{-5}\,\mathrm{cm^{-3}}$) the effective cooling rate of `CLOUDY` is actually higher than the cooling rate from SD1993, which explains why the mass accretion is slightly higher as well.

3.3 Heating from a central source

In the previous two sections, our results have shown that in isolation, the centre of a corona, similar to the corona of the Milky Way, will cool within $5 - 10\,\mathrm{Myr}$. Changing the cooling prescription and adding photoionizing radiation from the extragalactic UVB only delays the cooling in the centre by $2\,\mathrm{Myr}$, which is not long enough if we want to evolve for a time-scale comparable to a cooling time of $t_{\mathrm{cool}} \gg 100\,\mathrm{Myr}$ an isothermal Milky Way corona (Binney et al., 2009). In order to avoid the corona from rapidly cooling in the centre, we need additional heating, and the next obvious choice is heating from some central source in the Milky Way disc. This source can be interpreted as a galactic wind powered by supernovae, or the central black hole, which then could also be the source that created the Milky Way bubbles (Su et al., 2010; Predehl et al., 2020).

The heating from the centre of the system is included in the model by choosing a fixed power representing the total thermal energy injected into the system per unit time, $\dot{E}_{\mathrm{tot}}$. We then inject this energy at each timestep, weighted by a Gaussian kernel centered at the origin and with scale length λ (for details, see Section 2.2.3). We evolve the corona multiple times with varying $\dot{E}_{\text{tot}}$

$$\dot{E}_{\text{tot}} = 10^{39},\, 5\times10^{39},\, 10^{40},\, \dots,\, 5\times10^{42},\, 10^{43}\,\mathrm{erg\,s^{-1}}, \tag{67}$$

to see what power scales are needed in order to stop the centre from cooling. We evolve the corona with both initial conditions, using the `CLOUDY` prescription for updating entropy, combined with the additional heating from the centre. For high powers, the entropy in the centre will increase much faster than at larger radii, so to avoid negative entropy gradients we also include our prescription for convection. We choose the length scale of the kernel to match the size of the Fermi Bubbles with $\lambda = 8\,\mathrm{kpc}$ (height of $9\,\mathrm{kpc}$ Predehl et al., 2020). However, since the shape of the kernel is spherical, whereas the bubbles are better described by a cylinder, we also run evolutions with length scale $\lambda = 5\,\mathrm{kpc}$ roughly to match the volume of the Fermi Bubbles. Choosing a scale length which matches the volume of the eROSITA bubbles instead, would also roughly result in $\lambda = 8\,\mathrm{kpc}$.[6]

The evolution of the corona heavily depends on the value of $\dot{E}_{\text{tot}}$, but in general evolves in either of two cases, both which can be seen in Figure 17. In this figure we see the density, temperature and entropy-index over the evolution of the system for `mb2016`, with $\lambda = 8\,\mathrm{kpc}$. The left column shows the evolution with a relatively low power ($\dot{E}_{\text{tot}} = 10^{40}\,\mathrm{erg\,s^{-1}}$) and the right column shows the evolution with a high power ($\dot{E}_{\text{tot}} = 10^{42}\,\mathrm{erg\,s^{-1}}$), where on both sides the dashed black line represents the final timestep of the same corona without a central heating source (Figure 15). Our first case is represented in the left column, where $\dot{E}_{\text{tot}}$ is low, resulting in heating being subdominant to cooling. We can see in this case, that the evolutionary time of the system ($12\,\mathrm{Myr}$), and the density, temperature and entropy-index profiles in the final timestep almost exactly match the final timestep of the corona with no heating (black dashed line). The result in this case is therefore that the evolution proceeds almost identically as if there was no heating at all.

The second case, however, shows what happens to a corona under extreme heating with $\dot{E}_{\text{tot}} = 10^{42}\,\mathrm{erg\,s^{-1}}$. In this case, the heating becomes dominant over the cooling in the centre, resulting in a big decrease in density and increase in temperature. We see that in the first $30\,\mathrm{Myr}$ the density decreases by more than an order of magnitude from $4\times10^{-3}\,\mathrm{cm^{-3}}$ to $10^{-4}\,\mathrm{cm^{-3}}$, and the temperature jumps from 7×10^{5} K to 3×10^{6} K. From that point on, the density keeps decreasing and temperature keeps increasing, but it does so at a much slower pace. At the end of the evolution, the corona has an inner density of $2\times10^{-5}\,\mathrm{cm^{-3}}$ and a temperature of 4×10^{6} K.

The evolution in entropy-index is heavily influenced by our prescription of convection, which can be seen in the fact that the entropy-index is constant for a large part of the corona. This is caused by the fact that heating from the centre causes the entropy to go up only in the centre, and therefore a negative entropy gradient will form. Our convective method removes these negative gradient by replacing the unstable region with the average value of the entropy-index, resulting in these large isentropic profiles. At the start of the evolution, the corona still has a positive gradient starting from roughly $2\,\mathrm{kpc}$. However, after a few tens of Myr, the isentropic region has developed up to tens of kpc and reaches up to $200\,\mathrm{kpc}$ at the end of the evolution.

The evolutionary time in this extreme heating case is much longer ($180\,\mathrm{Myr}$) than in the dominant cooling case (about $10\,\mathrm{Myr}$), but interpreting this in a physical context is not possible due our choice in stopping condition based on the size of the timestep. We stop the evoltion whenever the timestep reaches a lower limit, which is set by the minimal value of the entropy update time-scale $|t_\epsilon|$, or whenever a maximum number of iterations is reached (Section 2.3.3). When cooling is dominant, t_ϵ decreases rapidly due to the runaway nature of cooling, which causes the timestep to also drop rapidly, and therefore the lower limit on δt is always reached before $N_{\text{iter,max}}$. Moreover, the evolutionary time does not increase, even if we would use a lower limit on δt. However, when heating is dominant ($\Lambda - \Gamma < 0$), the density and temperature in the corona increases, and in turn the cooling rate Λ decreases. Since the heating is approximately constant, the effective cooling rate $\Lambda - \Gamma$ becomes more negative, so heating is also a runaway effect. Compared to

---

[6] To estimate the volume, we assume the shape of one Fermi Bubble to be a cylinder with radius of the base $3\,\mathrm{kpc}$ and height $9\,\mathrm{kpc}$ and then multiply by 2 to account for the both bubbles above and below the Milky Way disc. The volume of eROSITA is similarly calculated, but with a radius of $7\,\mathrm{kpc}$ and a height of $14\,\mathrm{kpc}$. Values for the dimensions are taken from Predehl et al. (2020).

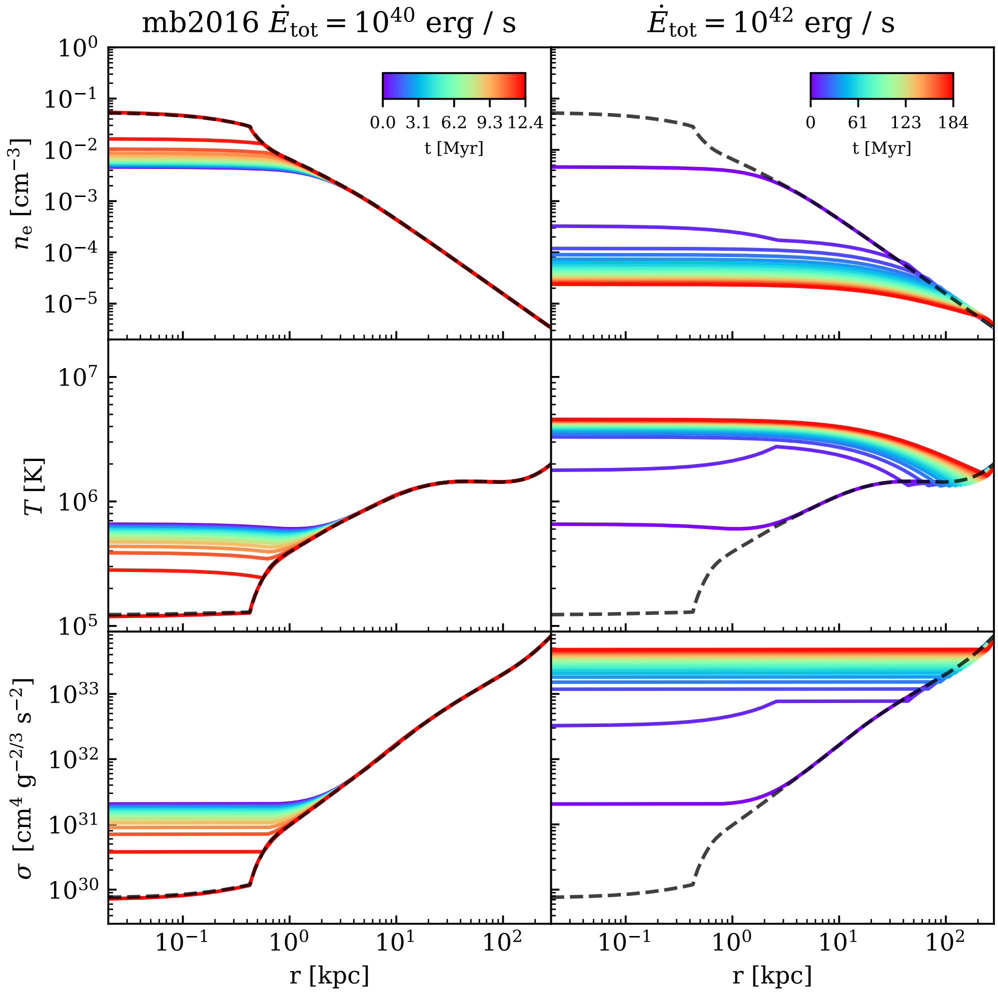

Figure 17: Evolution of two extreme cases heating, with a low power (left) and high power (right). Both evolutions have initial condition `mb2016`, convection enabled and length scale for heating $\lambda = 8\,\mathrm{kpc}$. The black dashed line shows the last timestep of the evolution without heating, which is fully shown in Figure 15. The time-steps between the curves are $1\,\mathrm{Myr}$ and $10\,\mathrm{Myr}$ for the left and right columns respectively.

cooling, however, the process is more gradual. The timestep will still decrease, but because it decreases more slowly, in some cases the maximum number of iterations is also reached. The choice of these stopping conditions therefore will influence the total evolution time in the system, and it is therefore not possible to put the evolutionary time in the extreme heating case in a physical context. For the coronae that are heating, the evolution time is mostly between $100 - 400\,\mathrm{Myr}$, but in principle they could evolve for much longer. For a detailed explanation see the discussion in Section 4.2.4.

Observations of properties of the Fermi Bubbles, have estimated a gas density of $n_{\mathrm{FB}} \sim 8 \times 10^{-4}\,\mathrm{cm}^{-3}$ and the temperature of $T_{\mathrm{FB}} \sim 4 \times 10^{6}\,\mathrm{K}$ in the bubble (Miller & Bregman, 2016). As we can see from Figure 17, these values for the density and temperature are achieved rather quickly in about $10 - 20\,\mathrm{Myr}$. Showing that the case where heating is dominant to the cooling is able to reproduce an environment similar to the Fermi Bubbles. The scale of the bubbles that we produce, however, reaches to at least $70\,\mathrm{kpc}$, which is one order of magnitude larger than the observed scale of the Milky Way bubbles.

The results above focus on the evolution from the `mb2016` initial condition, and power source with length scale $\lambda = 8\,\mathrm{kpc}$, however everything except the exact quantities and time-scales also applies for the `mb2016-rescaled` initial condition and for $\lambda = 5\,\mathrm{kpc}$. For our results, the main difference between these parameters is the value of the power needed for heating to be dominant, which we will discuss in the next subsection.

3.3.1 Heating threshold

We have seen that with a constant central heating source, the corona will be in either a regime with runaway cooling or one with runaway heating. Since these regimes are a function of the central power $\dot{E}_{\mathrm{tot}}$, there must be some threshold power where the corona transitions from being dominated by cooling to where heating is dominant. Since we have seen that the central density increases in the case of cooling, and decreases in the case of heating, we can use this to find upper and lower bounds for the threshold power. Figure 18 shows the electron density at $r = 0$ at the end of the evolution, as a function of the power of the central heating source with $\lambda = 8\,\mathrm{kpc}$ (upper panel) and $\sigma = 5\,\mathrm{kpc}$ (lower panel). The blue and orange colours show the values for `mb2016` and `mb2016-rescaled` respectively, where the large dots indicate the datapoints and the dotted lines connecting them are only visual. For reference, the initial values of $n_{\mathrm{e}}(r = 0)$ have been included as dashed lines.

In both Figures, we see that for energies below $\dot{E}_{\mathrm{tot}} \leq 5 \times 10^{40}\,\mathrm{erg\,s^{-1}}$ the final inner electron densities are all constant around a value of $n_{\mathrm{e}} = 0.1\,\mathrm{cm}^{-3}$, which is indeed similar to what we see in the left column of Figure 17, where cooling is dominant. As we have seen from the evolution without central heating, the density with `mb2016-rescaled` is higher at the end of the evolution, which we also see here. Since heating does not have an impact in this regime, the scale length of the kernel does not matter and the density values at the end of the evolution for $\lambda = 8$ and $5\,\mathrm{kpc}$ are the identical.

As the power of the central source increases, we see that for all the coronae, the density suddenly drops to an extremely low value around $10^{-4}\,\mathrm{cm}^{-3}$. This density is identical to the heating dominant case, shown in the right column of Figure 17. This sharp decrease in density for increasing $\dot{E}_{\mathrm{tot}}$ therefore denotes the region where the corona transitions from being cooling dominated to being heating dominanted and the threshold power should be somewhere in this region. The reason why the densities are constant for any power below or above the threshold are because the stopping condition is determined by the density and vice-versa. This can be seen if we adjust Equation 66 to also include heating:

$$\delta t_{\mathrm{stop}} \propto \frac{1}{n|\Lambda - \Gamma|}. \tag{68}$$

Reading off the values above and below the threshold from Figure 18, the upper and lower

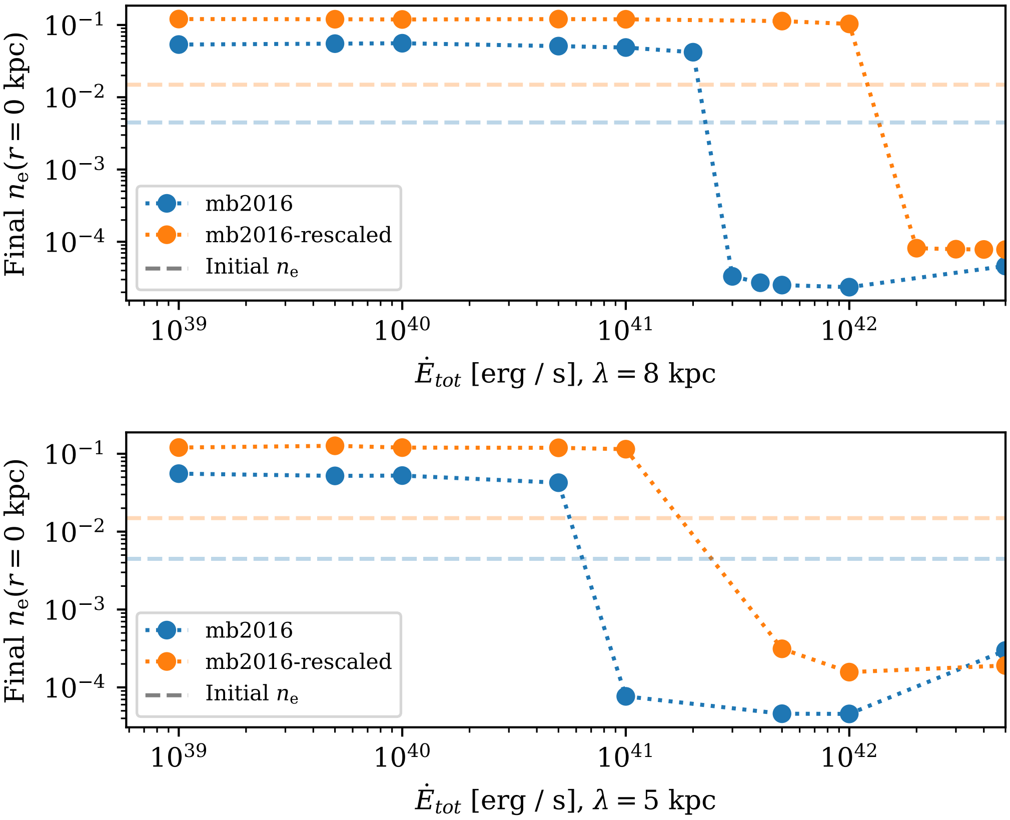

Figure 18: Inner ($r = 0$) electron densities at the end of the evolution of `mb2016` (blue) and `mb2016-rescaled` (orange) coronae, as a function of the power of the heating source in the centre of the system $\dot{E}_{\text{tot}}$ (scale length $\lambda = 8\,\text{kpc}$ above, $\lambda = 5\,\text{kpc}$ below). The dotted lines connecting the dots are a visual aid. As a reference, the initial densities at $r = 0$ are included as dashed lines.

bounds for the threshold power are:

$$\begin{aligned}
\text{for } \texttt{mb2016}\text{, with } \lambda = 8\,\mathrm{kpc} \text{ between } \dot{E}_{\mathrm{tot}} &= (2-3)\times 10^{41}\,\mathrm{erg\,s^{-1}},\\
\text{for } \texttt{mb2016-rescaled}\text{, with } \lambda = 8\,\mathrm{kpc} \text{ between } \dot{E}_{\mathrm{tot}} &= (10-20)\times 10^{41}\,\mathrm{erg\,s^{-1}},\\
\text{for } \texttt{mb2016}\text{, with } \lambda = 5\,\mathrm{kpc} \text{ between } \dot{E}_{\mathrm{tot}} &= (0.5-1)\times 10^{41}\,\mathrm{erg\,s^{-1}},\\
\text{for } \texttt{mb2016-rescaled}\text{, with } \lambda = 5\,\mathrm{kpc} \text{ between } \dot{E}_{\mathrm{tot}} &= (1-5)\times 10^{41}\,\mathrm{erg\,s^{-1}}.
\end{aligned}$$

Note that we have evolved the coronae with $\lambda = 8\,\mathrm{kpc}$ additional times around the threshold region, in order to see if we would be able to find a power for which the corona was not cooling nor heating dominated. However, we were unsuccessful in this regard, as can be seen in Figure 18, where on both sides of the threshold the density tends to one of the two extreme cases.

For powers above the transition region, we see that the inner density remains constant to around 10^{-4} – $10^{-5}\,\mathrm{cm^{-3}}$, which is due to the lower limit on the timestep, but increases again slightly for the `mb2016` corona at $\dot{E}_{\mathrm{tot}} \sim 5\times 10^{42}\,\mathrm{erg\,s^{-1}}$. This is also a numerical effect, however, since the magnitude of the heating is so large, that the shooting method has issues with finding a good $P(0)$ to get $P(R_{\mathrm{out}}) = P_\infty$ whilst keeping $M(R_{\mathrm{out}}) = M_{\mathrm{tot}}$, at some R_{out} and therefore stops the evolution prematurely. It would be possible to tweak the integration further in order to solve these issues, however, since the power at which this occurs is significantly above the transition region, we are not interested in the exact evolution of the corona with this power and we choose not to pursue it further.

In Figure 19 we show an example of the evolution with power just below (left column) and above (right column) the threshold region for the `mb2016` initial condition with $\lambda = 8\,\mathrm{kpc}$.[7] In the left panels of the Figure, we see that the density increases (temperature decreases) in the centre up to $1\,\mathrm{kpc}$. Between $1-20\,\mathrm{kpc}$ the density decreases (temperature increases), and beyond $20\,\mathrm{kpc}$ the profiles stay relatively unchanged. By calculating $\mathbb{L}$ in the outer parts of the corona, we find that it is also cooling here ($\mathbb{L} > 0$). This indicates that in the centre the corona is cooling, in the intermediate region it is heating, and beyond it is cooling again. This might be an indication that the scale length of the kernel is too large or that the Gaussian shape of the kernel produces tails which are too big. This same pattern is also present for coronae `mb2016-rescaled` with $\lambda = 8\,\mathrm{kpc}$ and `mb2016` with $\lambda = 5\,\mathrm{kpc}$, but not for `mb2016-rescaled` with $\lambda = 5\,\mathrm{kpc}$. Decreasing the length scale therefore does not immediately make the corona uniformly cooling or heating. Since these coronae are still dominated by cooling in the centre, and have therefore short evolution times, we still use them as the lower bound on the transition region.

We see that the threshold for the `mb2016-rescaled` corona is always at a higher power compared to the `mb2016` corona with the same length scale. This difference is due to the higher cooling in the `mb2016-rescaled` corona (for example see Section 3.1). More cooling means a higher energy loss, and consequently more heating is needed to counterbalance this cooling.

We also see that the threshold changes significantly if we change the size of the kernel. A smaller kernel size always produces a lower threshold, which again implies that the size, and perhaps the shape of the kernel, is important. In our implementation, if we decrease the length scale of the kernel whilst keeping the total power the same, the kernel will be more concentrated and insert more energy in the centre. Therefore, to balance the cooling in the centre, we need less total power, which should result in a lower threshold power. Since the kernel size seems to have impact on the results, it may be useful to investigate more sizes in future work.

---

[7] Appendix C contains Figures 31 to 33 similar to Figure 19 but for the `mb2016-rescaled` corona, and with $\lambda = 5\,\mathrm{kpc}$.

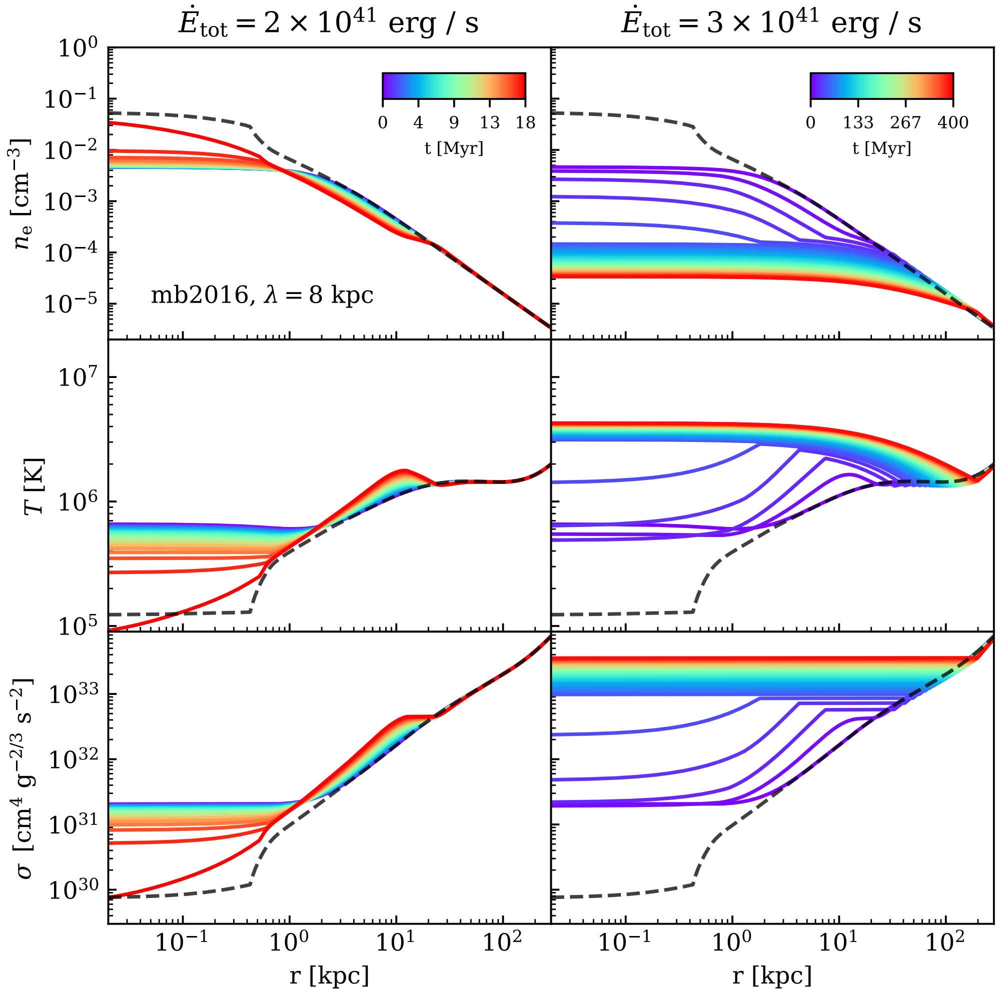

Figure 19: Full evolutions of the electron density, temperature and entropy-index of the lower (left column) and upper (right column) bounds to the threshold power of the `mb2016` corona with heating scale length $\lambda = 8\,\mathrm{kpc}$. The colour of the lines indicate the time of the evolution. For reference, the last timestep of the evolution without heating is included as a black dashed line (see Figure 15). The time-steps between the curves are $1\,\mathrm{Myr}$ and $10\,\mathrm{Myr}$ for the left and right columns respectively.

4 Discussion

In this Chapter, we discuss our results shown in Chapter 3. We start by comparing the threshold powers found in Section 3.3.1 to literature estimates of the Milky Way bubble power sources. Then, we test various assumptions and numerical details of our model, and discuss whether and how they influence our results. This includes, among others, the assumption of hydrostatic equilibrium, the assumed temperature in the initial condition and the starting radius for the integration of the corona. Finally, we discuss an analytic steady-state model for rotating cooling flows in the Milky Way by Stern et al. (2024), which is an extension of the nonrotating model (Stern2019), and show that this model is not applicable in the region where it would be most useful: close to the Milky Way disc.

4.1 Comparison with Milky Way bubble sources

We have seen that the evolution of a Milky Way-like corona is heavily influenced under the addition of a heating source originating from the centre of the system. Depending on the power of the source, the system will either be cooling or heating dominated and should transition between these regimes at some threshold power. Our results have shown that the threshold depends on the initial condition and scale length of the kernel, in general is of the order of $10^{41} - 10^{42}\,\mathrm{erg\,s^{-1}}$. Since the implementation of heating from the centre was motivated by existence of the Fermi and eROSITA bubbles, we compare our results to estimates of the power needed to inflate the bubbles (Miller & Bregman, 2016; Predehl et al., 2020; Yang et al., 2022). We first briefly describe what these estimates are, and how they are obtained and then proceed to compare them to our heating thresholds.

4.1.1 Estimates for sources of the Milky Way bubbles

Since the bubbles are observed as large conical structures above and below the GC of the Milky Way, it is most likely that their origin is tied to the GC as well. The most likely scenario is that these bubbles are inflated by an energetic episode, powered by nuclear star formation (NSF), or by the Milky Way's central massive black hole, called Sgr A* (Yang et al., 2018). Typically, the power of a NSF source, with SFR $\approx 0.08\,\mathrm{M_\odot/yr}$ in the Milky Way's GC, is considerably lower ($10^{40}\,\mathrm{erg\,s^{-1}}$, Crocker et al., 2015) than scenario's involving an AGN (above $10^{42}\,\mathrm{erg\,s^{-1}}$, Miller & Bregman, 2016). The scenario involving NSF, therefore requires a longer time-scale (at least $100\,\mathrm{Myr}$, Crocker et al., 2015) to form the bubbles, compared to the formation through an AGN (Yang et al., 2018). We will consider estimates from Miller & Bregman (2016) (Fermi) and Predehl et al. (2020) (eROSITA), who both estimated the power of the source that would inflate those bubbles, based on observations. Moreover, we consider the results from Yang et al. (2022) who simulated a short AGN episode producing a jet to form both bubbles.

Miller & Bregman (2016) observed regions close to the GC to constrain both the inner properties of the Milky Way's corona and the Fermi Bubbles. Using these parameters, they then proceded to estimate what power would be required to inflate these bubbles. They assumed that the bubbles are a continuous galactic outflow, in the energy conserving phase where radiative losses can be neglected (Weaver et al., 1977; Veilleux et al., 2005). The time since the creation of the bubble t_age, and the mechanical energy injection rate $\xi\dot{E}$ are then given as:

$$t_\mathrm{age} = 11.8\left(\frac{r}{10\,\mathrm{kpc}}\right)\left(\frac{v_\mathrm{exp}}{500\,\mathrm{km\,s^{-1}}}\right)^{-1}\mathrm{Myr} \tag{69}$$

$$\xi\dot{E} = 3.7\times10^{42}\left(\frac{n_0}{10^{-3}\,\mathrm{cm^{-3}}}\right)\left(\frac{r}{10\,\mathrm{kpc}}\right)^{2}\left(\frac{v_\mathrm{exp}}{500\,\mathrm{km\,s^{-1}}}\right)^{3}\mathrm{erg\,s^{-1}} \tag{70}$$

where r is the currently observed radius of the bubble, v_exp is the expansion velocity, n_0 the ambient density, $\dot{E}$ the energy injection rate and $\xi \sim 0.3$ the thermalization efficiency of the mechanical

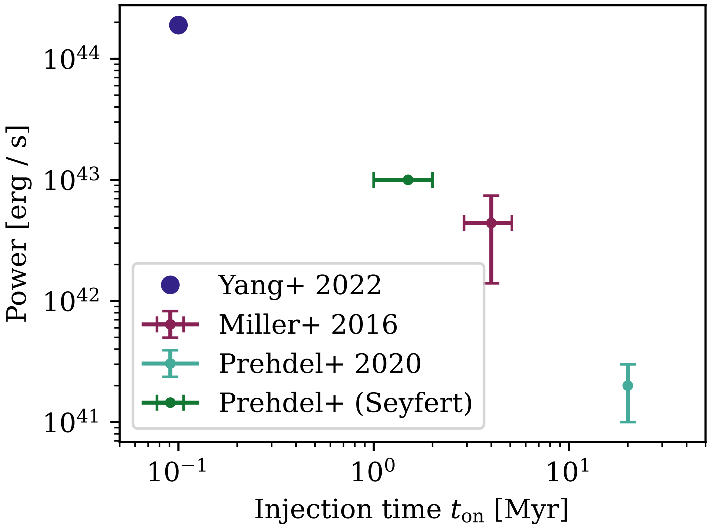

Figure 20: Literature estimates of the mechanical power and injection time of the Fermi and eROSITA bubbles of the Milky Way. The estimates from Miller & Bregman (2016) (Fermi) and Predehl et al. (2020) (eROSITA) are based on observations and assume the bubbles are winds powered by a continuously injecting central source. The Seyfert case from Predehl et al. (2020) assumes instead that the bubbles were formed by a shorter, more energetic episode. The estimate from Yang et al. (2022) is based on the simulation of a short, highly energetic jet that reproduces both the Fermi and eROSITA bubbles. The errorbars represent the range in the values as indicated by the respective authors.

luminosity. For their observed parameters of the Fermi Bubbles and including their uncertainties, they estimated the age of the bubbles to be $t_{\rm age} = 3 - 5\,{\rm Myr}$ and the combined energy injection for both bubbles to be $(2 \times \xi \dot{E}) = (1 - 7) \times 10^{42}\,{\rm erg\,s^{-1}}$.

In the discovery paper of the eROSITA bubbles by Predehl et al. (2020), they estimated the thermal energy of the bubbles based on their size, density and temperature of the emitting gas. Taking the observed size, and assuming $kT \approx 0.3\,{\rm keV}$ and $Z = 0.2 Z_\odot$ they estimated the electron density in the bubble to be $0.002\,{\rm cm^{-3}}$. Together this gives a thermal energy per bubble of $E_{\rm th} \approx 1.3 \times 10^{56}\,{\rm erg}$. Since the bubbles show a sharp boundary, they assumed the bubble is an outwards adiabatic shock, and find mach number $\mathcal{M} \approx 1.5$ (or outwards velocity $v \sim 340\,{\rm km\,s^{-1}}$) based on the difference between the temperature and density in-, and outside (Miller & Bregman, 2016) the bubble. The expansion time of such a bubble will then be $20\,{\rm Myr}$, which then corresponds to a source with power $(1 - 3) \times 10^{41}\,{\rm erg\,s^{-1}}$ during the expansion. They additionally speculate that the creation of the eROSITA bubbles would also be compatible with a short episode $(1 - 2\,{\rm Myr})$ of Seyfert-like activity from Sgr A*, with power $10^{43}\,{\rm erg\,s^{-1}}$.

More recently, Yang et al. (2022) showed with a hydrodynamical simulation that a short outburst event of Sgr A* would be able to create the structure of both the Fermi and eROSITA bubbles. They simulated a short outburst of $0.1\,{\rm Myr}$ that took place $2.6\,{\rm Myr}$ ago, using FLASH (Fryxell et al., 2000) a 3D adaptive mesh hydrodynamic code, using the CRSPEC module to model the evolution of the CR spectrum. The CR evolution assumes a *leptonic* model, where electrons are accelerated by the Sgr A* jet and lose energy via synchrotron radiation and inverse-Compton scattering. The total power of each Sgr A* jet is set to a value of $3.16 \times 10^{44}\,{\rm erg\,s^{-1}}$. At the end of the simulation, the morphology and sizes of both the Fermi and eROSITA bubbles are successfully reproduced.

The scenarios outlined above all give wildly different powers for the central energy source, mainly due to the different time-scales on which the energy is injected into the bubble. Of course, if the total energy of the Milky Way bubbles is fixed, a shorter injection time would imply a high power and conversely, a longer time-scale a lower power. In Figure 20, we have combined the

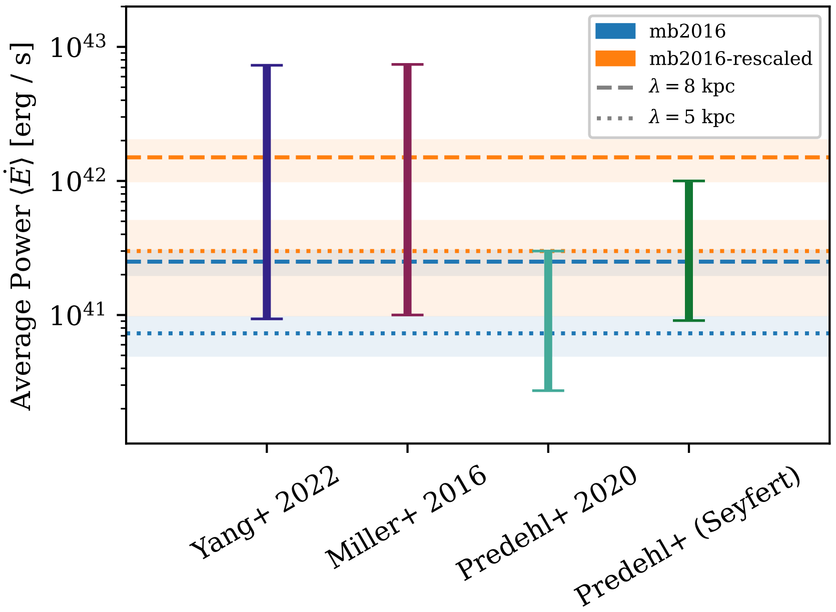

Figure 21: Combination of the threshold regions from Section 3.3.1 and literature estimates shown in Figure 20. The literature estimates are converted to average powers, as described in Section 4.1.2, where the upper and lower bounds represent the case with the smallest t_{off} and highest t_{off} respectively. The threshold regions, the range in power where the corona goes from being dominated by cooling to heating, from our results are indicated as blue (`mb2016`) and orange (`mb2016-rescaled`) patches and the value in the middle of the range shows the scale length as a dashed ($\lambda = 8\,\mathrm{kpc}$) or dotted ($\lambda = 5\,\mathrm{kpc}$) line.

estimated power and injection times of the four cases, where the errorbars correspond to the ranges in the estimates as reported by their authors. In the Figure we can clearly see here that the power estimates of the sources vary by three orders of magnitudes, and the injection time by 2. We can also see here that low injection times are paired with high powers, and vice versa. The time since the outburst could also be an important factor in the estimate of the power if the bubbles would lose a significant amount of their energy since the outburst, in particular due to radiation. However, Predehl et al. (2020) esimated that for the eROSITA bubbles the cooling time of the gas is of the order of $200\,\mathrm{Myr}$, so radiative cooling is unlikely to be an important factor for the time-scales that are considered here.

4.1.2 Comparison with the heating thresholds

Before we can compare our thresholds to the estimates of the Milky Way bubble power source, we have to account for the fact that our values are calculated using a continuous heating source. This is different from, for example, the process of AGN feedback, which is typically self regulating because the luminosity of the black hole is tied to its accretion rate. When the accretion rate is high, the black hole will have a high luminosity, heat the surrounding gas and consequently lowering the accretion rate. The fraction of the time the AGN spends in such an outburst state is called the duty cycle, typically being of the order of $10^{-3} - 10^{-2}$ (Cimatti et al., 2019). Such self regulation may also be relevant for the NSF, where gas needs to be cool to form stars, but the formation of young stars, together with the onset of type II supernovae, may stop the formation of more stars by heating the gas.

Assuming the energy source has an outburst of duration t_{on} with power $\dot{E}_{\mathrm{on}}$, and is off for remaining time t_{off} in the cycle (so $\dot{E}_{\mathrm{off}} = 0$), the average power injected in the system during a full cycle is given by

$$\langle \dot{E} \rangle = \frac{\dot{E}_{\text{on}} t_{\text{on}}}{t_{\text{on}} + t_{\text{off}}}. \tag{71}$$

In our model, heating is injected continuously into the system, so our threshold powers can already be interpreted as an average power. But to compare them to the estimates in the literature, we have to compute the corresponding average power for each estimate. If a system is self-regulating, it will have periods when it is dominated by heating (during the outburst) but also periods when it cools back down. On time-scales that are much larger than the duty cycle, the system will therefore not be cooling nor heating dominated, which means the average power of the source should be similar to our threshold power, or at least be somewhere in the transition region.

The duration of the outburst is given in all cases, and are $t_{\text{on}} = 3 - 5\,\text{Myr}$ for Miller & Bregman (2016), $t_{\text{on}} = 20\,\text{Myr}$ for the wind case and $t_{\text{on}} = 1 - 2\,\text{Myr}$ for the Seyfert-like case of Predehl et al. (2020) and $t_{\text{on}} = 0.1\,\text{Myr}$ for Yang et al. (2022). Estimating the time spent in the off state is difficult, so we consider extreme boundaries. For the lower limit of t_{off}, we take it to be equal to time between when the energy source stops emitting and now. This implies that the next energetic outburst of the source will occur very soon as well, which is an unlikely case. Both Miller & Bregman (2016) and Predehl et al. (2020), only estimate the age of the bubble together with the estimate for a continuous power source, so therefore we take $t_{\text{off}} = 0$, assuming the source keeps emitting energy up until very recently. For the Seyfert-like outburst, we assume this occured when the bubble was created ($20\,\text{Myr}$ ago), so accounting for the duration of the outburst, we take $t_{\text{off}} \approx 19\,\text{Myr}$. The time since the outburst simulated by Yang et al. (2022) is given explicitly, so we take $t_{\text{off}} = 2.5\,\text{Myr}$. For an upper limit on t_{off} we use the estimated cooling time of the eROSITA bubbles by Predehl et al. (2020) ($t_{\text{cool}} \sim 200\,\text{Myr}$), and add that to the lower limit of t_{off} for each case.

Figure 21 shows the calculated upper and lower limits of the average powers of the estimate from Miller & Bregman (2016), Predehl et al. (2020) and Yang et al. (2022) as vertical lines. Our ranges for the transition region, a range of powers between the regimes where our coronae are cooling and heating dominated, are indicated with blue (`mb2016`) and orange (`mb2016-rescaled`) horizontal patches, where the central value is marked with a dashed (scale length $\lambda = 8\,\text{kpc}$) or dotted ($\lambda = 5\,\text{kpc}$) line of the corresponding colour. We see that the estimates from Miller & Bregman (2016) and Yang et al. (2022) have the largest difference between the upper and lower limits, because the lower limit $t_{\text{on}} + t_{\text{off}} \leq 10\,\text{Myr}$ is very small compared to the cooling time of $200\,\text{Myr}$. It is also remarkable that the average power for these two estimates are almost identical, with Yang et al. (2022) being slightly lower. We previously saw a large scatter in the absolute values of the power estimates (Figure 20), but Figure 21 shows that the average powers of the estimates are considerably closer to each other, even when considering the large scatter in the values. The average powers from Predehl et al. (2020) estimates are lower than the estimates from Miller & Bregman (2016) and Yang et al. (2018), possibly because they only consider the energetics of the eROSITA bubbles.

When we compare our range for the transition region to the estimations from literature, we see that our values for the power thresholds for both coronae range from $5 \times 10^{40}\,\text{erg}\,\text{s}^{-1}$ to roughly $1 \times 10^{42}\,\text{erg}\,\text{s}^{-1}$, where the range from the literature values is similar, but has higher upper values for the average power. The transition region for the `mb2016` corona, with $\lambda = 8\,\text{kpc}$ and `mb2016-rescaled` corona, with $\lambda = 5\,\text{kpc}$ (middle two regions) are within the uncertainties of each of the literature estimates. The `mb2016-rescaled` corona, with $\lambda = 8\,\text{kpc}$ (upper line) is within the ranges off both Miller & Bregman (2016) and Yang et al. (2022), slightly outside the range of the Seyfert-like estimate and far from the wind estimate from Predehl et al. (2020). This latter estimate is also the only one that is of the same order as the lowest threshold from the `mb2016-rescaled` corona, with $\lambda = 8\,\text{kpc}$.

Overall it is remarkable that the transition regions estimated with our evolutionary model, are so similar to average powers of the Milky Way bubble sources as estimated in the literature. Apart from the simplicity of our model (for example spherical symmetry), we have only required that the inner source would be powerful enough to counterbalance rapid radiative cooling in the centre. The fact that the power we obtain is similar to the *observed* power of the bubbles suggests that the inner source in the Milky Way could be able to stop this cooling and onset a self-regulating mechanism that keeps the corona in equilibrium for very long times. The biggest discrepancy between our values and the ones from literature is at high average power. However, we note that this upper limit is estimated with $t_{\mathrm{off}} = 0$, implying the next energetic outburst of the source starts very soon, and is therefore likely too high of an upper limit.

4.2 Impact of our model assumptions

4.2.1 Temperature of the Milky Way corona

In the literature, the Milky Way corona is typically assumed to be isothermal with a temperature of $\log(T) = 6.3$ (**?**) or slightly lower around $\log(T) = 6.23$ (Ponti et al., 2023; Locatelli et al., 2024). For our initial conditions, we assume the density to follow a beta-model (Miller & Bregman, 2016) and the gravitational potential to be dominated by a NFW dark matter halo (see Section 2.4). When we then assume the corona is in hydrostatic equilibrium to find the pressure and temperature, we see that the corona is not fully isothermal (see for example middle panels of Figure 13).

We determine the boundary condition (P_∞) for the integration of Equations 5 and 6 by assuming that the temperature at the virial radius is equal to $\log(T) = 6.3$, the same temperature assumed by **?**. We can then compute P_∞ at this radius, since we know the temperature and density. Making this assumption on the temperature at $r = r_{\mathrm{vir}}$ results in temperature of the corona being lower than $\log(T) = 6.3$ for all $r < r_{\mathrm{vir}}$. However, observations of the Milky Way corona are mainly sensitive to the emission within a few tens of kpc from the Sun (for instance, 80 per-cent of the emission of the corona comes from $1\,\mathrm{kpc} < s < 20\,\mathrm{kpc}$, s being the distance from the Sun Locatelli et al., 2024), so ideally, the temperature in this region should then also be around the commonly assummed value of $\log(T) = 6.3$.

We produce new temperature profiles for our initial conditions, by assuming that at some different reference radius R_{ref}, the temperature is equal to $\log(T(R_{\mathrm{ref}})) = 6.3$. Similar to Section 2.4.3, we obtain $P(r)$ by integrating Equation 1 from 0 to r (Equation 56), but now find $P(0)$ by evaluating the integral on the RHS $I(r)$ at R_{ref}

$$P_0 = P(R_{\mathrm{ref}}) + I(R_{\mathrm{ref}}), \tag{72}$$

where $P(R_{\mathrm{ref}})$ we can find using the number density given by the β-model, and the assumed temperature at this radius. The full pressure profile is then obtained by evaluating $P(r) = P(0) - I(r)$ for radii between 0 and R_{out}. Finally, we compute the temperature profile using the ideal gas law. We note that for $R_{\mathrm{ref}} = R_{\mathrm{out}}$, this method produces the same temperature profile that we have used throughout the thesis.

Figure 22 shows the temperature (left) and pressure (right) profiles obtained by taking $R_{\mathrm{ref}} = r_{\mathrm{vir}}$, 100 and $10\,\mathrm{kpc}$. For these coronae, we used the density from `mb2016`. We see that all temperature profiles indeed match $\log(T) = 6.3$ (dashed grey line) at their respective R_{ref}. The temperature profile with $R_{\mathrm{ref}} = 100\,\mathrm{kpc}$ (green) is overall similar to the original profile with $R_{\mathrm{ref}} = r_{\mathrm{vir}}$ (blue), but diverges around $100\,\mathrm{kpc}$ and at the virial radius has a temperature of $4 \times 10^6\,\mathrm{K}$. The profile with $R_{\mathrm{ref}} = 10\,\mathrm{kpc}$, is very different, however, and increases rapidly starting at $3\,\mathrm{kpc}$. At the virial radius, the temperature of the corona is $10^8\,\mathrm{K}$, which is unrealistic for the Milky Way corona. To compensate for the higher temperatures at large r for $R_{\mathrm{ref}} = 10$ and $100\,\mathrm{kpc}$, the pressure is much lower. This could be advantageous for the numerical integration scheme, which would need less precision, since the difference between P_0 and P_∞ would be significantly lower.

For this work, assuming the temperature is $\log(T) = 6.3$ at r_{vir} is most appropriate, since overall it creates a temperature profile that is closest to $\log(T) = 6.3$. However, different initial conditions should be considered that give $\log(T) = 6.3$ around $10\,\mathrm{kpc}$, but also remain around this value at larger radii. A potential adjustment that could be made is in the gravitational potential of the system. For our model, we assume it is dominated by the dark matter halo everywhere, but we could also include the potential of the Milky Way disc, which would have large effects at low r.

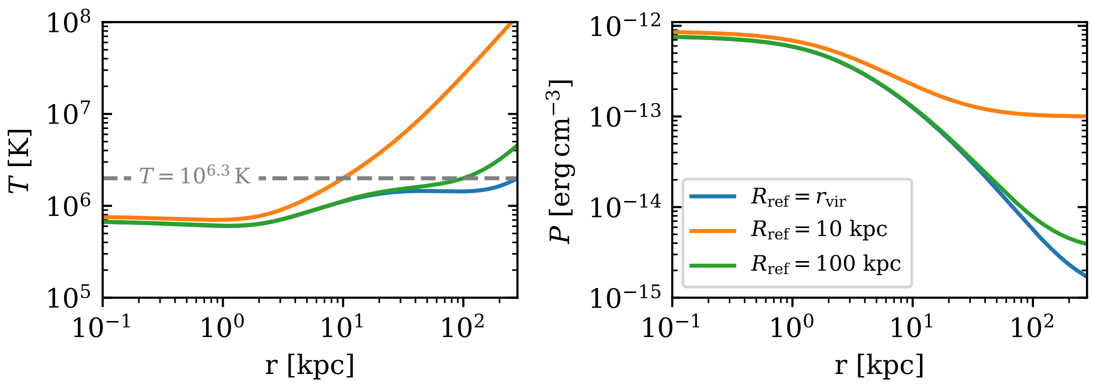

Figure 22: Initial profiles for the temperature (left) and pressure (right) for varying radii $R_{\rm ref}$ at which we assume the temperature to be equal to $\log T(R_{\rm ref}) = 6.3$ (grey dashed line). Throughout the thesis we have used $R_{\rm ref} = r_{\rm vir} = 282\,{\rm kpc}$ (blue line).

4.2.2 Assumption of hydrostatic equilibrium

At each time-step in the evolution of our model, we integrate the corona to get the pressure and mass profiles at the new time-step. For this, we assume that the corona is in hydrostatic equilibrium. However, since our model evolves the corona by heating or cooling, it is clearly not fully in hydrostatic equilibrium. But, if the time scale of the evolution is longer than the time the system needs to come to an equilibrium, we can expect that the corona time to re-adjust into a temporary equilibrium.

We can quantify this by comparing the speed at which the gas flows through the system, to the sound speed of the gas. If the flow speed is much smaller than the sound speed, our assumption of hydrostatic equilibrium can still be used (Forman et al., 1985). We compute the mach number ($\mathcal{M} \equiv |v_{\rm r}|/c_{\rm s}$) at radius r by dividing the radial velocity, calculated from the mass accretion (Equation 47), by the isothermal sound speed

$$c_{\rm s} = \sqrt{\frac{k_{\rm B}T}{\mu m_{\rm p}}}. \tag{73}$$

We use the isothermal sound speed, as opposed to the adiabatic sound speed, because our corona is explicitly evolving by a change in entropy and therefore cannot be adiabatic.

Figure 23 shows the evolution of the mach number of the `mb2016` (left) and `mb2016-rescaled` (right) coronae, evolved with classical cooling (Section 2.2.1). For both coronae, the mach number is small in the centre, increases with radius up to $1\,{\rm kpc}$ and then falls off again at large radii. This is very similar to the shape of the radial velocity, shown in Figure 14. The mach number peaks around $1\,{\rm kpc}$ at the end of the evolution, at value of roughly $\mathcal{M} \sim 1$. Everywhere else, the mach number is well below 1, and always stays below $\mathcal{M} = 0.1$ beyond $10\,{\rm kpc}$. Assuming hydrostatic equilibrium to integrate the corona at each time-step seems therefore a well-founded assumption.

4.2.3 Time-scale of convection

Our results have shown that when we evolve a Milky Way-like corona with our evolutionary model, a large negative entropy gradient develops in the centre of the corona, which makes this region convectively unstable. To avoid these unstable regions from forming, we implement a method from Binney et al. (2009), which at each time-step finds regions that have negative entropy gradients, and replaces the entropy of the entire region by the mass-weighted average of the entropy (see Section 2.2.4). Here, we compare the scale at which the convection takes place, to the sound speed of the system.

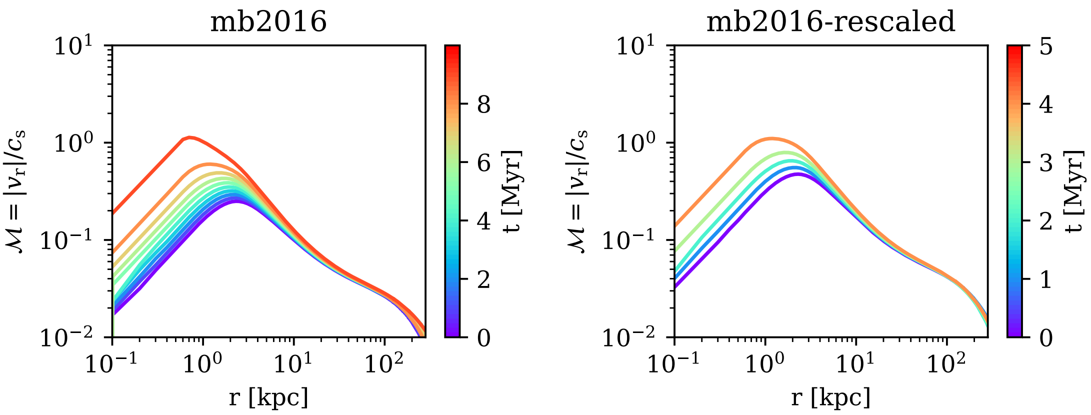

Figure 23: Evolution of the mach number $\mathcal{M} = |v_r|/c_s$ of the `mb2016` (left) and `mb2016` (right) coronae, using the CIE cooling function from SD1993.

We apply the convective method at each time-step, which are of the order $\delta t \sim 0.1 - 1\,\mathrm{Myr}$. From Figure 11, we see that the entropy is flat in the centre up to a radius of $1\,\mathrm{kpc}$, which means the convection method is applied on this scale. The temperature in this region is roughly $5 \times 10^5\,\mathrm{K}$, so the isothermal sound speed (Equation 73) is roughly $80\,\mathrm{km\,s^{-1}}$. Dividing the length scale by the sound speed gives us a rough indication of the time-scale at which convection can take place. For the length scale of $1\,\mathrm{kpc}$ and the sound speed at $T \sim 5 \times 10^5\,\mathrm{K}$ this will be $t_{\mathrm{conv}} \approx 12\,\mathrm{Myr}$. This time-scale is a factor $10 - 100$ longer than our time-steps of around $\delta t \sim 0.1 - 1\,\mathrm{Myr}$. The method for removing negative entropy gradient, therefore seems to act too fast on the system. However, we have seen in Section 3.1.1, that the evolution of the corona beyond the region that is cooling rapidly ($r > 3\,\mathrm{kpc}$) is not affected by the application of the convection method. Our results concerning the mass accretion in the outer parts of the corona, and the comparison with Stern et al. (2019), should therefore remain unaffected.

When we add heating from the centre to our evolution, we see (right column, Figure 17) that the region with constant entropy is significantly larger at the end of the evolution, extending even beyond $100\,\mathrm{kpc}$. Since the heating is injected into the centre of the system, the entropy will increase only here and hence the convection method will cause this entropy to be ‘transported’ outwards. The temperature in this region is now around $4 \times 10^6\,\mathrm{K}$, so $c_s \approx 230\,\mathrm{km\,s^{-1}}$. The time-scale on which the convection acts in the case of heating, is then $t_{\mathrm{conv,heat}} \approx (100\,\mathrm{kpc})/c_s \approx 400\,\mathrm{Myr}$ which is significantly longer than our estimate without heating. However, when we include heating from the centre, our results no longer focus on the precise evolution of the system. We are mostly concerned whether the corona is cooling or heating dominated. Convection will only ever transport entropy to larger radii, and as a consequence, the density (temperature) in the region from which the entropy is transported will only increase (decrease), and therefore the cooling in this region would become more efficient. So, by enabling convection, the cooling in the region which is heated can only become more efficient compared to the case without convection. If the corona is already heating dominated, it will therefore still be heating dominated when we would not use convection method, thus it will have no impact on our upper bounds of the power threshold.

The convective method could have an impact on the lower bound of the power threshold, however, if the length scale of the kernel would be much smaller than the region which is rapidly cooling. We would then get a situation, where within the length scale, the system would be heating and beyond it, the system would be cooling. However, as we see from the evolution of the corona with $\dot{E}_{\mathrm{tot}}$ at the lower bound of the threshold (left column, Figure 19), the opposite is the case, where the system is heating at $r \sim \lambda$ and is cooling at the centre. If we were to decrease the length scale, we would need to make sure that the convective method is adjusted such that it would act on time-scales of the same order as the time-step ($0.1 - 1\,\mathrm{Myr}$).

In conclusion, the scale at which our convection method acts seems to be too large compared to the length travelled at the sound speed of the system. However, we have also shown that our

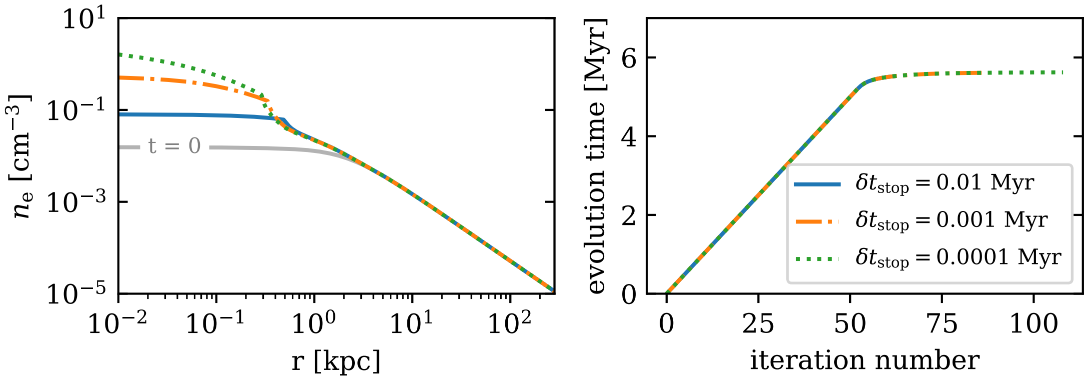

Figure 24: Comparison of the evolution of the `mb2016-rescaled` corona with classical cooling from SD1993 under different lower limits on the time-step: $\delta t_{\rm stop} = 0.01\,{\rm Myr}$ (blue, original), $0.001\,{\rm Myr}$ (orange dashed-dotted) and $0.0001\,{\rm Myr}$ (green dotted). The left Figure shows the electron density at the end of the evolution, when the time-step limit is reached, where the grey line indicates the density at $t = 0$. The Figure on the right shows the evolution time at each iteration,.

results are not significantly impacted by this convective method. Regardless, it is still important to investigate methods for removing these convectively unstable regions further, primarily in the case where there is an entropy generating source in the centre of the system.

4.2.4 Stopping conditions and evolution of the time-step

One of the numerical stopping conditions for our evolutionary model, is given by a lower limit on the time-step $\delta t_{\rm stop}$. For our results, we have set this limit at $\delta t_{\rm stop} = 0.01\,{\rm Myr}$, which is one to two orders of magnitude lower compared to the initial time-step $\delta t_0 = 0.1 - 1\,{\rm Myr}$. In this subsection we describe the evolution of the time-step δt, and then also justify why setting this limit does not affect our results.

As we have discussed before, cooling is a runaway effect, because when the gas cools, the density (temperature) increases (decreases) which results in even more efficient cooling (see Figure 4). Since, the cooling time sets the upper limit on the time-step to $t_{\rm cool}/10$, increased cooling will eventually decrease the time-step, and due to the runaway nature of cooling will keep decreasing it. Since there is no mechanism to stop the cooling, the time-step quickly decreases to a point where the evolution no longer progresses.

Figure 24 shows the effect of various $\delta t_{\rm stop} = 0.01, 0.001, 0.0001\,{\rm Myr}$ on the evolution of the `mb2016-rescaled` corona, with classical CIE cooling from SD1993. On the left side we see the electron density at the final time-step, for the various $\delta t_{\rm stop}$, where a smaller value will result in a higher density in the centre of the corona. However, the corona beyond $1\,{\rm kpc}$ stays the same. On the right panel we see the evolution time as a function of iteration number. For the first 50 iterations, the time-step stays constant, and the evolution time therefore increases the most here. Then, the time-step is lowered quickly due to the cooling and immediately flattens out. All three stopping conditions follow the same curve, but naturally stop at a different iteration number. The final evolution times for the three stopping conditions are almost equal at 5.52, 5.61 and $5.62\,{\rm Myr}$ for $\delta t_{\rm stop} = 0.01, 0.001, 0.0001\,{\rm Myr}$, respectively. Even though the density in the centre is affected by the limit on the stopping condition (see Equation 66, and Figure 24), the density beyond $1\,{\rm kpc}$ is not, and since changing the stopping condition does not affect the evolution time significantly, our results are not affected by using $\delta t_{\rm stop} = 0.01\,{\rm Myr}$.

The evolution of the time-step in the case where the corona is being heated, is slightly different compared to the cooling case. The time-step is still determined by the time-scale of energy change t_ϵ, which now depends on both cooling and heating as $t_\epsilon \propto 1/(n|\Lambda - \Gamma|)$ (Equation 18, with $\mathbb{L} \propto n^2(\Lambda - \Gamma)$). Since our model includes continuous heating with a constant power, Γ is constant and if the heating is dominant, $\Gamma > \Lambda$. Moreover, because the corona is heating, the density increases,

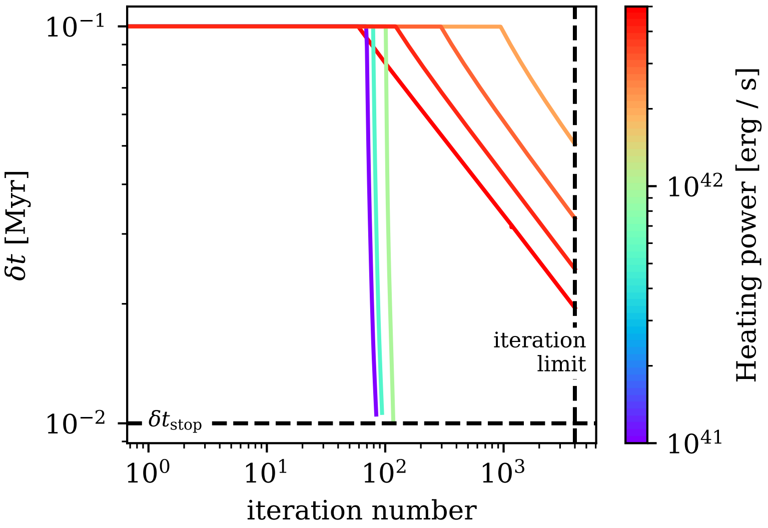

Figure 25: Comparison of the change in timestep δt as a function of iteration number for the `mb2016-rescaled` corona under varying heating powers $\dot{E}_{\mathrm{tot}}$ (indicated by colour) with $\lambda = 8\,\mathrm{kpc}$. The stopping conditions on the evolution, lower limit on time-step $\delta t_{\mathrm{stop}} = 0.01\,\mathrm{Myr}$ (horizontal) and an upper limit on the number of iterations $N_{\mathrm{iter}} = 4000$ (vertical) are included as black dashed lines. The green/blue lines are in the regime where cooling is dominant, and the orange/red lines are in the regime where heating is dominant.

which in turn decreases Λ, and as a result, t_ϵ will become smaller. In this case, the time-step also decreases, but now it decreases much less rapidly compared to the cooling case. We can see this in Figure 25, where we show δt over the entire evolution of the `mb2016-rescaled` corona, for varying $\dot{E}_{\mathrm{tot}}$. In all the cases, the timestep stays constant for roughly the first 100 iterations, while afterwards we can see differences. As we have seen before, when cooling is dominant (green and blue lines) δt decreases rapidly until it reaches δt_{stop}. The red and orange colours indicate evolution where heating is dominant, and we see that δt decreases much more slowly and only stops because we have set a limit of 4000 iterations. We also see that coronae with a smaller $\dot{E}_{\mathrm{tot}}$ (but still heating dominated), decrease their time-step later in the evolution compared to coronae with higher $\dot{E}_{\mathrm{tot}}$, resulting in a longer evolution time.

We see that the evolution that are dominated by heating all stop when the iteration limit of $N_{\mathrm{iter}} = 4000$ is reached. In principle, the evolution can continue beyond this point, but it will not change whether the corona is heating or cooling dominated. Varying this limit will significantly change the total evolution time of these system, which is the reason why we cannot put them in a physical context. But, the limit will not affect the upper bound on the power threshold and therefore not influence our results in this regard.

4.2.5 `CLOUDY` cooling and heating

In our results (Section 3.2) we have seen that when we use `CLOUDY`, with photoionisation from the extragalactic UVB, to calculate how the entropy evolves over time (see Section 2.2.2), the centre of the corona cools slightly more slowly compared to when we use classical cooling from SD1993. Here, we investigate if this is due to the different calculations made in the cooling function (Λ) by `CLOUDY`, compared to SD1993 or due to the addition of heating through photoionizing radiation from the extragalactic UVB. We evolve the `mb2016` corona again, with identical parameters to the evolution shown in Figure 15, but now we no longer consider the heating from photoionisation. Figure 26 shows the electron density (left) of the corona with (blue) and without (orange) photoionisation at $t = 8\,\mathrm{Myr}$. Because the differences are not visible by eye, the right panel shows the difference between the electron density with (n_{e}) and without ($n_{\mathrm{e,noheat}}$) photoionisation. In

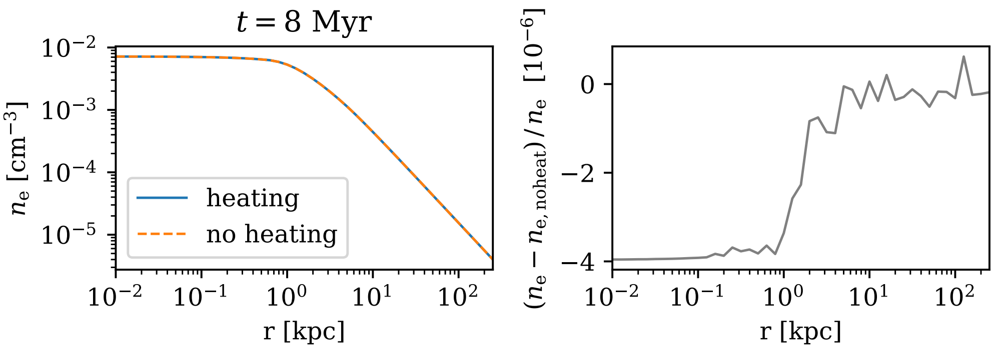

Figure 26: Comparison of evolution of the `mb2016` corona with convection between cooling from `CLOUDY` with (blue) and without (orange, dashed) heating from photoionisation. The left panel shows the electron densitiy at $t = 8\,\mathrm{Myr}$ for both cases. The right panel shows the difference between the density with heating n_e and without heating $n_\mathrm{e,noheat}$, at the same time-step. The scale of the vertical axis is in units of 10^{-6}.

this panel, we see that the difference is negative for $r < 1\,\mathrm{kpc}$, and for larger radii is around 0. This implies that $n_\mathrm{e} < n_\mathrm{e,noheat}$ in the centre, which is the region that in general has the most cooling. A higher density for $n_\mathrm{e,noheat}$ is expected, since no heating would results in a higher net cooling rate. The relative difference between the two cases, however, is of the order 10^{-6}, which is incredibly small. At large radii, we do not see much difference, which is most likely because the cooling rate in this region is much lower.

Since the difference between the cases is very small, this tells us that photoionisation from the UVB does not play a significant role in the evolution of the corona. Figure 27 shows the net cooling function from `CLOUDY` with (black) and without (grey) photoionisation for metallicities $Z = 0.1\,\mathrm{Z}_\odot$ (left) and $Z = 0.3\,\mathrm{Z}_\odot$ (right). In this figure, we see that for all densities and both metallicities, beyond $T > 10^5\,\mathrm{K}$ the net cooling functions with and without heating are identical. Only at lower temperatures we see the difference caused by photoionisation. For the evolution with our coronae, we see that (for example in Figure 15) the temperature of the corona always remains above $T > 10^5\,\mathrm{K}$. Combined with the fact that photoionisation only becomes relevant below this temperature, this explain why it seems that photoionisation does not have any effect on the cooling of the corona. Photoionisation can still have an impact when the corona cools below $T < 10^5\,\mathrm{K}$, for instance, when the gas is accreted by the galaxy. It therefore follows that photoionisation mostly plays a role at the interface between the corona and the Milky Way disc, which we do not consider in our model.

4.2.6 Integration with nonzero starting radius

A dominating factor in our results is the fact that cooling is most rapid within the few outer kpc of the corona. As a result, most of the evolution in density, temperature and entropy also occurs in this region. In reality, however, this region harbours the stellar disc and bulge together with the gaseous disc of the Milky Way, so several of our assumptions break down. The Milky Way disc is mostly an axisymmetric system, with rotation around the axis perpendicular to it. Therefore, assuming a spherically symmetric and non-rotating corona will not be valid in this region. Moreover, the gas in the corona close to the galaxy, will likely interact with it. For example, the gas can be reheated by galactic feedback, which would affect the equilibrium of the corona. A possible solution is to avoid integrating this inner region altogether, but this is not possible in the model due to our boundary conditions.

The integration of the equations for hydrostatic equilibrium (Equations 5 and 6) starts at $r = 0$, which allows us to safely assume the boundary condition on the mass $M(r = 0) = 0$. If one were to start the integration from some point $r_0 > 0$, we would need to also know $M(r_0)$. At $t = 0$ this is not a problem, since $\rho(r)$ is known and we can integrate the density to get $M_{t=0}(r_0)$. The

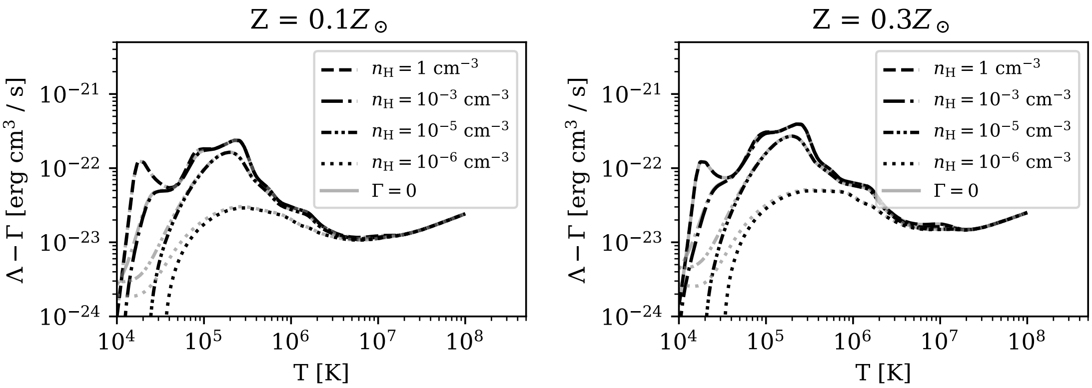

Figure 27: Net cooling functions (cooling Λ minus heating Γ) from `CLOUDY` (Ferland et al., 2013) with photoionisation from extragalactic UVB from Haardt & Madau (2012) for hydrogen densities between $n_H = 1 - 10^{-6}\,\mathrm{cm}^{-3}$ (black lines), and without photoionisation (grey lines). The figure on the left shows the net cooling functions for $Z = 0.1\,\mathrm{Z}_\odot$ and the figure on the right for $Z = 0.3\,\mathrm{Z}_\odot$.

issue arises however when we perform the first time evolution step by changing the entropy (see Section 2.1.2) and have to integrate using the new boundary condition. Let us say that this new integration occurs at time t_1 and the time before the update step is t_0, we then need to know $M_{t_1}(r_0)$ *before* we start the integration. When the corona cools, it constracts and the new mass at this radius will be higher than before: $M_{t_1}(r_0) > M_{t_0}(r_0)$. The difference between these two masses is given by $\dot{M}_{t_0}(r_0)\delta t$, where $\dot{M}_{t_0}(r_0)$ is the mass accretion rate at t_0 and δt is the time-step used in the update step. In order to know $\dot{M}(r_0)$, for instance by using the forward difference approximation (Equation 45), we need to know $M_{t_1}(r_0)$, which is unfortunately exactly the boundary condition that we want to find out. In order to find an appropriate value for this boundary condition, we therefore would have to make some additional assumptions or completely change the integration scheme.

Changing the integration scheme is beyond the scope of this work, however we could still make a simple assumption in order to check if the outer part of the corona is affected by the rapid cooling in the centre. We make the assumption that mass does not flow through our boundary condition at r_0, which would keep $M(r_0)$ constant over time. With this assumption, we evolve the `mb2016` corona, with SD1993 cooling and convection (Section 2.2.4) for starting radii of $r_0 = 0.1, 1$ and $10\,\mathrm{kpc}$. The resulting mass accretion profiles can be seen in Figure 28, where the result with $r_0 = 0.1\,\mathrm{kpc}$ (left) and $r_0 = 1\,\mathrm{kpc}$ (right) can be seen on the top row, and $r_0 = 10\,\mathrm{kpc}$ in the bottom left panel. We can see that the mass accretion profiles and evolutionary times for the 0.1 and $1\,\mathrm{kpc}$ are very similar to the normal evolutionary runs starting at $r = 0$ (bottom right panel). This is because these starting radii are still within the region with rapid cooling (Figure 11), and therefore the effect on the outer parts of the corona will be similar. The main difference, due to the integration starting at larger radii, is the mass pile up at r_0, which we can see by the mass accretion approaching 0 at the starting radius. This is of course expected, as we assumed $M(r_0)$ to be constant here.

The evolution with starting radius $r_0 = 10\,\mathrm{kpc}$ is a bit more interesting, because this starting radius is in a regime which does not cool rapidly within a few Myr. In this case, we see that the evolution also runs for significantly longer ($> 300\,\mathrm{Myr}$), but the mass accretion profile still stays relatively constant beyond $30\,\mathrm{kpc}$. The value of the mass accretion rate in the regime where it is constant, is around $\dot{M} \simeq 0.2\,\mathrm{M}_\odot/\mathrm{yr}$. This value is similar to what we find for the mass accretion in our integration starting from $r = 0$ (Section 3.2.1). We therefore can conclude that the rapid cooling of the inner corona does not seem to have a significant effect on the outer regions of the corona, meaning our estimation of $\dot{M}$ and comparison with the cooling flow model from Stern et al. (2019) still holds. In other words, our model with pure radiative cooling also reaches a steady-state inflow with similar properties to a model specifically designed with that purpose.

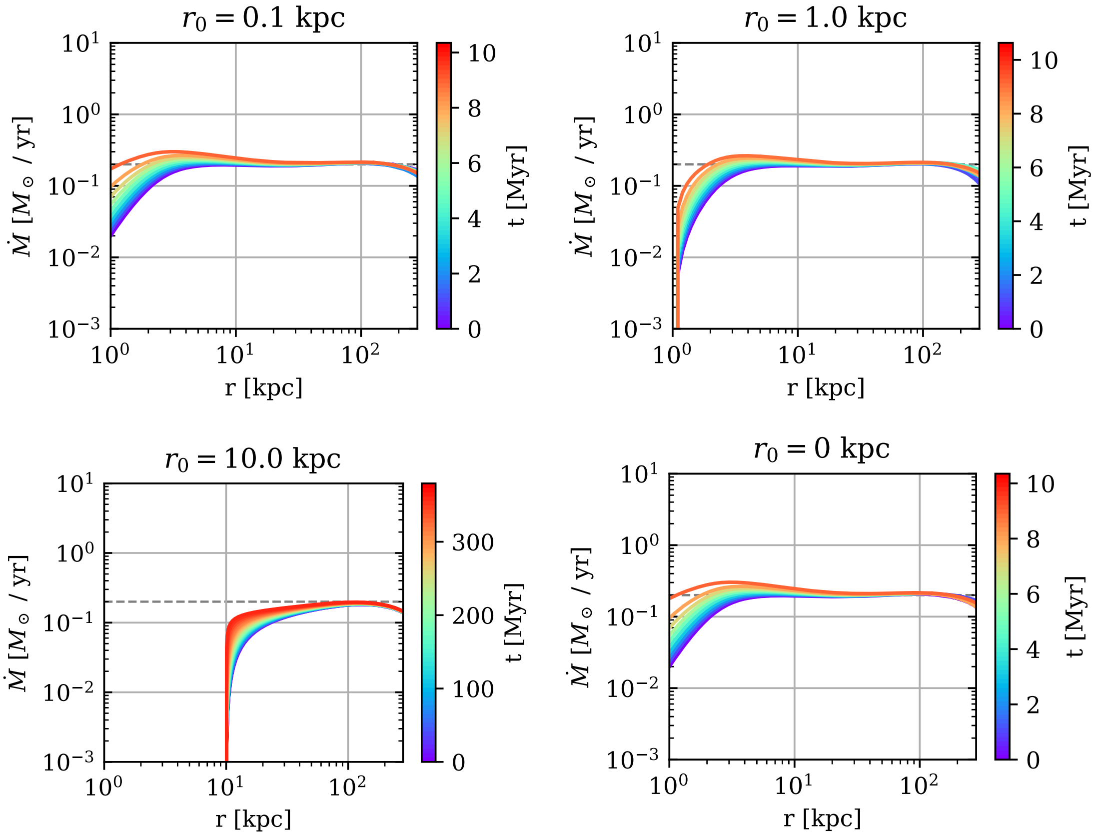

Figure 28: Evolution of mass accretion profiles for nonzero starting radius $r_0 = 0.1, 1.0$ and $10\,\mathrm{kpc}$ for the integration of the `mb2016` corona, with classical CIE cooling from SD1993 and with convection enabled. The original mass accretion profile for $r_0 = 0$, can be seen in the bottom right (similar to Figure 12). A grey dashed horizontal line is included to indicate $\dot{M} = 0.2\,\mathrm{M}_\odot/\mathrm{yr}$.

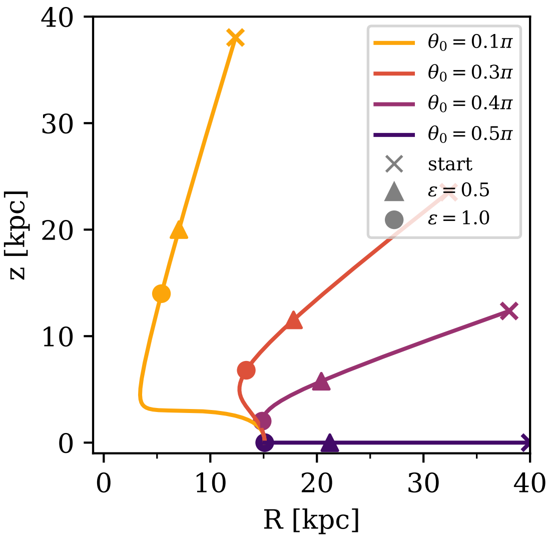

Figure 29: Integrated particle paths tracing the velocity field of the analytic steady-state cooling flow solutions with rotation from Stern et al. (2024). The four different particles start at $r = 40\,\mathrm{kpc}$ with varying starting angles $\theta_0 = 0.1\pi, 0.3\pi, 0.4\pi$ and 0.5π. The starting position is indicated with a cross, and the positions where the particle first attains $\varepsilon \geq 0.5$ and 1.0 are indicated by a triangle and circle respectively. To compute the velocity fields, we take $R_{\mathrm{c,max}} = 15\,\mathrm{kpc}, v_c = 200\,\mathrm{km\,s^{-1}}$, $\dot{M} = 2\,\mathrm{M_\odot/yr}$ and $\Lambda = 0.6 \times 10^{-22}\,\mathrm{erg\,s^{-1}\,cm^3}$.

4.3 Steady-state cooling flows with rotation

In this thesis, we have compared our results of applying an evolutionary model from Kaiser & Binney (2003) to the corona of the Milky Way, with analytic solutions of steady-state cooling flows from Stern2019 (Section 2.5). We saw that at large radii, these models produce almost identical results, since when we use the mass accretion calculated from our evolutionary model as a parameter in the cooling flow model, the same density distribution is recovered. The main disadvantage of both models is that they assume a spherical system with no rotation, which is clearly not valid close to the Milky Way disc. To solve this issue, the nonrotating cooling flow model was recently extended to include rotation by Stern et al. (2024). This would be a significant step forward, but we have noticed that the assumptions of this model break down for small radii, as we will show in this section. Unfortunately, the region where this model would mainly improve upon the non-rotation solutions from Stern2019 is close to the rotating Milky Way disc, where r is also small. Far away from the disc, the rotation is small and the non-rotating model already works, which means we also have no need for this model in this region. Taking these two together, the model from Stern et al. (2024) does not improve upon the non-rotating model. We will first explain how the nonrotating analytic solutions are extended to include rotation (for a detailed derivation see the original paper by Stern et al., 2024), and then show that the model fails when the radius is too small.

4.3.1 Derivation of the rotating solutions

Similar to the non-rotating solutions, they make the assumption that a cooling flow of gas exists in a halo, where the gravitational potential of the dark matter halo is dominant and can be described by the circular speed $v_c(r)$ being a powerlaw in r. Instead of a spherically symmetric system, they now assume that the system is rotating with angular frequency Ω about the z-axis, and is axisymmetric around this axis. The angle θ is then the angle between the z-axis and the $x - y$ plane, starting from $\theta = 0$ along the z-axis. Since the system is now axisymmetric, properties of the gas are described by r and θ (as opposed to only r in a spherical system). The effects of rotation increase as the flow approaches the disc in the centre of the system, thus with decreasing r, so they introduce a pertubation parameter

$$\epsilon \equiv \left(\frac{r}{R_{\mathrm{c,max}}}\right)^{-2}, \tag{74}$$

where $R_{\mathrm{c,max}}$ is the maximum radius in the $x-y$ plane where the aximuthal velocity v_ϕ of the gas is equal to the circular velocity v_c. The gas properties, then, are taken to be first order pertubations in ϵ

$$P_1(r,\theta) = P_0(r)[1+\epsilon(r)f_P(\theta)], \tag{75}$$
$$\rho_1(r,\theta) = \rho_0(r)[1+\epsilon(r)f_\rho(\theta)], \tag{76}$$
$$v_{r,1}(r,\theta) = v_{r,0}(r)[1+\epsilon(r)f_{v_r}(\theta)], \tag{77}$$
$$v_{\theta,1}(r,\theta) = v_{r,0}(r)\epsilon(r)f_{v_\theta}(\theta), \tag{78}$$

where the subscript 0 implies the quantity is given by the nonrotating cooling flow solutions of Stern2019 and subscript 1 denotes the solutions with rotation. The functions $f_q(\theta)$ for quantity q are arbirary functions of θ and they are found by inserting the perturbed solutions (Equations 75-78) into the hydrodynamical equations with rotation (see Stern et al., 2024, Section 2.4). The full solutions for pressure, density and velocity are then given by

$$P_1(r,\theta) = P_0(r)\left[1+\frac{R^2_{\mathrm{c,max}}}{r^2}\left(\frac{3}{4}\sin^2\theta-\frac{5}{8}\right)\right], \tag{79}$$
$$\rho_1(r,\theta) = \rho_0(r)\left[1+\frac{R^2_{\mathrm{c,max}}}{r^2}\left(\frac{11}{4}\sin^2\theta-\frac{35}{24}\right)\right], \tag{80}$$
$$v_{r,1}(r,\theta) = v_{r,0}(r)\left[1-\frac{R^2_{\mathrm{c,max}}}{r^2}\left(\frac{23}{12}\sin^2\theta-\frac{65}{72}\right)\right], \tag{81}$$
$$v_{\theta,1}(r,\theta) = -v_{r,0}(r)\frac{R^2_{\mathrm{c,max}}}{r^2}\frac{5\sin(2\theta)}{18}. \tag{82}$$

4.3.2 Application to the Milky Way

When we apply these solutions to the Milky Way, however, we are unfortunately still restricted to regions far away from the disc. We can almost directly see this from the pertubation parameter ϵ (Equation 74), which should remain small $\epsilon \ll 1$, so

$$r^2 \gg R^2_{\mathrm{c,max}}. \tag{83}$$

Taking the value of $R_{\mathrm{c,max}} \approx 15\,\mathrm{kpc}$ for a Milky Way like disc, equal to the value used by Stern et al. (2024) we see that the radius must be much larger than the size of the Milky Way disc. Moreover, since the scale height of the disc is roughly $1\,\mathrm{kpc}$ (Cimatti et al., 2019), the cooling flow will hit the point of $r \sim R_{\mathrm{c,max}}$ significantly before it is close to the disc. To visualize the flows described by these solutions, we put four particles at $r = 40\,\mathrm{kpc}$ for angles $\theta_0 = 0.1\pi, 0.3\pi, 0.4\pi$ and 0.5π and integrate their paths according to the velocity field defined by Equations 81 and 82. We can see the resulting traces edge-on in Figure 29, where the horizontal axis shows the radius R in the plane of the disc and the vertical axis shows the height above the disc z. The starting locations are marked by a cross and the location in the flow where for the first time $\epsilon = 0.5$ and 1.0 are marked by triangles and circles respectively. We see that close to the starting location the flows are similar to radial flows described by the non-rotating solution. As the radius decreases, the solutions deviate slightly from the radial solutions, and slowly tend to turn towards the point with $R = R_{\mathrm{c,max}}$, $z = 0$. At the end, all the particles end up at this point by construction, where the paths with starting angles $\theta_0 = 0.1\pi$ and 0.3π have to make extreme turns in order to get there. Clearly this behaviour is not physical, and indeed it all happens within $r < R_{\mathrm{c,max}}$, where the assumption of perturbative flow is no longer valid.

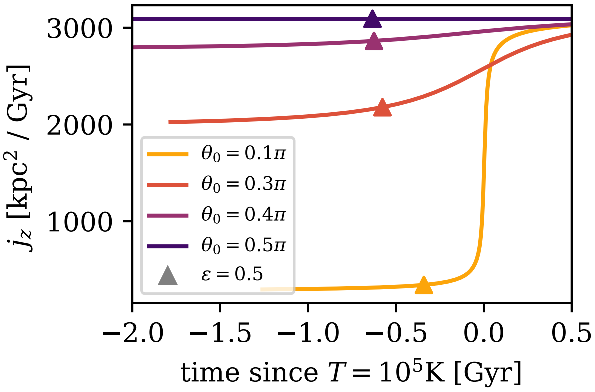

Figure 30: Evolution of the specific angular momentum (in the z-axis) of the same 4 particles from Figure 29. The horizontal axis is shifted such that $t = 0.0$ indicates the time of which the temperature of the gas in the flow is $T = 10^5\,\mathrm{K}$ (the temperature is higher before). The triangle indicates the position where $\varepsilon = 0.5$ for the first time.

This same note was made by Cassen & Pettibone (1976), who studied accretion via rotating Bondi flows. Their approach is similar, where the rotating solution is a first order pertubation in small $\varepsilon \equiv (\Gamma_\infty c_\mathrm{s}/GM)^2$, where Γ_∞ is the specific angular momentum far away from the centre, c_s the sound speed and M the mass of the accreting body. For their pertubations, the zeroth order solution is also equal to the original non-rotating solutions by Bondi (1952) for spherically symmetric accretion. Similar to our Figure 29, Cassen & Pettibone (1976) show the velocity vectors of the accretion flow at multiple scales. The scale that corresponds to the region where the solutions are invalid is shown in Figure 3c of their paper, where we see the exact same turns close to the rotating plane that we see in the paths starting at low θ_0.

4.3.3 Conservation of angular momentum

In an axisymmetric system, the specific angular momentum of gas along the axis perpendicular to the plane of rotation j_z is expected to be conserved along flowlines, which is also shown explicitly by Stern et al. (2024), Equation 20. We compute the specific angular momentum of the gas along the track of the cooling flow by Stern et al. (2024) for the four particles starting at $r = 40\,\mathrm{kpc}$, and initial angle θ_0 from 0.1π to 0.5π (same as Figure 29) as

$$j_z = \Omega r^2 \sin^2\theta, \tag{84}$$

where Ω is the angular frequency of the rotating gas. Figure 30 shows how the angular momentum changes for these particles, along the flow, up to the point where it reaches a temperature of $T = 5\,\mathrm{K}$. In the simulations of Stern et al. (2024) this point indicates when the particle cools and is accreted by the disc, and angular momentum is conserved up to this point (see Figure 4 from their paper). We can see that j_z of the particle initially placed in the plane of the disc ($\theta_0 = 0.5\pi$), is indeed conserved, as it stays constant across all time. The other three particles, however, all increase in j_z when they get closer to the disc, where the biggest increase is for $\theta_0 = 0.1\pi$, close to the point where $T = 10^5\,\mathrm{K}$. We note that j_z already increases before the perturbation parameter becomes too large ($\varepsilon \geq 0.5$, indicated by the triangle). This shows that in general, angular momentum is not conserved for the rotating solutions described by Equations 79 – 82.

It is therefore evident that close to the disc of the Milky Way, where the pertubation parameter becomes too large, and angular momentum is also no longer conserved, we cannot use the solutions for steady-state cooling flow with rotation. This unfortunately defeats the purpose of the model, since this is exactly the region where the non-rotating solutions from Stern2019 are no longer applicable. In the regime far away from the galaxy, the rotating solutions are valid, but become identical to the non-rotating solutions, so they do not improve upon the non-rotating model.

4.4 Future Work

One of the most obvious improvements to the model developed here, would be to add angular momentum, which becomes mainly important close to the centre of the system. How this could be implemented in the model is not obvious, but most certainly would require the system to be axisymmetric. Moreover, the integration process of the static corona would also have to be changed significanly, since we would also have to integrate over θ, the angle between the axis and plane of rotation, in addition to the current integration over the radius.

Our implementation of the heating source can also be studied further, where our results have shown that the shape of the kernel influences the strength of the source required to stop the corona from cooling. Additionally, the region of the corona that is heated extends to a significantly larger scale ($r > 100\,\mathrm{kpc}$) than the size of the Milky Way bubbles ($r \sim 10\,\mathrm{kpc}$). It could be interesting to adjust the shape and size of the kernel to produce a scale that is closer to the Milky Way bubbles.

Moreover, our heating source mainly considers the effect of mechanical feedback, which is typically relevant for AGN or starburst driven winds (Veilleux et al., 2005) and AGN in radio mode (Cimatti et al., 2019). We do not consider the effect of radiation, which is important if an AGN accretes fast enough to be have quasar mode feedback (Cimatti et al., 2019). The radiation could serve to photoionise the gas in the corona, which would have an impact on the equilibrium calculations in the cooling function. Including radiation could be important for studying the source of the Milky Way bubbles, since the Magellanic Stream shows evidence of large-scale ionization cones originating from Sgr A* (Bland-Hawthorn et al., 2019). Including this in our model can in principle be done using `CLOUDY`, where we would then include such a radiative source in the calculation of the cooling rates.

In calculating the average power of estimates from the Fermi and eROSITA bubble sources, we had to assume how long it will take until the next energetic outburst occurs, t_{off}. We took the extreme upper bound to be $t_{\text{off}} = 0$, and the lower bound to be $t_{\text{off}} = 200\,\mathrm{Myr}$, motivated by the cooling time of the eROSITA bubbles (Predehl et al., 2020). In principle, we could use our model to get a more refined estimate of t_{off} by starting the evolution from an initial condition which includes the Milky Way bubbles, and then let the system evolve by only cooling. Such an initial condition could be based on observations of the bubbles, or based on our own results from a corona dominated by heating. We have shown that, with heating, such a corona produced densities and temperatures similar to those present in the Fermi bubbles. The time the system would evolve could then be used to obtain a self-consistent estimate for t_{off}.

Our current density distribution for the initial condition is based on observations from **?** and further constraints in the centre by Miller & Bregman (2016). More recent observations of the Milky Way corona exist (Locatelli et al., 2024), which also show the presence of a large disc-like component, closer to the galaxy. These observations are not constrained in the centre however, which is needed in order to start the integration from $r = 0$, so if these constraints were to be added, this distribution could be used as a new initial condition.

The corona in our model is assumed to be supported by thermal pressure. However, turbulence (Buie et al., 2020; Chen et al., 2023) and cosmic rays (Salem et al., 2016; Ji et al., 2020) can also contribute significantly to the total pressure of coronal gas. CGM models that consider such additional pressure terms (for example Faerman et al., 2017; Dutta et al., 2024) are typically able to reproduce the emission and absorption from [OVI] (Tumlinson et al., 2017) significantly better compared to models like Gupta et al. (2012) and **?**, that are based on [OVII] and [OVIII]. In principle, it is possible to add additional pressure terms to our model, which would require modifying Equation 1.

A technical improvement can be made in the efficiency of the implementation of the PCHIP interpolation scheme on a 3 dimensional grid. Currently, this uses a pure Python implementation from Scipy (Virtanen et al., 2020), and is a large bottleneck in the evolution which use the `CLOUDY` cooling/heating prescription. Improving this implementation, for example with just-in-time (JIT) compilation from `Numba` (Lam et al., 2015), would allow the evolution to either run for longer, have a smaller timestep, or it would be possible to run a finer grid search to find bounds to the threshold power.

5 Conclusions

In this thesis, we have studied the evolution of a Milky Way-like hot CGM (or corona) using an evolutionary semi-analytic model from Kaiser & Binney (2003). This model assumes that the corona is approximately in hydrostatic equilibrium, and evolves through a changing of the entropy using classical CIE cooling. We have extended this model to use a non-CIE cooling function (`CLOUDY`), and have included heating by photoionisation from the extragalactic UVB and heating from a central heating source. We have evolved this model using two initial conditions, one based on observations of the Milky Way corona (`mb2016` **?**Miller & Bregman, 2016) and one being a rescaled version of the first model motivated by recent observations of stacked MW-mass galaxies (Bregman et al., 2022; Zhang et al., 2024, `mb2016-rescaled`). The `mb2016` and `mb2016-rescaled` coronae have total masses at $r = r_{\rm vir}$ being 10 and 30 % respectively of the missing baryons in the Milky Way. The respective metallicities are assumed to be $Z = 0.3$ and $0.1\,Z_\odot$. The results of evolving the Milky Way-like coronae with the various cooling/heating prescriptions can be summarised as follows

1. When we evolve the two coronae with classical cooling (Sutherland & Dopita, 1993) and with `CLOUDY` (Ferland et al., 2013), we see that the centre ($r < 1\,$kpc) of the corona cools within 10 Myr, where the `mb2016-rescaled` corona cools roughly a factor 2 faster than the `mb2016` corona. During the evolution, the mass accretion beyond 20 kpc is roughly constant up to the virial radius, at approximate values of $\dot{M} \simeq 0.2\,M_\odot$ for `mb2016`, and $\dot{M} \simeq 1.0\,M_\odot$ for `mb2016-rescaled`, and only increases slightly across the evolution of the corona. This shows that the rescaled Milky Way corona would be able to sustain the star formation in the Milky Way in its own, whereas the corona as observed by **?** needs an additional mechanism of gas accretion. For both cases, the Milky Way would not need much feedback to limit excess gas accretion, since the accretion rates are of the same order, or lower than the SFR observed in the Milky Way.

2. The density, temperature and radial velocity of both coronae beyond 10 kpc are very similar to the profiles predicted by the cooling flow model from Stern et al. (2019), which shows that an isolated cooling corona in approximate hydrostatic equilibrium produces the same distributions as one with the assumption of a steady-state cooling flow with accretion from the IGM.

3. We have seen that heating by photoionising radiation from the local extragalactic UVB is not effective during the main phase of the evolution of our model (around 10 Myr), since the temperature of the gas is above $T > 10^5$ K. During the rapid ($t \ll 1$ Myr) cooling in the centre of our model, the gas becomes cooler ($T < 10^5$ K) and at this point the UVB could have an impact on the cooling of the gas, and consequenty play a role in the accretion of this gas onto the galactic disc.

4. By heating the coronae with a constant central source with different powers, we see that for a high power source, the centre of the corona heats quickly to a density and temperature similar to those observed in the Fermi bubbles (Miller & Bregman, 2016), and then keeps heating indefinitely. For a low power source, the evolution of the corona is not influenced significantly. The transition region, or threshold power, for which the corona is not heating nor cooling, depends on the initial condition and the shape of the heating kernel, but is between $\dot{E} = (0.5 - 3) \times 10^{41}\,{\rm erg\,s^{-1}}$ for `mb2016` and $\dot{E} = (1 - 20) \times 10^{41}\,{\rm erg\,s^{-1}}$ for `mb2016-rescaled`.

5. We compare our range for the threshold powers with estimates of the source that inflated the Fermi and eROSITA bubbles (Miller & Bregman, 2016; Predehl et al., 2020; Yang et al., 2022), by assuming this source is self-regulating and therefore neighter cools nor heats the corona on time-scales longer than the duty cycle. We then calculate the average power of such a source over its complete duty cycle, where we consider a wide range for the time in which the source does not inject energy in the corona ($t_{\rm off}$). Most of the resulting average

powers are remarkebly similar to the threshold powers estimated in this thesis. Only the estimate from Predehl et al. (2020) is considerably lower compared to the other estimates, which might be related to the fact that it only estimates the energy in the eROSITA bubbles.

6. The agreement between the threshold powers, and the average powers of various estimates of the Milky Way bubbles, suggests that the source that created the bubbles is able to stop the corona from rapidly cooling in the centre, and start a self-regulating cycle that could keep the corona in equilibrium for a long time.

Future improvements for our model include a further study of the central heating source, where we could consider the impact of photoionising radiation from this source, and investigate the effect of different kernel shapes and sizes. We could also consider the addition of angular momentum in the model, or vary initial conditions like the gas density or Milky Way potential. Finally, we can also use our model to study the time the Milky Way bubbles need to cool, and thereby get a more direct estimate for t_{off}.

6 Acknowledgements

I would like to thank Andrea Afruni for helping me with obtaining and implementing the `CLOUDY` tables used in this thesis, and Lucia Armilotta for generating these tables. I would also like to thank my supervisor, Filippo Fraternali for all the personal supervision and feedback. He guided me throughout the project, always considered my own input and opinions and overall has allowed me to be an independent researcher. Moreover, I would also like to thank Filippo's research group with Barbara, Fernanda, Linn and others, for letting me be a part of the meetings during the thesis, explaining their research and struggles and always answering my questions. I have also enjoyed joining the small book club at the beginning of the year. Finally, I would like to thank all the people in the Master's research office. Without them, the day-to-day work would definitely have been less fun throughout the year, and they have been big motivation for me to come to the office every day.

References

Afruni A., Pezzulli G., Fraternali F., Grønnow A., 2023, Monthly Notices of the Royal Astronomical Society, 524, 2351

Anderson M. E., Churazov E., Bregman J. N., 2016, Monthly Notices of the Royal Astronomical Society, 455, 227

Balbus S. A., 1995, in The Physics of the Interstellar Medium and Intergalactic Medium. p. 328, `https://ui.adsabs.harvard.edu/abs/1995ASPC...80..328B`

Binney J., Dehnen W., Bertelli G., 2000, Monthly Notices of the Royal Astronomical Society, Volume 318, Issue 3, pp. 658-664., 318, 658

Binney J., Nipoti C., Fraternali F., 2009, Monthly Notices of the Royal Astronomical Society, 397, 1804

Birkinshaw M., 1999, Physics Reports, 310, 97

Bland-Hawthorn J., Cohen M., 2003, The Astrophysical Journal, 582, 246

Bland-Hawthorn J., Gerhard O., 2016, Annual Review of Astronomy and Astrophysics, vol. 54, p.529-596, 54, 529

Bland-Hawthorn J., et al., 2019, The Astrophysical Journal, 886, 45

Bogdán Á., et al., 2013, The Astrophysical Journal, 772, 97

Bondi H., 1952, Monthly Notices of the Royal Astronomical Society, 112, 195

Bregman J. N., Hodges-Kluck E., Qu Z., Pratt C., Li J.-T., Yun Y., 2022, The Astrophysical Journal, 928, 14

Buie E., Fumagalli M., Scannapieco E., 2020, The Astrophysical Journal, 890, 33

Cassen P., Pettibone D., 1976, The Astrophysical Journal, 208, 500

Chabrier G., 2003, Publications of the Astronomical Society of the Pacific, 115, 763

Chen H.-W., et al., 2023, The Astrophysical Journal Letters, 955, L25

Cimatti A., Fraternali F., Nipoti C., 2019, Introduction to Galaxy Formation and Evolution: From Primordial Gas to Present-Day Galaxies. Cambridge University Press

Clarke C., Carswell B., 2007, Principles of Astrophysical Fluid Dynamics. Cambridge University Press

Cooper A. P., et al., 2010, Monthly Notices of the Royal Astronomical Society, 406, 744

Crocker R. M., Bicknell G. V., Taylor A. M., Carretti E., 2015, The Astrophysical Journal, 808, 107

Dai X., Bregman J. N., Kochanek C. S., Rasia E., 2010, The Astrophysical Journal, 719, 119

Dai X., Anderson M. E., Bregman J. N., Miller J. M., 2012, The Astrophysical Journal, 755, 107

Das S., Mathur S., Gupta A., 2020, The Astrophysical Journal, 897, 63

Das S., Chiang Y.-K., Mathur S., 2023, The Astrophysical Journal, 951, 125

David L. P., Nulsen P. E. J., McNamara B. R., Forman W., Jones C., Ponman T., Robertson B., Wise M., 2001, The Astrophysical Journal, 557, 546

Dekel A., Birnboim Y., 2006, Monthly Notices of the Royal Astronomical Society, 368, 2

Dekel A., et al., 2009, Nature, 457, 451

Di Teodoro E. M., Fraternali F., 2014, Astronomy and Astrophysics, 567, A68

Diemer B., Kravtsov A. V., 2014, The Astrophysical Journal, 789, 1

Dormand J. R., Prince P. J., 1980, Journal of Computational and Applied Mathematics, 6, 19

Dutta A., Bisht M. S., Sharma P., Ghosh R., Roy M., Nath B. B., 2024, Beyond Radial Profiles: Using Log-Normal Distributions to Model the Multiphase Circumgalactic Medium (`arXiv:2310.03717`), doi:10.48550/arXiv.2310.03717, `http://arxiv.org/abs/2310.03717`

Fabian A. C., Nulsen P. E. J., Canizares C. R., 1984, Nature, 310, 733

Faerman Y., Sternberg A., McKee C. F., 2017, The Astrophysical Journal, 835, 52

Faerman Y., Sternberg A., McKee C. F., 2020, The Astrophysical Journal, 893, 82

Ferland G. J., et al., 2013, Revista Mexicana de Astronomia y Astrofisica, 49, 137

Fielding D., Quataert E., McCourt M., Thompson T. A., 2017, Monthly Notices of the Royal Astronomical Society, 466, 3810

Fielding D. B., et al., 2020, The Astrophysical Journal, 903, 32

Finkbeiner D. P., 2004, The Astrophysical Journal, 614, 186

Forman W., Jones C., Tucker W., 1985, The Astrophysical Journal, 293, 102

Fragkoudi F., et al., 2020, Monthly Notices of the Royal Astronomical Society, 494, 5936

Fraternali F., 2017, in , Vol. 430, Springer, Cham. Springer International Publishing, Cham, p. 323, `https://ui.adsabs.harvard.edu/abs/2017ASSL..430..323F`

Fraternali F., Tomassetti M., 2012, Monthly Notices of the Royal Astronomical Society, 426, 2166

Fraternali F., Marasco A., Marinacci F., Binney J., 2013, The Astrophysical Journal, 764, L21

Fritsch F. N., Butland J., 1984, SIAM journal on scientific and statistical computing, 5, 300

Fryxell B., et al., 2000, The Astrophysical Journal Supplement Series, 131, 273

Fukugita M., Peebles P. J. E., 2006, The Astrophysical Journal, 639, 590

Greco J. P., Hill J. C., Spergel D. N., Battaglia N., 2015, The Astrophysical Journal, 808, 151

Grønnow A., Fraternali F., Marinacci F., Pezzulli G., Tolstoy E., Helmi A., Brown A. G. A., 2024, Monthly Notices of the Royal Astronomical Society, 528, 3009

Gupta A., Mathur S., Krongold Y., Nicastro F., Galeazzi M., 2012, The Astrophysical Journal, 756, L8

Haardt F., Madau P., 2012, The Astrophysical Journal, 746, 125

Hafen Z., et al., 2022, Monthly Notices of the Royal Astronomical Society, 514, 5056

Hairer E., Norsett S., Wanner G., 1993, Solving Ordinary Differential Equations I: Nonstiff Problems. Vol. 8, Springer-Verlag, doi:10.1007/978-3-540-78862-1

Helmi A., 2008, The Astronomy and Astrophysics Review, 15, 145

Henley D. B., Shelton R. L., 2013, The Astrophysical Journal, 773, 92

Ji S., et al., 2020, Monthly Notices of the Royal Astronomical Society, 496, 4221

Joung M. R., Bryan G. L., Putman M. E., 2012, The Astrophysical Journal, 745, 148

Kaaret P., et al., 2020, Nature Astronomy, Volume 4, p. 1072-1077, 4, 1072

Kaiser C. R., Binney J., 2003, Monthly Notices of the Royal Astronomical Society, 338, 837

Kereš D., Hernquist L., 2009, The Astrophysical Journal, 700, L1

Kereš D., Katz N., Fardal M., Davé R., Weinberg D. H., 2009, Monthly Notices of the Royal Astronomical Society, 395, 160

Kroupa P., 2002, Science, 295, 82

Kubryk M., Prantzos N., Athanassoula E., 2013, Monthly Notices of the Royal Astronomical Society, 436, 1479

Lam S. K., Pitrou A., Seibert S., 2015, in Proceedings of the Second Workshop on the LLVM Compiler Infrastructure in HPC. LLVM '15. Association for Computing Machinery, New York, NY, USA, pp 1–6, doi:10.1145/2833157.2833162, `https://doi.org/10.1145/2833157.2833162`

Landau R. H., Páez M. J., Bordeianu C. C., 2015, Computational Physics: Problem Solving with Python. John Wiley & Sons

Li Y., Bregman J., 2017, The Astrophysical Journal, 849, 105

Li J.-T., Bregman J. N., Wang Q. D., Crain R. A., Anderson M. E., 2016, The Astrophysical Journal, 830, 134

Locatelli N., et al., 2024, Astronomy and Astrophysics, 681, A78

Lochhaas C., et al., 2023, The Astrophysical Journal, 948, 43

Maciel W. J., 2013, Astrophysics of the Interstellar Medium. Springer, New York, NY, doi:10.1007/978-1-4614-3767-3, `https://link.springer.com/10.1007/978-1-4614-3767-3`

Marinacci F., Binney J., Fraternali F., Nipoti C., Ciotti L., Londrillo P., 2010, Monthly Notices of the Royal Astronomical Society, 404, 1464

McGaugh S. S., Schombert J. M., de Blok W. J. G., Zagursky M. J., 2009, The Astrophysical Journal Letters, 708, L14

McNamara B. R., Nulsen P. E. J., 2007, Annual Review of Astronomy and Astrophysics, 45, 117

Miller M. J., Bregman J. N., 2013, The Astrophysical Journal, 770, 118

Miller M. J., Bregman J. N., 2016, The Astrophysical Journal, 829, 9

Navarro J. F., Frenk C. S., White S. D. M., 1997, The Astrophysical Journal, 490, 493

Nicastro F., et al., 2023, The Astrophysical Journal Letters, Volume 955, Issue 1, id.L21, $<$NUMPAGES$>$19$<$/NUMPAGES$>$ pp., 955, L21

O'Sullivan E., Ponman T. J., Collins R. S., 2003, Monthly Notices of the Royal Astronomical Society, 340, 1375

Peeples M. S., Werk J. K., Tumlinson J., Oppenheimer B. D., Prochaska J. X., Katz N., Weinberg D. H., 2014, The Astrophysical Journal, 786, 54

Planck Collaboration et al., 2020, Astronomy and Astrophysics, 641, 67

Ponti G., et al., 2023, Astronomy and Astrophysics, 674, A195

Posti L., Helmi A., 2019, Astronomy and Astrophysics, 621, A56

Predehl P., et al., 2020, Nature, 588, 227

Press W. H., Teukolsky S. A., Vetterling W. T., Flannery B. P., eds, 2007, Numerical Recipes: The Art of Scientific Computing, 3. ed edn. Cambridge University Press, Cambridge

Salem M., Bryan G. L., Corlies L., 2016, Monthly Notices of the Royal Astronomical Society, 456, 582

Salpeter E. E., 1955, The Astrophysical Journal, 121, 161

Scalo J. M., 1986, Fundamentals of Cosmic Physics, 11, 1

Schönrich R., Binney J., 2009, Monthly Notices of the Royal Astronomical Society, 396, 203

Schönrich R., McMillan P. J., 2017, Monthly Notices of the Royal Astronomical Society, p. stx093

Selig M., Vacca V., Oppermann N., Enßlin T. A., 2015, Astronomy and Astrophysics, 581, A126

Snowden S. L., et al., 1997, The Astrophysical Journal, 485, 125

Sofue Y., 2000, The Astrophysical Journal, 540, 224

Sormani M. C., Sobacchi E., 2019, Monthly Notices of the Royal Astronomical Society, 486, 215

Sparke L. S., Gallagher III J. S., 2007, Galaxies in the Universe: An Introduction. Cambridge University Press

Springel V., di Matteo T., Hernquist L., 2005, Monthly Notices of the Royal Astronomical Society, 361, 776

Stern J., Fielding D., Faucher-Giguère C.-A., Quataert E., 2019, Monthly Notices of the Royal Astronomical Society, 488, 2549

Stern J., Fielding D., Hafen Z., Su K.-Y., Naor N., Faucher-Giguère C.-A., Quataert E., Bullock J., 2024, Monthly Notices of the Royal Astronomical Society, 530, 1711

Su M., Slatyer T. R., Finkbeiner D. P., 2010, The Astrophysical Journal, 724, 1044

Sunyaev R. A., Zeldovich Ya. B., 1970, Comments on Astrophysics and Space Physics, 2, 66

Sutherland R. S., Dopita M. A., 1993, The Astrophysical Journal Supplement Series, 88, 253

Tumlinson J., Peeples M. S., Werk J. K., 2017, Annual Review of Astronomy and Astrophysics, 55, 389

Twarog B. A., 1980, Astrophysical Journal, Part 1, vol. 242, Nov. 15, 1980, p. 242-259., 242, 242

Vanderlinde K., et al., 2010, The Astrophysical Journal, Volume 722, Issue 2, pp. 1180-1196 (2010)., 722, 1180

Veilleux S., Cecil G., Bland-Hawthorn J., 2005, Annual Review of Astronomy and Astrophysics, 43, 769

Virtanen P., et al., 2020, Nature Methods, 17, 261

Voit G. M., 2021, The Astrophysical Journal Letters, 908, L16

Voit G. M., Pandya V., Fielding D. B., Bryan G. L., Carr C., Donahue M., Oppenheimer B. D., Somerville R. S., 2024, Equilibrium States of Galactic Atmospheres I: The Flip Side of Mass Loading, doi:10.48550/arXiv.2406.07631, `https://ui.adsabs.harvard.edu/abs/2024arXiv240607631V`

Weaver R., McCray R., Castor J., Shapiro P., Moore R., 1977, The Astrophysical Journal, 218, 377

Weinberger R., et al., 2017, Monthly Notices of the Royal Astronomical Society, 465, 3291

Whitaker K. E., van Dokkum P. G., Brammer G., Franx M., 2012, The Astrophysical Journal, 754, L29

White S. D. M., Frenk C. S., 1991, The Astrophysical Journal, 379, 52

Yang H.-Y. K., Ruszkowski M., Zweibel E. G., 2018, Galaxies, 6, 29

Yang H. Y. K., Ruszkowski M., Zweibel E. G., 2022, Nature Astronomy, 6, 584

Zhang R., Guo F., 2020, The Astrophysical Journal, 894, 117

Zhang Y., et al., 2024, The Hot Circum-Galactic Medium in the eROSITA All Sky Survey I. X-ray Surface Brightness Profiles, doi:10.48550/arXiv.2401.17308, `https://ui.adsabs.harvard.edu/abs/2024arXiv240117308Z`

van de Voort F., Schaye J., Booth C. M., Dalla Vecchia C., 2011, Monthly Notices of the Royal Astronomical Society, 415, 2782

Acronyms

AGN active galactic nuclei

CGM circumgalactic medium

CIE collisional ionisation equilibrium

CMB Cosmic Microwave Background

CR cosmic ray

GC galactic centre

IGM intergalactic medium

IMF initial mass function

ISM interstellar medium

JIT just-in-time

NFW Navarro-Frenk-White

NSF nuclear star formation

ODE ordinary differential equation

PCHIP Piecewise Cubic Hermite Interpolating Polynomial

SFR star formation rate

SZE Sunyaev-Zeldovich Effect

UVB ultraviolet background

A Calculations and Derivations

A.1 Rewriting thermodynamical quantities

We can rewrite the term $C_{\mathrm{V}}\mu m_{\mathrm{p}}$ using the following relations and definitions of specific heats, specific gas constant $\mathcal{R}$, the mass of a mole m_{mol} and the Boltzmann constant k_B

$$C_{\mathrm{P}} = C_{\mathrm{V}} + \mathcal{R}, \quad \mathcal{R} = R/m_{\mathrm{mol}}, \quad m_{\mathrm{mol}} = N_A \mu m_{\mathrm{p}}, \quad R = k_{\mathrm{B}} N_{\mathrm{A}}, \quad \gamma = C_{\mathrm{P}}/C_{\mathrm{V}}. \tag{85}$$

$$C_{\mathrm{P}} = C_{\mathrm{V}} + \mathcal{R}, \tag{86}$$

$$\frac{\mathcal{R}}{C_{\mathrm{V}}} = \frac{C_{\mathrm{P}}}{C_{\mathrm{V}}} - 1, \tag{87}$$

$$\mathcal{R} = C_{\mathrm{V}}(\gamma - 1). \tag{88}$$

Then, rewriting $\mathcal{R}$:

$$\mathcal{R} = R/m_{\mathrm{mol}}, \tag{89}$$

$$\mathcal{R} = \frac{k_{\mathrm{B}}/N_{\mathrm{A}}}{N_{\mathrm{A}}\mu m_{\mathrm{p}}} = \frac{k_{\mathrm{B}}}{\mu m_{\mathrm{p}}}. \tag{90}$$

Combining Equations 88 and 90 finally gives us:

$$\frac{k_{\mathrm{B}}}{\mu m_{\mathrm{p}}} = C_{\mathrm{V}}(\gamma - 1) \implies \mu m_{\mathrm{p}} C_{\mathrm{V}} = \frac{k_{\mathrm{B}}}{\gamma - 1}. \tag{91}$$

A.2 Average entropy-index in an unstable region

We derive the equation which we use to calculate the average entropy-index $\bar{\sigma}$ used to remove regions with negative entropy gradients (see Section 2.2.4), using the method outlined in Binney et al. (2009). Given a region with a negative entropy gradient starting at radius r_1 and ending at r_2 ($\mathcal{S}(r_1) > \mathcal{S}(r_2)$), in this region the entropy never increases

$$\mathcal{S}(r_i) \geq \mathcal{S}(r_j), \quad \text{for } r_1 \leq r_i \leq r_j \leq r_2. \tag{92}$$

To remove the negative gradient, we change the entropy at each radius r_i in the unstable region from the initial entropy $\mathcal{S}(r_i)$ to the mass-weighted average value $\bar{\mathcal{S}}$. The difference is then given by

$$\bar{\mathcal{S}} - \mathcal{S}(r_i) = \mathrm{d}\mathcal{S}(r_i) = \frac{\mathrm{d}\mathcal{Q}(r_i)}{T(r_i)}, \tag{93}$$

where $T(r_i)$ is the temperature and $\mathrm{d}\mathcal{Q}(r_i)$ is the change in specific heat at radius r_i, and we used the relation between change in specific entropy and specific heat for a reversible transformation $d\mathcal{Q} = Td\mathcal{S}$. When we apply this change, no heat enters or leaves the region, so the sum of all changes in heat should be 0

$$\sum \mathrm{d}Q(r_i) = 0. \tag{94}$$

Using the definition of a specific quantity $d\mathcal{Q}(r_i) = \mathrm{d}Q(r_i)/m(r_i)$, where $m(r_i)$ is the gas mass inside the shell at radius r_i, and multiplying Equation 93 by the temperature and shell mass, we then obtain

$$\sum_i T(r_i)m(r_i)\left[\bar{\mathcal{S}} - \mathcal{S}(r_i)\right] = \sum_i \mathrm{d}Q(r_i) = 0. \tag{95}$$

Finally, we isolate $\bar{\mathcal{S}}$

$$\bar{\mathcal{S}} = \frac{\sum_i \mathcal{S}(r_i)T(r_i)m(r_i)}{\sum_i T(r_i)m(r_i)}, \tag{96}$$

to get the average entropy in terms of entropy, temperature and mass in the convectively unstable region. Since our model makes use of the entropy-index, we substitute $\mathcal{S} = C_{\mathrm{V}} \ln \sigma + \text{constant}$ in in Equation 96, and the constants cancel out to give

$$\ln \bar{\sigma} = \frac{\sum_i \ln[\sigma(r_i)] T(r_i) m(r_i)}{\sum_i T(r_i) m(r_i)}. \tag{97}$$

A.3 Taylor approximation for NFW potential

When we evaluate the gradient of the NFW potential (Equation 50) numerically for very small r ($r \ll r_s$), there are some instabilities due to being close to dividing by 0. To compute this potential without issues, we therefore separate the functional part of the gradient

$$\frac{\mathrm{d}\Phi}{\mathrm{d}r} = -16\pi G \rho_s r_s f(r/r_s), \qquad \text{where } f(x) \equiv \frac{\frac{x}{(1+x)} - \ln(1+x)}{x^2}, \tag{98}$$

and evaluate the limit

$$\lim_{x\to 0} f(x) = -\frac{1}{2}. \tag{99}$$

Since $f(x)$ converges as $x \to 0$, we can evaluate $\mathrm{d}\Phi/\mathrm{d}r$ using a taylor series whenever r is sufficiently small to avoid numerical instabilities. The second order taylor expansion of $f(x)$ is

$$f(x) \approx -\frac{1}{2} + \frac{2}{3}x - \frac{3}{4}x^2 + \mathcal{O}(x^3), \tag{100}$$

so, at the end we compute $f(x)$ as follows

$$f(x) = \begin{cases} -\frac{1}{2} + \frac{2}{3}x - \frac{3}{4}x^2 & \text{if } x < 0.005 \\ \frac{x/(1+x) - \ln(1+x)}{x^2} & \text{otherwise} \end{cases} \tag{101}$$

A.4 Units in integration

To avoid numerical instabilities due to floating point calculations (Landau et al., 2015), we choose units for our quantities such that their values will be around 1. To keep the quantities in their chosen unit, we then have to determine multiplication constants for every equation we use. Given a quantity Q and chosen unit Q_u, and $\hat{Q}$ the value of Q in the chosen unit (i.e. $\hat{Q} = Q/Q_u$), we determine the multiplication constant C for the equation as follows

$$P = nk_BT \quad \equiv \quad \hat{P}P_u = \hat{n}n_u\, k_B\, \hat{T}T_u, \tag{102}$$

$$\equiv \quad \hat{P} = \hat{n}\hat{T} \cdot \left(\frac{n_u T_u k_B}{P_u}\right), \tag{103}$$

$$\equiv \quad \hat{P} = C_{\text{ideal}} \hat{n}\hat{T}, \tag{104}$$

where the multiplication constant is then (in our chosen unit system)

$$C_{\text{ideal}} \equiv \frac{n_u T_u k_B}{P_u} \approx 1.380 \times 10^3. \tag{105}$$

For our calculations, we have used the following units

temperature : 10^6K
length : pc
entropy-index : $10^{30}\mathrm{cm}^4\,\mathrm{g}^{-2/3}\,\mathrm{s}^{-2}$
mass : $10^8\mathrm{M}_\odot$
density : $m_\mathrm{p}\mathrm{cm}^{-3}$
time : Myr
pressure : $10^{-13}\mathrm{erg\,cm}^{-3}$
number density : cm^{-3}
velocity : $\mathrm{km\,s}^{-1}$

A.5 Full steady-state cooling flow solutions for Milky Way mass haloes

Here we derive the full density, radial velocity and temperature profiles from the general steady-state solutions of Stern2019 for the Milky Way. First we rewrite the general solutions in terms of m, and finally in the specific case of $m = 0$ as well. The general form of these steady-state solutions for these specific quantities can be written as

$$\rho(r) = \frac{m_\mathrm{p}}{X}\sqrt{\frac{9B}{40\pi A}}\sqrt{\frac{\dot{M}}{\Lambda}}\frac{v_c(r)}{r^{3/2}}, \tag{106}$$

$$|v_r(r)| = \frac{X}{m_\mathrm{p}}\sqrt{\frac{5A}{18\pi B}}\frac{\sqrt{\dot{M}\Lambda}}{v_c(r)r^{1/2}}, \tag{107}$$

$$T(r) = \frac{6}{5A}\left(\frac{r}{R_\mathrm{vir}}\right)^{2m}T_\mathrm{vir}, \tag{108}$$

where X is the hydrogren fraction of the gas, assumed to be $X = 0.75$, the other constants A, B come from the integration and can be expressed as a function of m

$$A \equiv \frac{v_c^2}{c_s^2} = \frac{9}{10}(1-2m), \quad B \equiv \frac{t_\mathrm{flow}}{t_\mathrm{cool}} = 1 + (4/3)m, \tag{109}$$

and, we used $n_H = X\rho/m_\mathrm{p}$ and $\mathcal{M} = |v_r|/c_s = \sqrt{A}|v_r|/v_c$ to convert equations 26 and 27 from Section 2.3 in Stern2019. To apply these relations to the Milky Way, we use the following approximation of the circular speed as used by Stern2019, Section 2.5:

$$v_c(r) = 140\left(\frac{M_\mathrm{vir}}{10^{12}\,\mathrm{M}_\odot}\right)^{0.36}\left(\frac{r}{100\,\mathrm{kpc}}\right)^{m}\mathrm{km\,s^{-1}}, \tag{110}$$

and use the following forms for the virial radius and temperature (equations 8,9 in Stern2019) as a function of the virial mass of the halo

$$R_\mathrm{vir} = 260\left(\frac{M_\mathrm{vir}}{10^{12}\,\mathrm{M}_\odot}\right)^{1/3}\mathrm{kpc}, \tag{111}$$

$$T_\mathrm{vir} = 6\times10^5\left(\frac{M_\mathrm{vir}}{10^{12}\,\mathrm{M}_\odot}\right)^{2/3}\mathrm{K}. \tag{112}$$

We use these expressions to convert equations 106-108 to be in units similar to Stern2019, but still as a function of m

$$\rho(r) = 2.3\times10^{-5}\sqrt{\frac{B}{A}}\left(\frac{M_\mathrm{vir}}{10^{12}\,\mathrm{M}_\odot}\right)^{0.36}\left(\frac{\dot{M}}{\mathrm{M}_\odot/\mathrm{yr}}\right)^{1/2}\left(\frac{\Lambda}{10^{-22}\,\mathrm{erg\,cm^3\,s^{-1}}}\right)^{-1/2}\left(\frac{r}{100\,\mathrm{kpc}}\right)^{m-3/2}m_\mathrm{p}\,\mathrm{cm}^{-3}, \tag{113}$$

$$|v_r(r)| = 13.6\sqrt{\frac{A}{B}}\left(\frac{M_\mathrm{vir}}{10^{12}\,\mathrm{M}_\odot}\right)^{-0.36}\left(\frac{\dot{M}}{\mathrm{M}_\odot/\mathrm{yr}}\right)^{1/2}\left(\frac{\Lambda}{10^{-22}\,\mathrm{erg\,cm^3\,s^{-1}}}\right)^{1/2}\left(\frac{r}{100\,\mathrm{kpc}}\right)^{-m-1/2}\mathrm{km\,s^{-1}}, \tag{114}$$

$$T(r) = \frac{7.2\times10^5}{A\cdot2.6^{2m}}\left(\frac{M_\mathrm{vir}}{10^{12}\,\mathrm{M}_\odot}\right)^{2/3-2m/3}\left(\frac{r}{100\,\mathrm{kpc}}\right)^{2m}\mathrm{K}. \tag{115}$$

For $m = 0$, we then finally obtain

$$\rho(r) = 2.4 \times 10^{-5} \left(\frac{M_{\mathrm{vir}}}{10^{12}\,\mathrm{M}_{\odot}} \right)^{0.36} \left(\frac{\dot{M}}{\mathrm{M}_{\odot}/\mathrm{yr}} \right)^{1/2} \left(\frac{\Lambda}{10^{-22}\,\mathrm{erg}\,\mathrm{cm}^{3}\,\mathrm{s}^{-1}} \right)^{-1/2} \left(\frac{r}{100\,\mathrm{kpc}} \right)^{-3/2} m_{\mathrm{p}}\,\mathrm{cm}^{-3}, \tag{116}$$

$$|v_r(r)| = 12.9 \left(\frac{M_{\mathrm{vir}}}{10^{12}\,\mathrm{M}_{\odot}} \right)^{-0.36} \left(\frac{\dot{M}}{\mathrm{M}_{\odot}/\mathrm{yr}} \right)^{1/2} \left(\frac{\Lambda}{10^{-22}\,\mathrm{erg}\,\mathrm{cm}^{3}\,\mathrm{s}^{-1}} \right)^{1/2} \left(\frac{r}{100\,\mathrm{kpc}} \right)^{-1/2} \mathrm{km}\,\mathrm{s}^{-1}, \tag{117}$$

$$T = 8 \times 10^{5} \left(\frac{M_{\mathrm{vir}}}{10^{12}\,\mathrm{M}_{\odot}} \right)^{2/3} \mathrm{K}. \tag{118}$$

B Code

The code that has been written to produce the results and plots in the thesis is published on Github[8]. This repository contains a mix of a general-purpose package containing code for the integration (folder `KB_Model`) and interpolation of `CLOUDY` tables (folder `CLOUDY`). Notebooks and scripts that have been used to produce the results and create all plots can be found in the `Notebooks` folder. These notebooks have been executed on the Kapteyn servers, using the `anaconda3/2024.02` kernel, Python version 3.11.7. To use the code in for example the `KB_Model` module, you can add the directory to the path variable

```
from pathlib import Path
import sys
module_location = Path('/path/to/the/folder/KB_Model') # Specify
sys.path.append(str(module_location))
```

and then you can import submodules, for example

```
from models import beta_model
```

Make sure to properly specify these paths *before* executing the notebooks.

---

[8] url: https://github.com/StenSipma/MscThesisAstronomy

C Figures

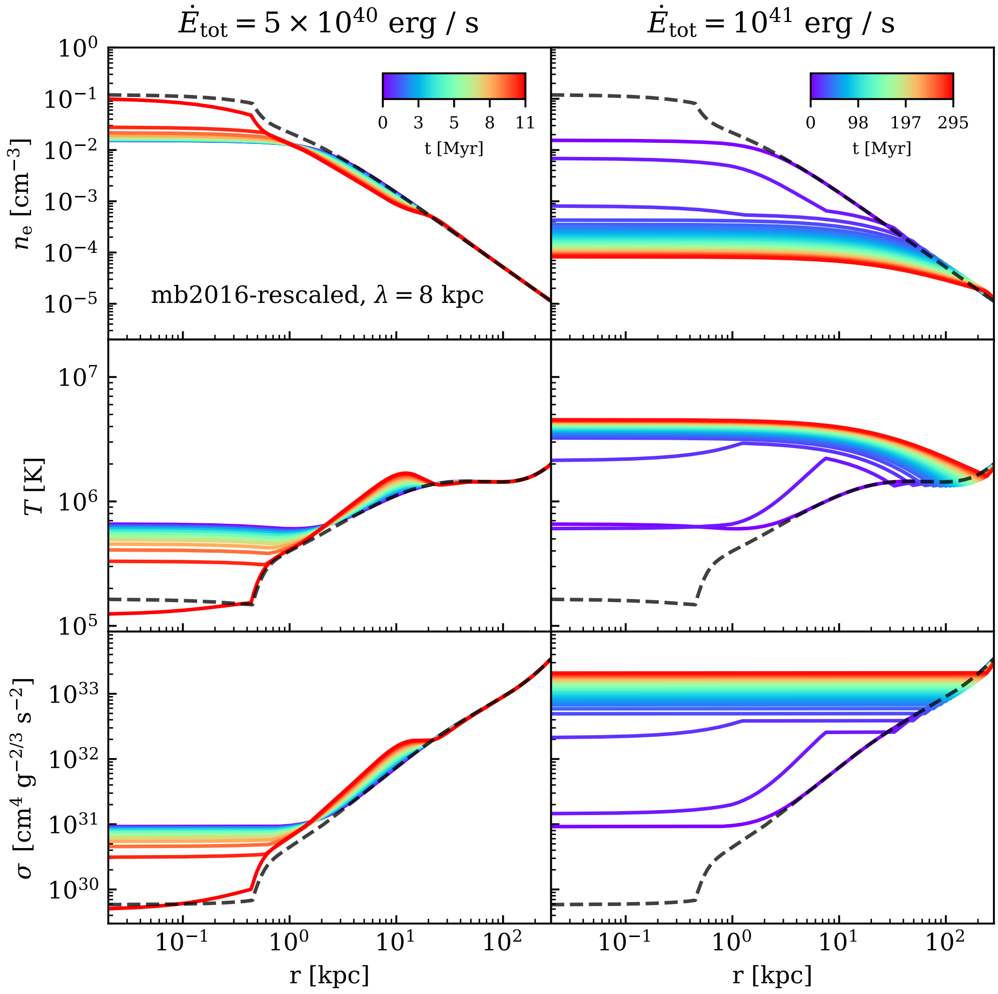

Figure 31: Full evolutions of the electron density, temperature and entropy-index of the lower (left column) and upper (right column) bounds to the threshold power of the `mb2016-rescaled` corona with heating scale length $\lambda = 8\,\text{kpc}$. The colour of the lines indicate the time of the evolution. For reference, the last timestep of the evolution without heating is included as a black dashed line (see Figure 15).

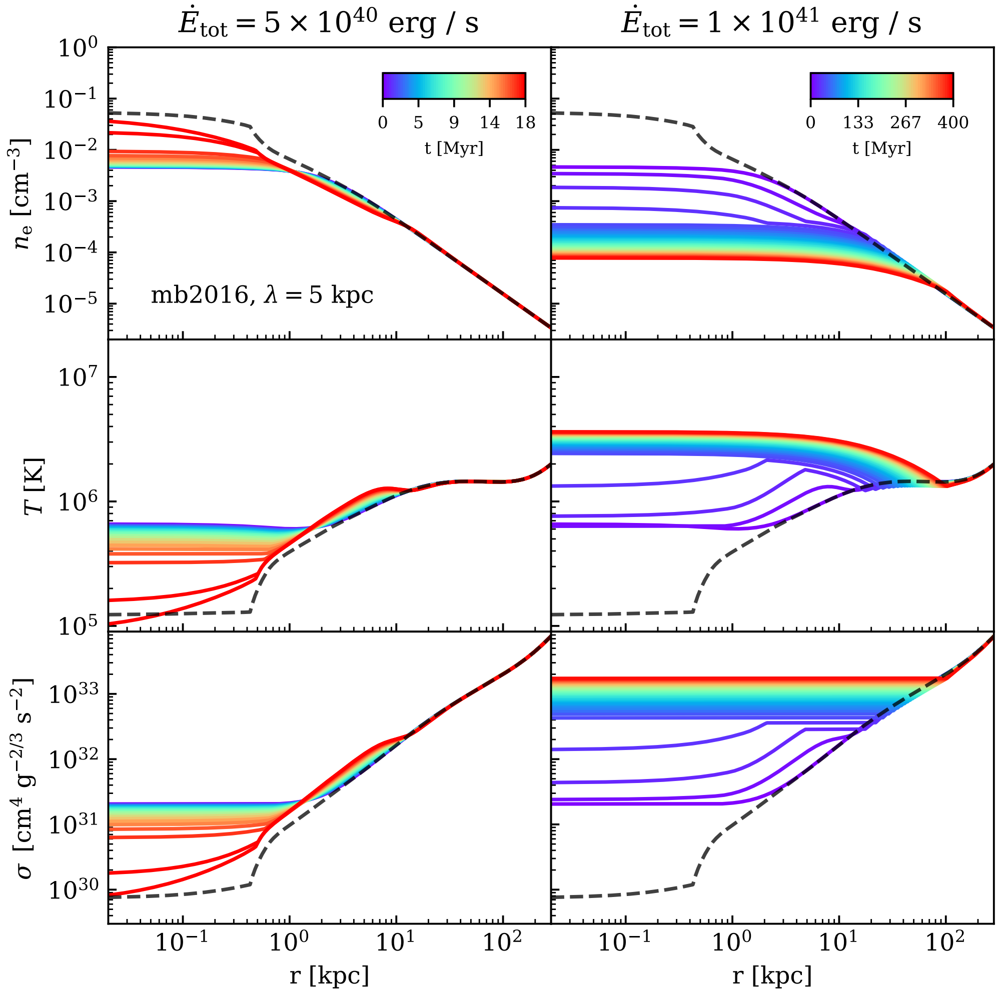

Figure 32: Full evolutions of the electron density, temperature and entropy-index of the lower (left column) and upper (right column) bounds to the threshold power of the `mb2016` corona with heating scale length $\lambda = 5\,\mathrm{kpc}$. The colour of the lines indicate the time of the evolution. For reference, the last timestep of the evolution without heating is included as a black dashed line (see Figure 15).

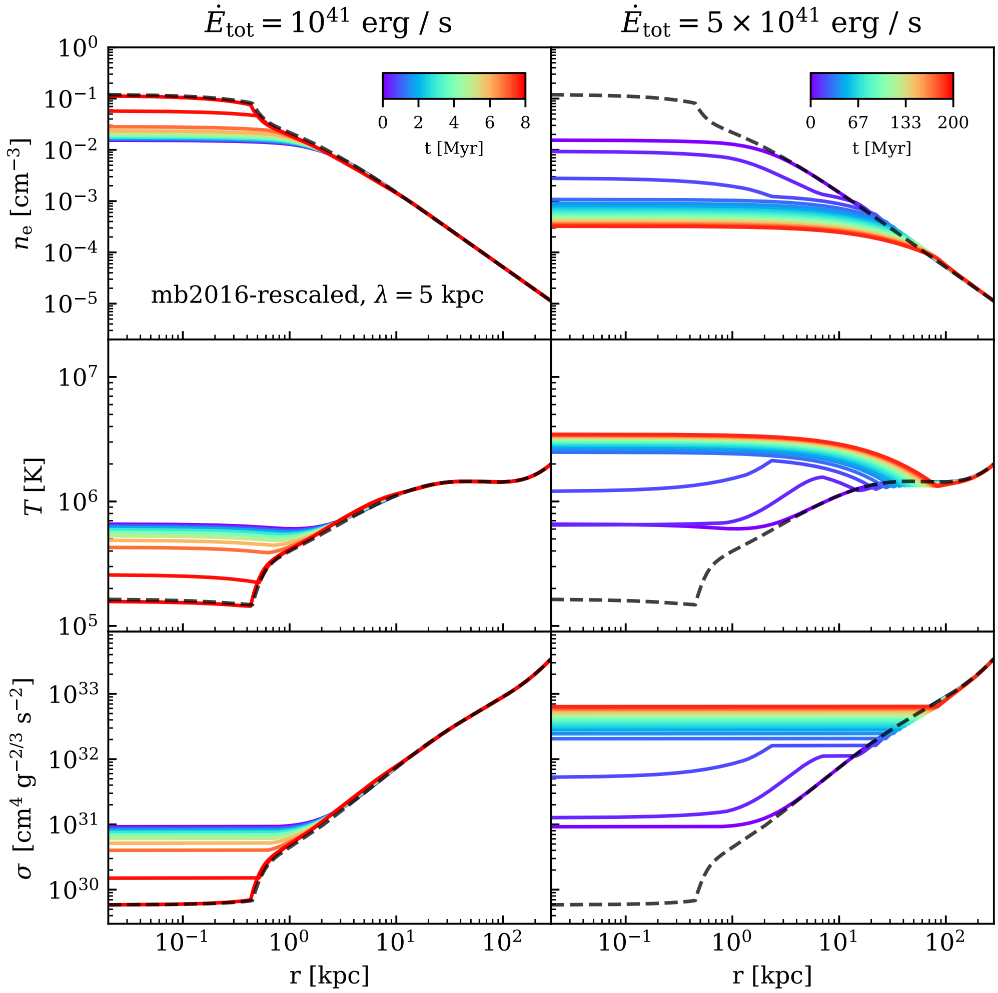

Figure 33: Full evolutions of the electron density, temperature and entropy-index of the lower (left column) and upper (right column) bounds to the threshold power of the `mb2016-rescaled` corona with heating scale length $\lambda = 5\,\mathrm{kpc}$. The colour of the lines indicate the time of the evolution. For reference, the last timestep of the evolution without heating is included as a black dashed line (see Figure 15).